Development of high-performance mid-infrared laser sources for isotope detection applications

LI Enhao

Doctor of Philosophy

Department of Fusion Science
School of Physical Sciences

The Graduate University for Advanced Studies, SOKENDAI

September 2023

Contents

I. Introduction

1.1 Isotope Detection in Nuclear Fusion Reactors

Isotope detection is instrumental in environmental studies, enabling scientists to track the movement of pollutants, assess the impact of human activities on ecosystems, and monitor the effectiveness of remediation efforts. In nuclear fusion science, the isotope analysis technique also plays a vital role in the development of advanced diagnostics and monitoring systems for nuclear fusion reactors, providing real-time feedback on plasma parameters, isotopic changes, and potential anomalies, which could help to ensure safe and efficient operation.

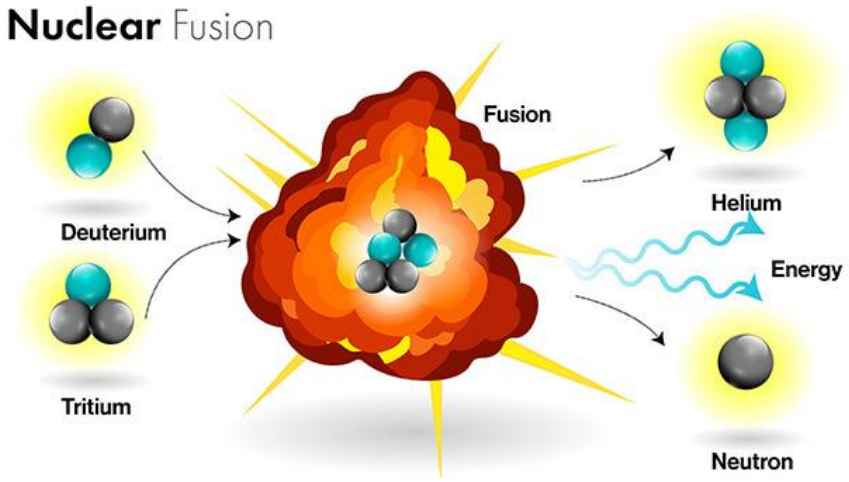

Fig. 1-1. Deuterium-Tritium fusion reaction [1-1].

Fusion energy is an ideal clean energy source extracted from nuclear fusion reactions, in which two light atomic nuclei join together while releasing vast amounts of energy, as shown in Fig. 1-1 [1-1]. The most pursued fusion reaction is the fusion of hydrogen isotopes, specifically deuterium and tritium. Deuterium is a stable isotope of hydrogen that can be readily extracted from seawater, while tritium is a radioactive isotope that can be produced within a fusion reactor itself by utilizing lithium, which is found abundant in the Earth's crust. The fusion of deuterium and tritium (DT reaction) is particularly appealing for practical fusion power generation due to its relatively low activation energy and high reaction rate compared to other fusion reactions (DD, D^3He reactions), as shown in Fig. 1-

2. Therefore, the DT reaction is the most practical and feasible solution for first-generation fusion power plants.

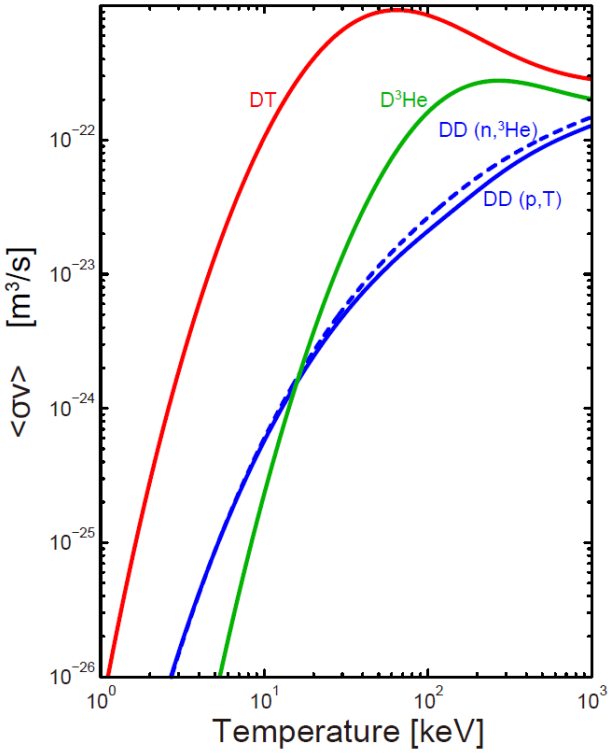

Fig. 1-2. Fusion cross-sections for the most important fusion reactions as a function of ion temperature in keV [1-2].

Magnetic confinement fusion is one of the most prominent approaches to achieving DT fusion reaction, which confines a hot plasma of deuterium and tritium within a strong magnetic field. The plasma is heated to temperatures exceeding several tens of keV, where the fusion reaction rate can reach its maximum (see the red curve in Fig. 1-2), causing the deuterium and tritium ions to collide at high speeds, overcome their electrostatic repulsion, and fuse together. This method is expected to achieve self-sustained fusion reactions and releases more energy than is needed to maintain the plasma. Currently, the International Thermonuclear Experimental Reactor (ITER), which will be the world's largest magnetic confinement fusion reactor, is being constructed, aiming to achieve a self-sustained fusion reaction, to address critical challenges associated with fusion science, and finally to pave the way for the development of the next generation of fusion power plants.

The design of fuel circulation systems in fusion reactors, especially the design for

handling tritium, is of great importance because tritium is a naturally scarce and radioactive substance. On the one hand, it serves as indispensable fuel for the DT fusion reaction. On the other hand, it often exists as tritiated water (HTO) in the cooling system of fusion facilities, as depicted in a typical fuel circulation system shown in Figure 1-3. For future fusion reactors, water-cooling is still the most practical approach for cooling the blanket system, which converts the kinetic energy of neutrons to heat and breeds the tritium fuel from the neutron-Lithium reaction [1-3]. However, due to the permeation effect, some tritium will be transported in the blanket and then dissolved in the cooling water. Although several efforts have been made to develop anti-permeation membrane [1-4] to prevent tritium from permeating into the cooling pipes, there is still a possibility for tritium leakage if the anti-permeation membrane is damaged by a sudden accident. In addition, as the cooling pipes are intricately installed around the fusion reactor, this leakage is likely to cause widespread tritium migration and radioactive contamination. Therefore, from the perspective of recycling valuable fusion fuel and managing radioactive contaminants, it is necessary to continuously monitor the water isotopes in nuclear fusion environments to ensure a safe and steady operation.

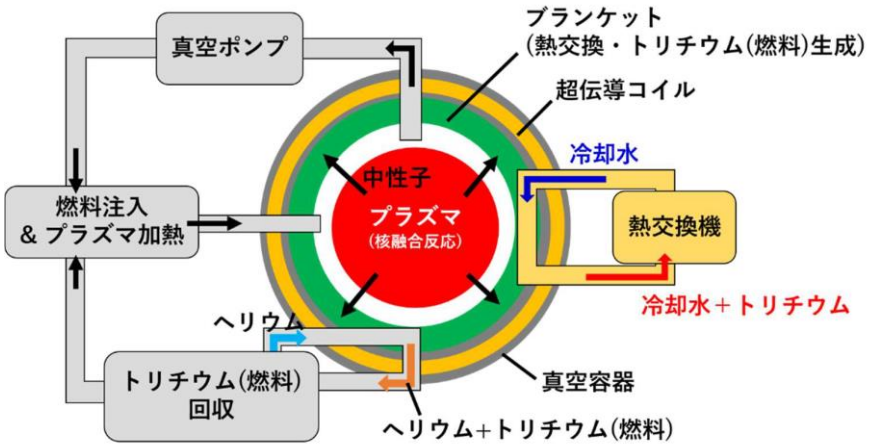

Fig. 1-3. Fuel circulation system for future DT fusion reactor.

Currently, the two commonly used methods for hydrogen isotope detection are mass spectrometry (MS) [1-5] and liquid scintillation counter (LSC) [1-6]. Both of these techniques can determine the isotopic composition of samples with high sensitivity and accuracy. However, typical MS or LSC facilities are huge, complex, and costly, as shown

in Fig. 1-4. More importantly, they usually necessitate complicated sample preparation processes and are difficult to measure gaseous samples directly, thus making them unavailable for continuous, real-time, and in-situ measurements. Therefore, there is an urgent need to develop novel isotope detection systems that can fulfill the requirements of real-time measurements in the nuclear fusion environment.

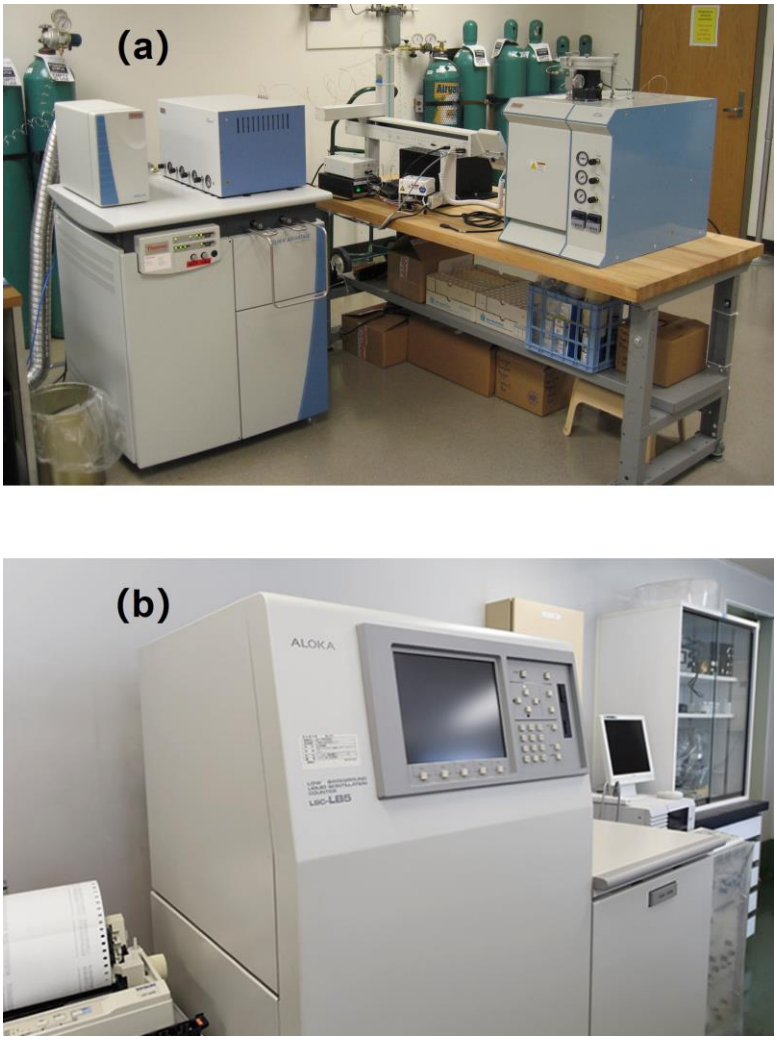

Fig. 1-4. Typical devices for measuring hydrogen isotope. (a) Isotope-ratio mass spectrometry [1-7]. (b) Liquid scintillation counter [1-8].

1.2 Laser Absorption Spectroscopy for Isotope Detection

The optical method using laser absorption spectroscopy (LAS) is an alternative approach for isotope detection that enables real-time, in-situ measurements while also providing high detection sensitivity. LAS utilizes the optical absorption properties of the target samples to extract information about the sample's composition. All substances have their specific absorption spectrum because of the unique energy levels and transitions within the atoms or molecules. When light interacts with matter, typically passing through a sample, the matter can absorb the energy of the light, resulting in energy transitions between different energy states. As for the light source, it exhibits an attenuation of light intensity after passing through the sample. By analyzing the absorption spectrum of the sample, we can identify the presence of specific substances and determine their concentration.

With the rapid development of optics and laser sources at new wavelength bands, the LAS technique is also evolving toward higher detection sensitivity and accuracy, as well as lower concentration detection limits. Here we review several typical LAS techniques and introduce their fundamental principles and characteristics respectively.

(1). Direct absorption spectroscopy based on "light→sample→detector" structure

The "light→sample→detector" is the most conventional architecture used for the LAS technique, which utilizes the Beer-Lambert Law [1-9] to derive the sample concentration. The Beer-Lambert Law is used to describe the attenuation of laser after passing through a sample:

$$I = I_0 \exp(-\alpha L) \tag{1-1}$$

where I_0 means the initial laser intensity, I represents the laser intensity after passing through the sample, L represents the optical path length of the sample, and α is the absorption coefficient of the sample to be measured.

Figure 1-5 shows the schematic diagram of a typical "light→sample→detector" setup. First, a laser source, typically a tunable laser, is injected into the gas cell. After a single pass through the sample, a photodetector receives the laser signal to record the laser intensity. During the experiment, the laser wavelength should be scanned over the absorption peaks of the target sample; then the sample concentration can be calculated by

comparing the recorded laser intensities with and without the sample.

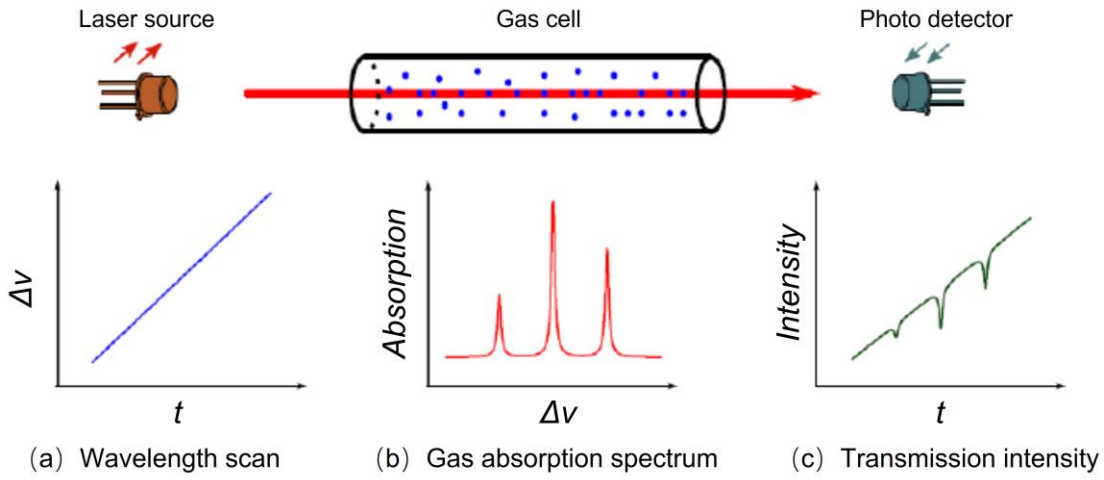

Fig. 1-5. Principle of the LAS based on the "light→sample→detector" scheme [1-10].

As one of the most commonly used LAS techniques, the "light→sample→detector" design features outstanding advantages, including compact structure, simple signal processing, and fast measurement without calibration. However, the detection concentration limit of this scheme is relatively high due to the limitation of the allowable optical path length for in-situ measurement and the influence of the electronic noise introduced from the laser source and detector, which makes it challenging to achieve detection of low-concentration or even trace isotope samples.

(2). Cavity ring-down spectroscopy technique

One straightforward way to decrease the detection concentration limit is to increase the effective optical path length (L) of the detection system. For this purpose, cavity ring-down spectroscopy (CRDS) was proposed and has become one of the most advanced LAS techniques with ultra-high detection sensitivity.

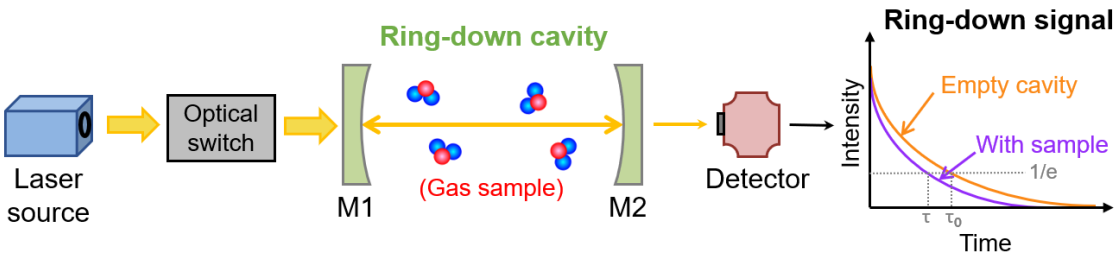

Fig. 1-6. Basic principle of cavity ring-down spectroscopy [1-11].

The basic principle of the CRDS technique is depicted in Fig. 1-6. The most important feature of CRDS is that two highly reflective mirrors with a typical reflection of R>99.99% are installed at both ends of the sample chamber, forming an optical resonator commonly referred to as the "ring-down cavity". When the laser frequency resonates with the ring-down cavity, the laser couples into the cavity and thus form a standing wave; meanwhile, the laser power received by the detector gradually increases. When the laser power reaches a set threshold, a signal is sent to the optical switch to shut off the incident laser, after which time the laser intensity within the cavity does not disappear suddenly but decays gradually. The decay signal, which is also called the "ring-down signal", can be described by:

$$P = P_0 \exp\left(t/\tau\right) \tag{1-2}$$

where P_0 represents the recorded laser power when the laser is shut off, and τ means the decay time constant, which indicates the time when the light intensity decays to 1/e of its maximum. As the laser oscillates back and forth between the two highly reflective mirrors, the cavity loss for each pass is $1-R+\alpha L$ (assuming the same reflectivity for both mirrors), which is introduced by the absorption of the sample and the transmission of the mirrors. Therefore, the decay time constant τ can be described by [1-11]:

$$\tau = \frac{L}{c\left(1-R+\alpha L\right)} \tag{1-3}$$

where L is the length of the ring-down cavity, R represents the reflectivity of cavity mirrors, and α is the absorption coefficient of the target sample. By measuring the decay times (τ and τ_0) with and without the target sample, the absorption coefficient can be obtained:

$$\alpha(\nu) = \frac{1}{c}\left(\frac{1}{\tau(\nu)} - \frac{1}{\tau_0}\right) \tag{1-4}$$

For a generic CRDS system, the minimum detectable absorption coefficient is [1-11]:

$$\alpha_{\lim} = \frac{1-R}{L} \times \frac{\Delta\tau}{\tau_0} \tag{1-5}$$

where $\Delta\tau$ means the minimum detectable time constant of the CRDS system. From this formula, it can be seen that two effective approaches to improve the detection sensitivity are to use cavity mirrors with higher reflectivity or to increase the cavity length. Additionally, the spectral linewidth of the laser source, sampling accuracy of the acquisition card, and finesse of the ring-down cavity are also important factors in

determining the sensitivity of the CRDS, which mainly affects the term $\Delta\tau/\tau_0$ in the above formula.

Essentially, CRDS is still a kind of direct absorption spectroscopy technique, but the presence of an ultra-high-finesse optical resonator significantly increases the effective optical path length from several meters in conventional "light→sample→detector" scheme to tens of kilometers, thus can significantly enhance the detection capabilities for low-concentration gas samples. Until now, the CRDS technique has gained great development, and new techniques such as optical heterodyne CRDS [1-12] and saturated absorption CRDS [1-13] have been derived one after another. Meanwhile, the sensitivity and accuracy of the detection system have been gradually improved. The current state-of-the-art CRDS systems have achieved detection sensitivity comparable to that of mass spectrometry [1-14], thus becoming one of the ideal means for isotope detection applications.

(3). Cavity-enhanced absorption spectroscopy technique

On the basis of the CRDS study, another high-sensitivity detection technique called cavity-enhanced absorption spectroscopy (CEAS) has been proposed. The basic structure of the CEAS system is very similar to that of the CRDS, as shown in Figure 1-7. The difference is that the detector in CRDS measures the decay signal of the light intensity, while the detector in CEAS measures the time-integrated light intensity transmitting through the cavity. Therefore, CEAS does not require an optical switch to control the incident laser; thus, its implementation is simpler and more convenient than CRDS.

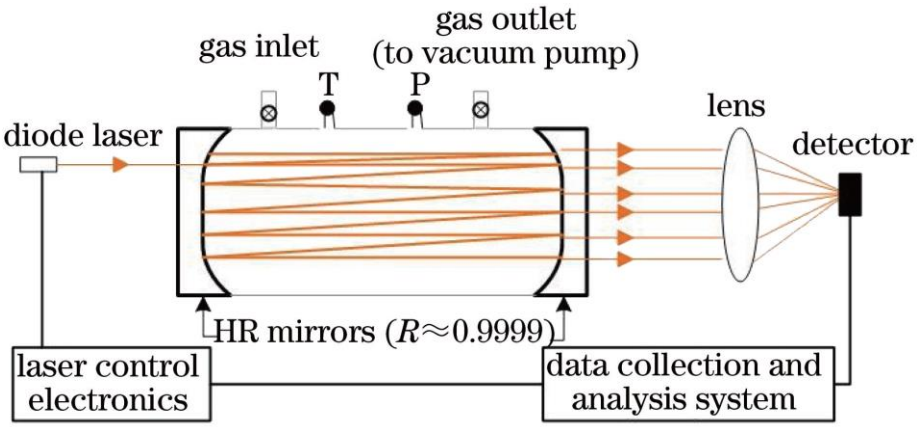

Fig. 1-7. Diagram of an off-axis cavity-enhanced absorption spectroscopy system [1-15].

As the principle of CEAS has been described in detail in several papers [1-16], here we only review the important formulas related to CEAS measurements. The core of CEAS remains the Beer-Lambert law, but the presence of highly reflective mirrors confines the laser within the cavity to experience multiple roundtrips, resulting in a significant increase in the effective optical path length and hence enhancement of the laser absorption signal. For the measurement of weakly absorbing samples using CEAS, the transmitted light intensity (I_t) can be described by [1-17]:

$$\frac{I_t}{I_0}=\frac{(1-R)^2\exp(-\alpha L)}{\left(1-\mathrm{R}\exp(-\alpha L)\right)^2}\approx\frac{\left(1-R\right)^2\left(1-\alpha L\right)}{\left(1-R+R\alpha L\right)^2}=\frac{1-\alpha L}{\left(1+\frac{R\alpha L}{1-R}\right)^2}\approx 1-\frac{1+R}{1-R}\alpha L=1-\alpha L_{eff} \quad (1\text{-}6)$$

where R represents the reflectivity of the cavity mirror, L represents the cavity length, and L_{eff} indicates the effective optical path length. Therefore, an approximation of the effective optical path length and the absorption coefficient can be derived by:

$$L_{eff}=\frac{1+R}{1-R}L\approx\frac{2}{1-R}L \quad (1\text{-}7)$$

Then the absorption coefficient α can be calculated simply by:

$$\alpha=\frac{1}{L}\left|\ln\left(\frac{1}{2R^2}\left(2R+\frac{I_0}{I_t}\left(1-R\right)^2-\sqrt{4\frac{I_0}{I_t}R\left(1-R\right)^2+\frac{I_0^2}{I_t^2}\left(1-R\right)^2}\right)\right)\right|\approx\frac{1}{L}\left(\sqrt{\frac{I_0}{I_t}}-1\right)\left(1-R\right) \quad (1\text{-}8)$$

It can be seen that, similar to the CRDS technique, the detection concentration limit of a CEAS system can also be reduced by increasing the resonator (L) length and the reflectivity (R) of the cavity mirror. In addition, the CEAS technique requires a high-power laser source to minimize the influence of electronic noise on the detection sensitivity.

CEAS has become one of the representative techniques in the field of LAS and has been widely used for atmospheric isotope measurements [1-18], breath analysis [1-19], and laser diagnostics [1-20]. Meanwhile, the CEAS technique is constantly evolving. To reduce the laser coupling noise and maximize the transmitted laser intensity, off-axis CEAS [1-21] and three-mirror off-axis CEAS [1-22] have been developed, enabling further improvements in the signal-to-noise ratio and hence the detection sensitivity. Currently, CEAS has gradually developed towards higher detection sensitivity, faster response time, and more compact and portable structures.

1.3 Requirements of Lasers for Water Isotope Detection

For an LAS system, the laser light source is the core component that determines the applicable detection technique, the versatility and flexibility, as well as the ultimate detection sensitivity and resolution of the detection system. Thus, there are many requirements for the laser sources to achieve in-situ measurement of water isotopes with a high signal-to-noise ratio. Here we describe the basic output characteristics that an ideal laser source should possess according to the absorption spectra of water isotopes and the requirements of a high-sensitivity detection system.

(1). Laser wavelength

In a molecule, the electrons occupy discrete energy levels around the atomic nuclei. These energy levels are determined by the molecule's electronic structure, which is influenced by the atomic arrangement and the interactions between adjacent atoms. When a molecule interacts with light, such as a laser beam, the electrons can undergo transitions between these energy levels by absorbing photons. Thus, each molecule shows a characteristic set of absorption lines on the electromagnetic spectrum.

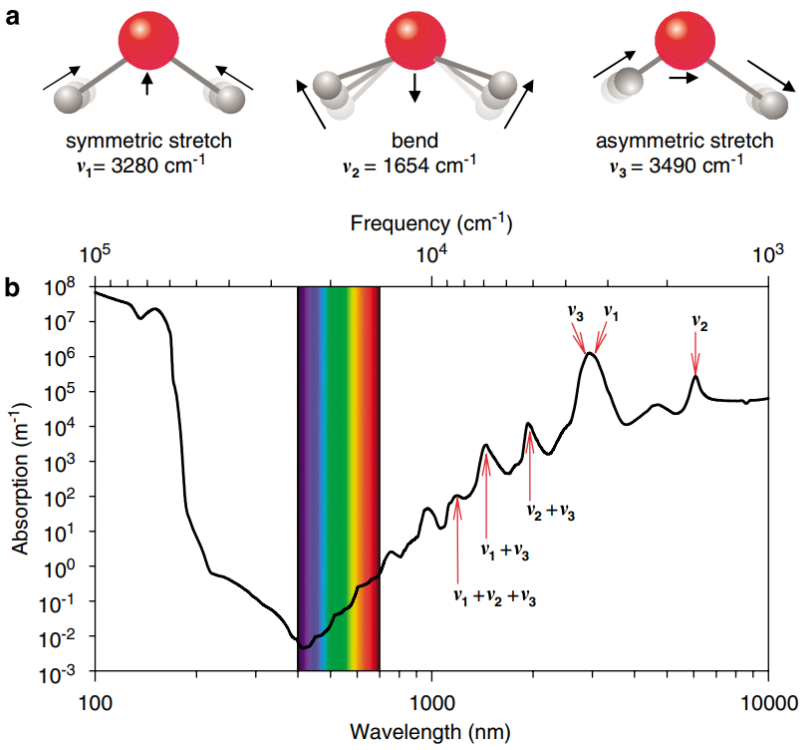

Fig. 1-8. Absorption spectrum of pure H_2O molecules [1-23].

For the detection of water isotopes (H_2O, HDO, and HTO, etc.) using LAS, the most suitable laser wavelength should be the mid-infrared band, particularly the 3–5 μm region, because the absorption peaks of water isotopes are exactly located within this band. Figure 1-8 shows the absorption spectrum of pure water (H_2O). It can be seen that the strongest absorption band, which corresponds to the stretching vibrational modes of the H_2O molecule, is located at around 3 μm. For water isotopes, the hydrogen atoms are replaced by heavier deuterium or tritium atoms. Consequently, their molecular vibrations are shifted to other frequencies, leading to different absorption bands. According to references [1-24] and [1-25], the strongest absorption peaks of HDO and HTO are shifted to ~3.7 μm and 4.5 μm, respectively, as shown in Fig. 1-9.

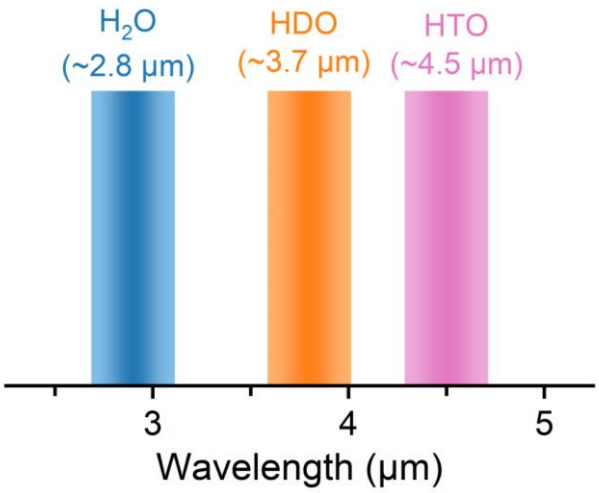

Fig. 1-9. Absorption band of water isotopes according to references [1-24] and [1-25].

Therefore, in terms of the laser wavelength, a laser source operating in the 3–5 μm spectral region is required, as it can match the strongest absorption lines of the target sample, thus enabling accurate measurements of low-concentration samples. Further, matching the absorption peaks of molecules can help to shorten the optical path length required for high-sensitivity measurement, thereby reducing the size of the entire system and achieving a portable detection system.

(2). Spectral linewidth

For most gas-phase molecules at room temperature, their absorption linewidths are typically on the order of a few wavenumbers (cm^{-1}). It has been reported that the HTO molecule shows a typical linewidth of approximately 0.02 cm^{-1} at 2388 cm^{-1} (as shown in

Fig. 1-10), corresponding to a linewidth in wavelength of approximately 35 pm at 4.2 μm [1-26]. Therefore, a narrow-linewidth laser source with its spectral linewidth narrower than the absorption linewidth of the target sample is generally required to match the laser wavelength to a specific absorption peak for high-precision detection.

At first, using a narrow-linewidth laser allows for better spectral resolution and thus can accurately measure the positions and intensities of absorption peaks. Further, precisely matching the laser wavelength to a particular absorption line can reduce interference from other background gases or contaminants, enabling targeted investigations of specific molecular or atomic species. From the perspective of the light source, lasers with narrow-linewidth outputs typically have excellent frequency stability, which can improve the repeatability and reproducibility of measurements over time.

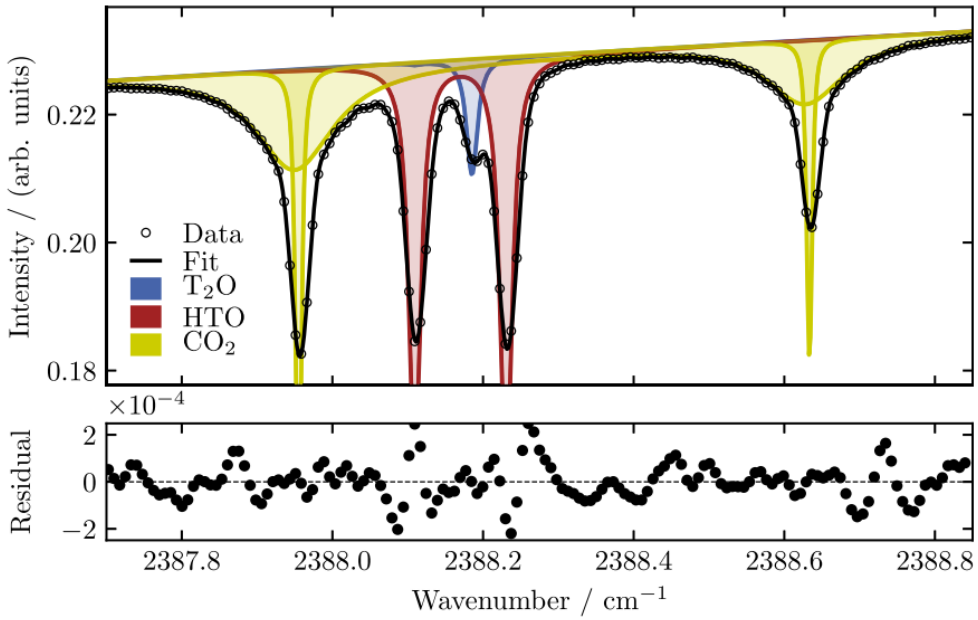

Fig. 1-10. Typical absorption lines of HTO and T_2O at ~4.2 μm. [1-26]

(3). Tuning capability

As each molecule has many possible energy transitions, it generally shows multiple discrete absorption lines enveloped within multiple absorption bands. Moreover, different molecules may have same transition energies, resulting in overlaps between their absorption bands. For example, figure 1-11 shows the high-resolution spectra of water isotopes with CO_2 and N_2O at ~3.65 μm. In this band, we can observe large amounts of

overlaps between the absorption lines of water isotopes and CO_2. These overlaps make it difficult to identify the source of the absorption signal during spectroscopic measurements.

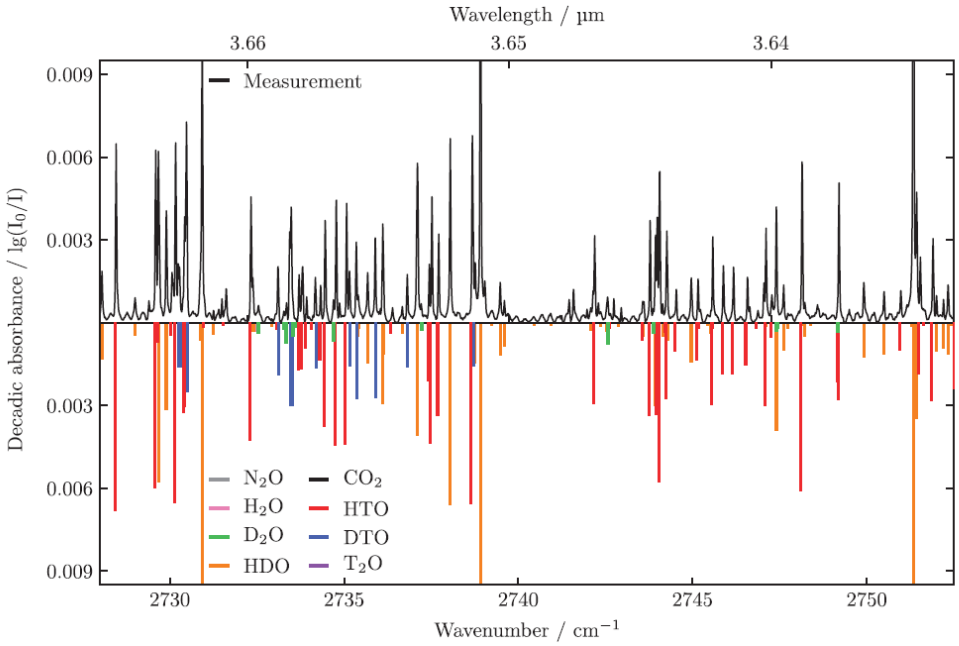

Fig. 1-11. High-resolution absorption spectra of water isotopes [1-27].

Therefore, in cases where multiple molecules or compounds are present in the sample, it is necessary to select the laser wavelength that can merely excite the desired target sample, which can avoid the absorption signal from interfering molecules. This suggests that the laser source should be widely tunable in lasing wavelength. The ability of precise wavelength tuning can resolve fine spectral details and distinguish closely spaced absorption lines. Additionally, using a widely tunable laser source allows the detection of multiple gas samples with the use of only one light source, which can significantly improve the versatility and adaptability of the detection system.

(4). Laser output power

Laser output power is another critical parameter that affects the performance of LAS detection. As LAS detection relies on measuring the attenuation of laser when passing through the sample, a higher laser power can provide a stronger initial signal and hence a larger measurable absorption signal, resulting in higher detection sensitivity and signal-to-noise ratio. In addition, for the laser-matter interaction process, a high-power laser provides a higher photon flux and thus increases the likelihood of absorption events, which can

improve the probability of interaction between the laser and the sample. Therefore, a lower laser power can be used when measuring strongly absorbing or high-concentration samples; while for weakly absorbing or trace-level samples, a higher laser power is generally required to achieve a sufficient signal-to-noise ratio.

In addition, a higher laser power allows for faster sampling and data acquisition while also reducing the sensitivity requirements of the detector, which is advantageous when studying dynamic processes or time-sensitive measurements. Also, for certain applications, such as remote sensing or non-contact detection [1-28], it is required to perform LAS measurements from a distance. A high-power laser can then transmit longer distances and still provide sufficient intensity for interaction with the sample.

In any case, a higher laser output power is desirable because it enables a wider dynamic range and thus can meet the requirements of various specific applications.

To sum up, the basic requirements for laser sources to achieve high-resolution and high-sensitivity water isotope detection should be high output power, narrow spectral linewidth, and widely tunable in the 3–5 μm mid-infrared spectral region. Therefore, the main objective of my Ph.D. project is to develop such high-performance mid-infrared lasers to advance the development of optical isotope detection systems.

1.4 Dissertation Organization

This dissertation presents several state-of-the-art mid-infrared lasers developed during my Ph.D. studies. I focused on the exploration of experimental techniques to develop laser systems capable of combining high power, narrow linewidth, and widely tunable abilities in one, which is rather difficult to achieve for conventional lasers. The remainder of the dissertation is organized with a chapter for 3-μm laser development, two chapters for 4-μm laser development, a chapter for water isotope detection, and a chapter to summarize the work. The main content of each chapter is briefly described as follows:

(1). 3-μm Laser Development Based on Er:YAP Crystal

This study aims to explore the power scaling technique of 3-μm lasers based on Er-doped bulk materials. We propose a scheme that cryogenically cools an Er:YAP crystal to

improve its 3-μm laser performance. The spectral properties and laser performance of Er:YAP at different cooling temperatures were investigated for the first time. The results prove that cryogenically cooling the Er:YAP can significantly improve its laser performance and is a promising approach to breaking the current power record of 3-μm lasers. Further, we demonstrate that the Er:YAP laser is wavelength-tunable and can emit narrow spectral linewidth with watt-level output power, indicating that it is an excellent laser source for water isotope detection.

(2). 4-μm Fe:ZnSe Laser Oscillator End Pumped by an Er:YAP Laser

This chapter presents a novel development of a 4-μm laser based on an Er:YAP-laser-pumped Fe:ZnSe oscillator design. Fe:ZnSe is an excellent gain medium for direct generation of 4-μm lasers; however, the development of Fe:ZnSe lasers is limited by the lack of reliable high-power 3-μm pump sources. Thus, in this work we propose to use our self-developed Er:YAP laser as the pump source for Fe:ZnSe to achieve an efficient and compact 4-μm laser source. The Fe:ZnSe oscillator produced a maximum output power of 1 W with an overall optical conversion efficiency of 8.8%, which is the highest efficiency reported thus far. This study shows that the Er:YAP laser can serve as an excellent pump source of Fe:ZnSe to generate high-efficiency 4-μm lasers.

(3). Hybrid Fe:ZnSe Amplifier for High-power, Narrow-linewidth, and Widely Tunable MIR Laser

This study proposes a novel laser design to address the difficulties of precise spectral control in Fe:ZnSe oscillators based on a hybrid Fe:ZnSe amplifier seeded by a quantum cascade laser (QCL). The laser wavelength is entirely determined by the QCL, while the Fe:ZnSe only amplifies the laser power while keeping the spectrum unchanged. We demonstrated a record high-power, pure single-frequency laser operating at 4.3 μm and a high-power, narrow-linewidth, and widely tunable laser with a tuning range of 630 nm by using the hybrid Fe:ZnSe amplifier designs. This work opens a new avenue for the development of MIR lasers with a high power spectral density using Fe:ZnSe. The proposed laser systems can meet the requirements of high-sensitivity spectroscopy applications and are well-suited for real-time, in-situ detection of water isotopes in nuclear fusion reactors.

(4). Preliminary Study on Water Isotope Detection Using Mid-infrared Laser

This study aims to develop a compact, portable, and on-site usable system for water isotope detection. We propose to use commercial 6.3-μm and 7.4-μm QCLs as the detection light sources because the 6–7 μm band can avoid the atmospheric CO_2 absorption and corresponds to the second strongest absorption peak of the water isotope. In this preliminary experiment, a detection setup based on the conventional "light source→sample →detector" scheme was constructed, and the characteristic absorption peaks of H_2O, HDO, and $H_2{}^{18}O$ were successfully calibrated, demonstrating that this compact and portable detection system can be used for real-time, in-situ measurement applications.

References (Chapter I)

[1-1]. S. Holzner, “Physics I for dummies,” John Wiley & Sons (2022).

[1-2]. H. S. Bosch, G. M. Hale, “Improved formulas for fusion cross-sections and thermal reactivities,” Nuclear Fusion, **32**(4), 611 (1992).

[1-3]. M. Rubel, “Fusion neutrons: tritium breeding and impact on wall materials and components of diagnostic systems,” Journal of Fusion Energy, **38**(3-4), 315–329 (2019).

[1-4]. 小西哲之. 核融合動力プラントの安全性についての考察, プラズマ・核融合学会誌, **78**(11), 1157–1164 (2002).

[1-5]. R. E. Ellefson, W. E. Moddeman, and H. F. Dylla, “Hydrogen isotope analysis by quadrupole mass spectrometry,” Journal of Vacuum Science and Technology, **18**(3), 1062–1067 (1981).

[1-6]. R. A. Sigg, J. E. McCarty, R. R. Livingston, and M. A. Sanders, “Real-time aqueous tritium monitor using liquid scintillation counting,” Nuclear Instruments and Methods in Physics Research Section A: Accelerators, Spectrometers, Detectors and Associated Equipment, **353**(1-3), 494–498 (1994).

[1-7]. https://www.sanken.osaka-u.ac.jp/labs/cac/souchi-ms_c.html

[1-8]. http://www.hrc.u-toyama.ac.jp/en/about/facility/facility11.html

[1-9]. D. F. Swinehart, “The Beer-Lambert Law,” Journal of chemical education, **39**(7), 333 (1962).

[1-10]. H. He, S. Gao, J. Hu, T. Zhang, T. Wu, Z. Qiu, C. Zhang, Y. Sun, S. He, “In-situ testing of methane emissions from landfills using laser absorption spectroscopy,” Applied Sciences, **11**(5), 2117 (2021).

[1-11]. S. Maithani, M. Pradhan, “Cavity ring-down spectroscopy and its applications to environmental, chemical and biomedical systems,” Journal of Chemical Sciences, **132**, 1–19 (2020).

[1-12]. Y. He, B. J. Orr, “Rapidly swept, continuous-wave cavity ringdown spectroscopy with optical heterodyne detection: single-and multi-wavelength sensing of gases,” Applied Physics B, **75**, 267–280 (2002).

[1-13]. G. Giusfredi, S. Bartalini, S. Borri, P. Cancio, I. Galli, D. Mazzotti, and P. D. Natale, "Saturated-absorption cavity ring-down spectroscopy," Physical Review Letters, **104**(11), 110801 (2010).

[1-14]. I. Galli, S. Bartalini, R. Ballerini, M. Barucci, P. Cancio, M. D. Pas, G. Giusfredi, D. Mazzotti, N. Akikusa, and P. D. Natale, "Spectroscopic detection of radiocarbon dioxide at parts-per-quadrillion sensitivity," Optica, **3**(4), 385–388 (2016).

[1-15]. K. B. Hewett, J. E. McCord, M. Gupta, and T. Owano, "Measuring the yield of singlet oxygen in a chemical oxygen iodine laser," International Symposium on Gas Flow, Chemical Lasers, and High-Power Lasers. SPIE, **6346**, 129–135 (2007).

[1-16]. D. Romanini, I. Ventrillard, G. Méjean, J. Morville, E. Kerstel, "Introduction to cavity enhanced absorption spectroscopy," Cavity-Enhanced Spectroscopy and Sensing, 1–60 (2014).

[1-17]. X. Chao, Z. Hu, and N. Zhu, "Research and Application Progress of Cavity-enhanced Absorption Spectroscopy," Acta Photonica Sinica, **52**(3), 0352102 (2023)

[1-18]. L. Han, H. Xia, T. Pang, Z. Zhang, B. Wu, S. Liu, P. Sun, X. Cui, Y. Wang, M. W. Sigrist, F. Dong, "Frequency stabilization of quantum cascade laser for spectroscopic CO_2 isotope analysis," Infrared Physics & Technology, **91**, 37–45 (2018).

[1-19]. I. Bayrakli, H. Akman, and F. Sari, "High-sensitivity biomedical sensor based on photoacoustic and cavity enhanced absorption spectroscopy with a new software platform for breath analysis," Applied Optics, **60**(7), 2093–2099 (2021).

[1-20]. K. Sun, S. Wang, R. Sur, X. Chao, J. B. Jeffries, and R. K. Hanson, "Time-resolved in situ detection of CO in a shock tube using cavity-enhanced absorption spectroscopy with a quantum-cascade laser near 4.6 μm," Optics Express, **22**(20), 24559–24565 (2014).

[1-21]. P. Malara, P. Maddaloni, G. Gagliardi, and P. D. Natale, "Combining a difference-frequency source with an off-axis high-finesse cavity for trace-gas monitoring around 3 μm," Optics Express, **14**(3): 1304–1313 (2006).

[1-22]. R. Centeno, J. Mandon, S. M. Cristescu, and F. J. M. Harren, "Three mirror off axis integrated cavity output spectroscopy for the detection of ethylene using a quantum cascade laser," Sensors and Actuators B: Chemical, **203**, 311–319 (2014).

[1-23]. M. Stomp, J. Huisman, L. J. Stal, H. C. P. Matthijs, “Colorful niches of phototrophic microorganisms shaped by vibrations of the water molecule,” The ISME journal, **1**(4), 271–282 (2007).

[1-24]. J. G. Bayly, V. B. Kartha, and W. H. Stevens, “The absorption spectra of liquid phase H_2O, HDO and D_2O from 0.7 μm to 10 μm,” Infrared Physics, **3**(4), 211–222 (1963).

[1-25]. M. J. Down, J. Tennyson, M. Hara, Y. Hatano, and K. Kobayashi, “Analysis of a tritium enhanced water spectrum between 7200 and 7245 cm^{-1} using new variational calculations,” Journal of Molecular Spectroscopy, **289**, 35–40 (2013).

[1-26]. J. Reinking, V. Hermann, J. Müller, M. Schlösser, F. Hase, and J. Orphal, “The fundamental ν_3 band of DTO and the $2\nu_1$ overtone band of HTO from the analysis of a high-resolution spectrum of tritiated water vapour,” Journal of Molecular Spectroscopy, **370**, 111295 (2020).

[1-27]. J. Reinking, M. Schlösser, F. Hase, and J. Orphal, “First high-resolution spectrum and line-by-line analysis of the $2\nu_2$ band of HTO around 3.8 microns,” Journal of Quantitative Spectroscopy and Radiative Transfer, **230**, 61–64 (2019).

[1-28]. B. M. Walsh, H. R. Lee, N. P. Barnes, “Mid infrared lasers for remote sensing applications,” Journal of Luminescence, **169**, 400–405 (2016).

II. 3-μm Laser Development Based on Er:YAP Crystal

2.1 Research Status and Problem Statement

3-μm lasers are ideally suited for water isotope detection because the 3-μm band corresponds exactly to the strongest stretching vibrational absorption peaks of the hydroxyl group [2-1]. However, obtaining a high-power 3-μm laser is not easy due to the inherently large quantum defect in the energy conversion from near- to mid-infrared photons. Laser diode (LD) pumped Erbium-doped lasers demonstrate unique advantages among 3-μm lasers in terms of their compactness, power scaling capacity, and high wall-plug efficiency [2-2][2-3]. Among them, the Er:ZBLAN fiber laser shows the most preferable power scaling ability, which could deliver up to 41.6 W output power at ~3 μm [2-4]. However, due to the low mechanical strength of ZBLAN soft glass and the property of water absorption on the fiber tips, Er:ZBLAN fibers are extremely difficult to handle and have a low durability [2-5]. Thus, significant efforts have also been made to develop Er-doped bulk materials with higher mechanical strength and robustness. Recently, Er-doped crystals or ceramics with low phonon energies, such as Er:YAP [2-6], Er:Y_2O_3 [2-7], and Er:Lu_2O_3 [2-8], have emerged as alternative candidates for the power scaling of 3-μm lasers, and various methods have been developed to improve the power-scaling ability of these materials. Nevertheless, the output power of Er-doped bulk lasers still cannot exceed that of Er fiber lasers due to the difficulty of thermal management. Effective thermal management of laser gain media is urgently needed to further scale up the output power of 3-μm Er lasers.

Cryogenically cooled lasers are an advanced technique for the development of high-power lasers [2-9], given that the thermo-mechanical properties of laser gain materials exhibit significant improvements at low temperatures. This feature is quite attractive for 3-μm Er-doped bulk lasers because thermal effects (the thermal lensing effect and thermally induced wavefront distortion) and the subsequent material damage are the primary limitations to their power scaling behaviors. In addition, lasing ability of the gain material can be significantly improved at low temperatures. In 2010, a cryogenic sesquioxide

Er:Y_2O_3 ceramic laser was reported by T. Sanamyan et al., which generated an output power of 14 W and a slope efficiency of 26% at 2.7 μm [2-10]. In 2016, detailed spectroscopic properties of a cryogenic Er:Y_2O_3 ceramic were reported by the same group, and the output power of 24 W represents the highest output power reported from a 3-μm Er-doped solid-state laser [2-11]. The significant improvement in the output power demonstrates the great potential of the cryogenic lasers to break the current power record of 3-μm mid-infrared lasers. As an alternative laser material for 3-μm lasers, Er:YAP crystal possesses low phonon energy (550 cm^{-1}) and excellent mechanical properties. The thermal shock resistance of YAP is significantly higher than that of a typical garnet host material such as YAG [2-6], thus indicating its potential for high-power laser operation. Significant progress was reported with respect to mid-infrared Er:YAP lasers operating at room temperature. In 2018, the temperature-dependent spectroscopic properties of a low-doped Er:YAP crystal (1 at.% of Er^{3+}) were presented by R. Svejkar et al., and the results revealed higher output powers and slope efficiencies at cryogenic cooling temperatures than at room temperature [2-12]. However, the Er:YAP used in that study was not optimized in terms of the doping concentration and crystal length; thus, the continuous wave (CW) output power was limited to 27 mW with a slope efficiency of only 3.5%. The spectroscopic properties of the highly doped Er:YAP crystal, in addition to its laser performance under cryogenic conditions, therefore require investigation for the further power scaling of the 3-μm lasers.

In this study, we aim to measure the spectroscopic properties of a highly doped Er:YAP crystal at cooling temperatures ranging from 77–290 K and study its laser performance to analyze the reasons limiting the power scaling of a cryogenic Er:YAP laser. The proposed cryogenic Er:YAP laser can produce watt-level output power at ~2.8 μm, which is approximately two orders of magnitude higher than the results reported in [2-12]. When the Er:YAP was cooled from 290 K to 77 K, the laser slope efficiency increased by a factor of 1.4 over that obtained at room temperature, indicating that cryogenically cooling the gain medium can effectively improve the 3-μm laser performance of the Er:YAP. More importantly, we demonstrate that the Er:YAP laser is wavelength-tunable by controlling the cooling temperature and laser power, and explain the underlying reasons for this. Finally, the main factors limiting the laser power and efficiency are discussed.

2.2 Spectroscopy of Cryogenically Cooled Er:YAP

2.2.1 Absorption Spectroscopy

The spectroscopic properties of the Er:YAP crystal, including its absorption spectrum and fluorescence lifetime, were first investigated to anticipate possible lasing behaviors. Figure 1 shows the experimental setup built for the absorption spectrum measurement. An Er:YAP crystal (*b*-cut, space group: *Pbnm*, ordered from CRYTUR) with a doping concentration of 5 at.% was used. This 5 at.% doping concentration was chosen because it demonstrated excellent laser efficiency at room temperature in our group's previous study [2-6]; meanwhile, it was a relatively low doping concentration among all reported 3-μm Er:YAP lasers operating at room temperature [2-13][2-14], which implies a good balance between thermal effects and laser efficiency during lasing process. The crystal had a cross-section of 2 mm × 5 mm and a length of 8 mm. It was wrapped in a piece of indium foil with a thickness of 0.1 mm and mounted in a liquid-nitrogen-cooled copper heat sink for temperature control. Two anti-reflective (AR) windows were used for the cryostat, and the pressure of the vacuum chamber was kept below 1.5 mTorr. A super-continuum (SC) light source (WhiteLase micro, FIANIUM) was used as the probe light, and an optical spectrum analyzer (Q8381A, ADVANTEST) with a resolution of 0.1 nm was used to measure the transmitted spectra of the SC light. The absorption spectra were derived by comparing the transmitted spectra with and without the Er:YAP crystal.

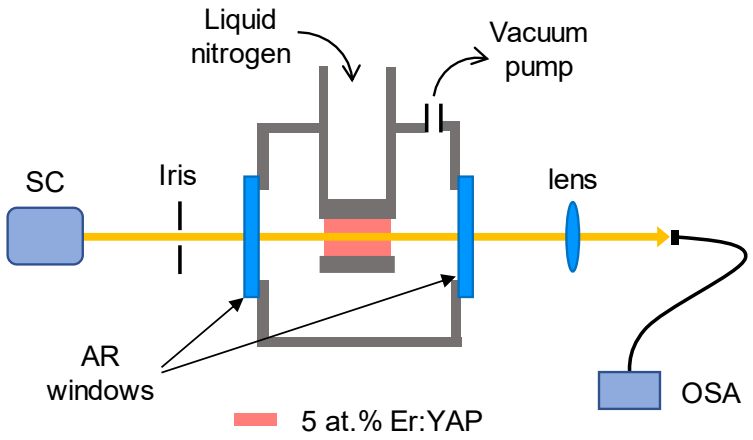

Fig. 2-1. Experimental setup for the absorption spectrum measurement.

Figure 2 shows the measured absorption spectra of the Er:YAP crystal at 290 K and 77 K. It should be noted that the Er:YAP crystal exhibits an anisotropic structure, such that the measured absorption spectrum is the averaged result of polarized absorption along the *a* and *c*-axes of the crystal. At 290 K, the absorption spectrum covered a broad band from 960–1020 nm, and the absorption coefficient at 976 nm, which corresponds to the pumping wavelength of the LD, was 1.5 cm^{-1}. When the crystal was cryogenically cooled to 77 K, the absorption spectrum narrowed with a band from 960 nm to less than 1000 nm, and the absorption coefficient at 976 nm decreased to 0.5 cm^{-1}. These changes in the spectral shape and overall reduction in the absorption coefficient at 77 K can be attributed to the influence of the temperature-dependent Boltzmann factor. This result indicates that a higher incident pump power is necessary to achieve a watt-level laser output due to the decreased absorption coefficient at low temperatures.

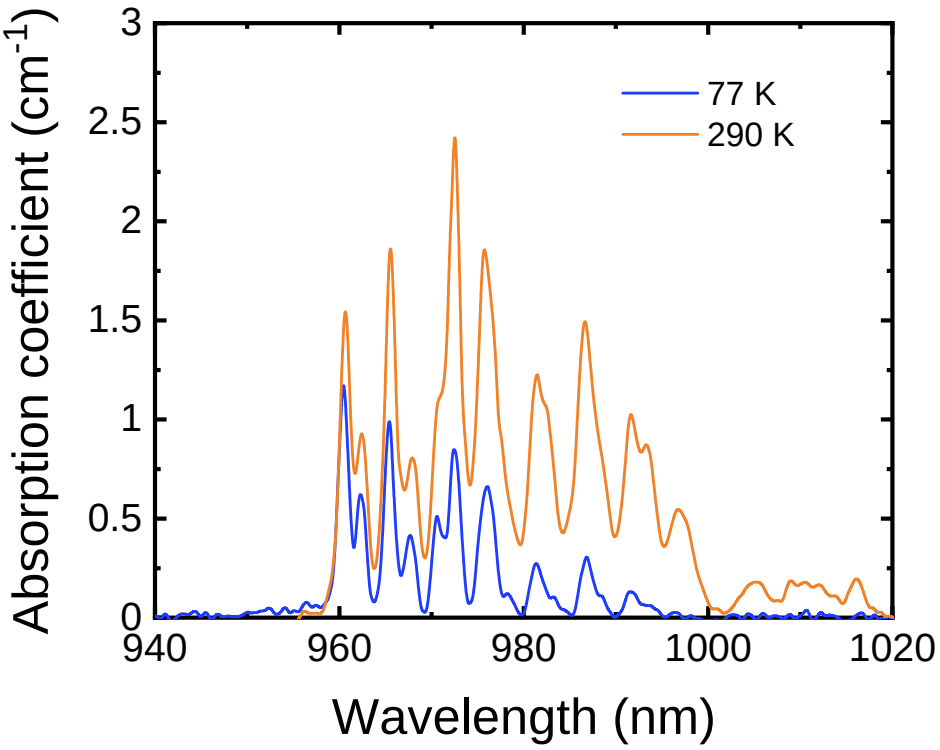

Fig. 2-2. Absorption spectra of Er:YAP measured at 77 K and 290 K.

2.2.2 Fluorescence Lifetime

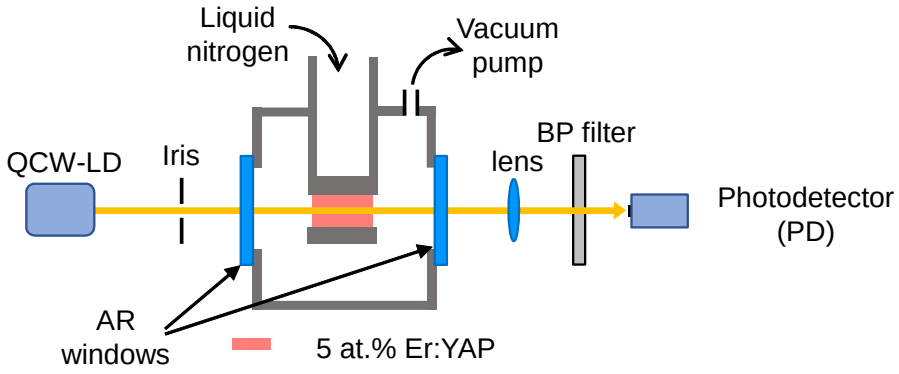

Fig. 2-3. Experimental setup for the fluorescence lifetime measurement.

Fluorescence lifetime is an important parameter that describes the energy storage capacity and lasing ability of the gain material. We then constructed a setup shown in Fig. 2-3 to measure the fluorescence lifetime of the Er:YAP at different cooling temperatures. The Er:YAP crystal was excited by a quasi-CW modulated 976-nm LD with a 100-μs pulse width at different cooling temperatures from 77–290 K. Two high-speed photodetectors working at 1.5 μm (PDA20H-EC, THORLABS) and 3 μm (PVI-4TE-4-1×1, VIGO SYSTEM) were used to detect the fluorescence decay signals from $^4I_{13/2}$ and $^4I_{11/2}$ multiplets, which correspond to the transitions from the lower laser level and upper laser level, respectively. The fluorescence lifetimes can be derived by fitting these decay signals using a single exponential decay function: $I(t) = I_0 \cdot \exp(-t/\tau_f)$ [2-15]. Typical decay signals with their fitting curves are shown in Fig. 2-4.

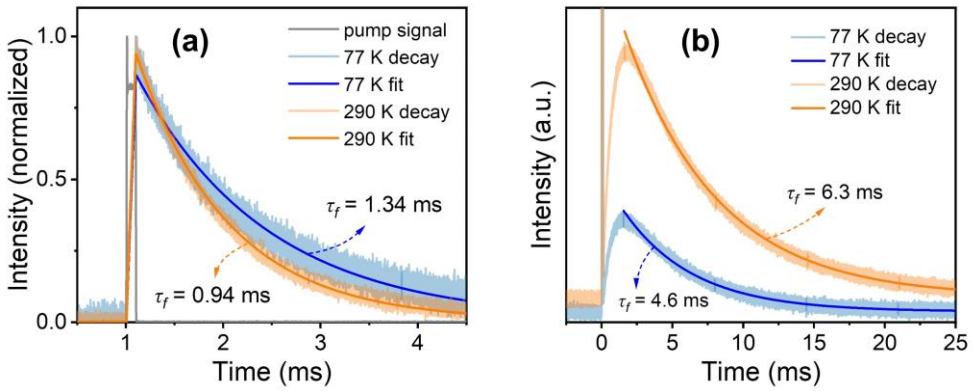

Fig. 2-4. Decay signals of transitions from (a) upper laser level and (b) lower laser level.

Figure 2-5 summarizes the fitted fluorescence lifetimes of the upper laser level ($^4I_{11/2}$) and lower laser level ($^4I_{13/2}$) at cooling temperatures ranging from 77–290 K. It can be seen that the fluorescence lifetime of the $^4I_{11/2}$ multiplet gradually decreased from 1.34 ms to 0.94 ms; whereas, the lifetime of the $^4I_{13/2}$ multiplet increased from 4.61 ms to 6.27 ms when the cooling temperature was increased from 77 K to 290 K. In general, the number of phonons in the crystal should decrease as the cooling temperature decreases, thus leading to weak multi-phonon coupling. As such, the lifetime of the $^4I_{11/2}$ multiplet was expected to increase slightly at low temperatures. However, the energy gap between the $^4I_{13/2}$ multiplet and the ground state $^4I_{15/2}$ is quite large (see inset of Fig. 2-5), such that the lifetime of the $^4I_{13/2}$ multiplet was not significantly influenced by the non-radiative transition driven by multi-phonon coupling. Therefore, we attributed the decreased lifetime of the $^4I_{13/2}$ level to the enhanced energy transfer up-conversion (ETU in Fig. 2-5) effect at lower cooling temperatures, which was particularly pronounced for a relatively high-doped crystal [2-16], thus depopulating the $^4I_{13/2}$ multiplet and resulting in a decreased fluorescence lifetime. Therefore, we can conclude from the spectroscopic studies that the low operating temperature is beneficial for population inversion and hence the 3-μm laser transition.

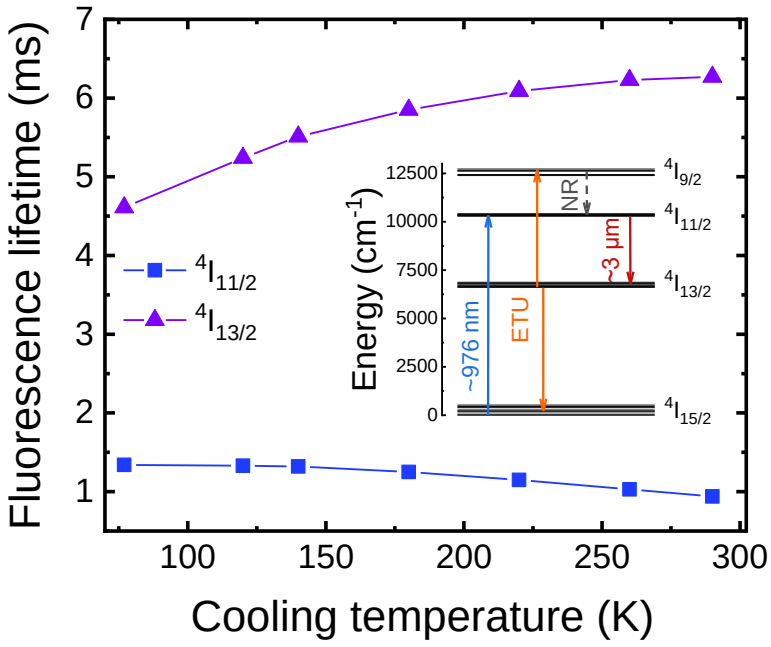

Fig. 2-5. Fluorescence lifetimes of the upper and lower laser levels of Er:YAP at different cooling temperatures. Inset: energy level diagram of Er:YAP [2-17].

2.3 Laser Performance of Cryogenically Cooled Er:YAP

2.3.1 Cryogenic Er:YAP Laser Setup

To test the laser performance of the cryogenically cooled Er:YAP, we constructed a laser setup based on a compact plane-plane resonator design, as shown in Fig. 2-6. A 976-nm fiber-coupled and wavelength-stabilized LD (K976AAHRN-27.00WN0N-10522F10ENA, BTW) served as the pump source, the fiber of which had a core diameter of 105 μm and numerical aperture of 0.22. The pump light was focused into the crystal with a waist diameter of ~390 μm using a 4:15 telescope system. The Er:YAP crystal was mounted on a liquid-nitrogen-cooled copper heatsink inside a cryostat and cooled to 77 K. A plane input mirror (IM, high transmission at 960–980 nm, and high reflectivity at 2.6–3 μm) and a sapphire plate (AR coated at 2.9 μm) were employed as the cryostat windows. A plane output coupler (OC) was placed behind the sapphire window, thus forming a compact linear cavity. With this arrangement, the total cavity length was measured to be 25 mm. Three OCs with transmissions of T = 1%, T = 2.5%, and T = 5% were used to optimize the laser performance. A bandpass filter was used to block residual pump light from the laser output to measure the laser power accurately.

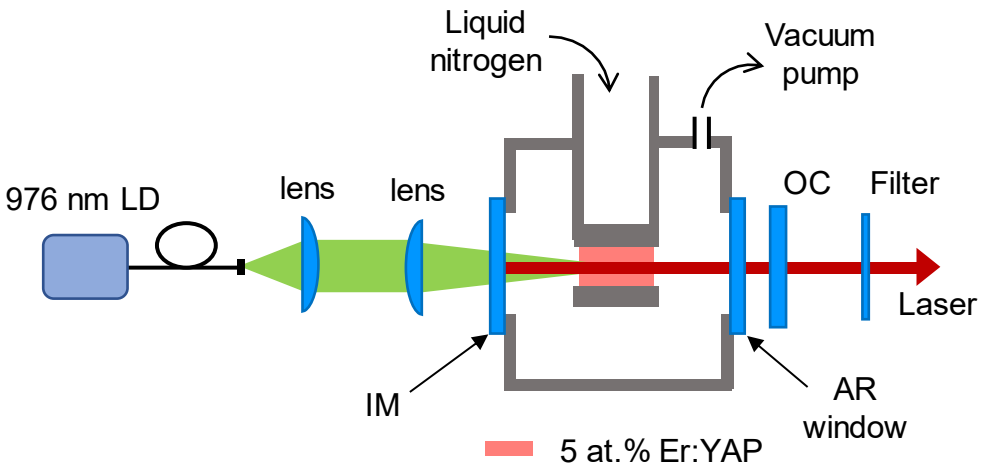

Fig. 2-5. Experimental setup of the cryogenically cooled Er:YAP laser.

2.3.2 Laser Output Characteristics

First, we examined the pump absorption of the Er:YAP crystal using the 976-nm LD. At room temperature, the single-pass pump absorption was measured to be approximately 71%, corresponding to an absorption coefficient of 1.55 cm^{-1}, which was almost the same as the above measurement result in Fig. 2-2, thus confirming the accuracy of the experiment on absorption spectrum measurement. Therefore, for laser experiments at cryogenic conditions, we used the measured single-pass absorption coefficient (0.5 cm^{-1}) to evaluate the absorbed pump power (i.e., 33% of the incident pump power). This evaluation is reasonable because the ground-state bleaching effect can be neglected due to the high Er^{3+}-ion doping concentration.

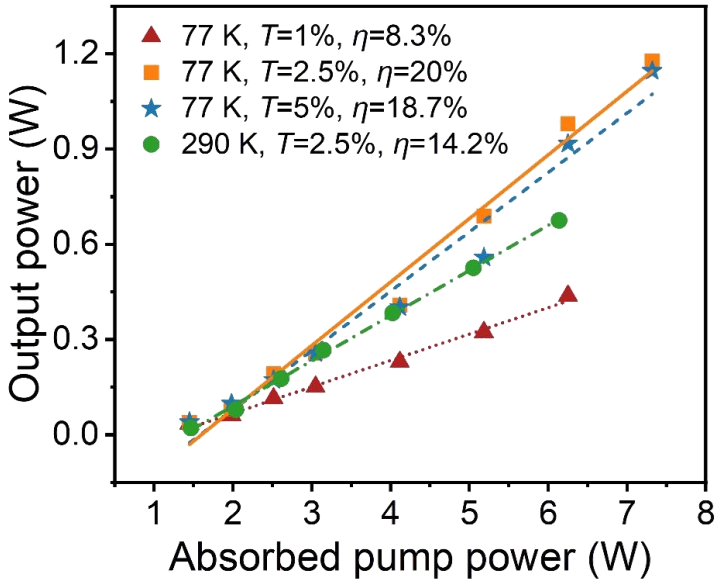

Fig. 2-6. Er:YAP laser output power versus absorbed pump power.

Figure 2-6 shows the Er:YAP laser output power as a function of the absorbed pump power for using three OCs at 77 K and T = 2.5% at 290 K. The best laser performance was obtained when the output coupling transmission T = 2.5%. As the cooling temperature decreased, the laser slope efficiency increased by a factor of 1.4, from approximately 14% at room temperature to 20% at 77 K. This result proves that cryogenically cooling the Er:YAP can significantly enhance its laser performance. The cryogenic Er:YAP laser produced a maximum output power of 1.2 W without thermal rollover, indicating that

further increase in the laser power to multi-watt power levels is possible. However, it is limited by the available absorbed pump power due to the weak pump absorption at 77 K, thus suggesting that using a longer crystal or shifting the pump laser spectrum to a shorter wavelength (i.e., ~960 nm) is a potential solution for future studies. Furthermore, compared to the results reported in [2-12], we successfully scaled up the laser power by two orders of magnitude. This power improvement can be attributed to the use of a relatively highly doped Er:YAP crystal, which enables a larger quantum efficiency due to the enhanced energy transfer up-conversion at a high doping concentration [2-18]. The power fluctuation of the Er:YAP laser was monitored to be less than 5% within one hour.

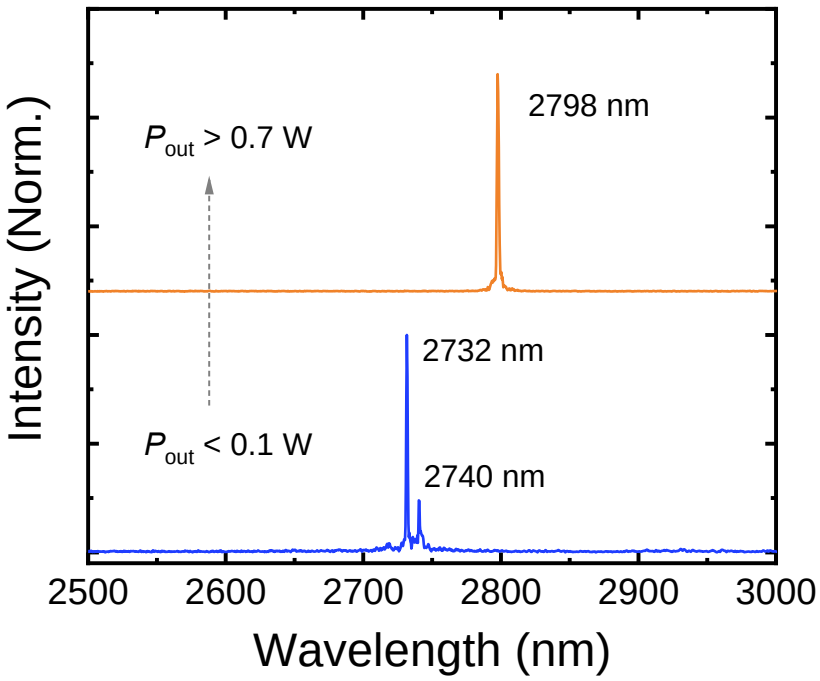

Fig. 2-7. Laser spectra of the cryogenically cooled Er:YAP laser.

We then characterized the laser spectrum using a Fourier transform optical spectrum analyzer (771B-MIR, Bristol Instruments). Figure 2-7 shows the measured spectra of the Er:YAP laser with T = 2.5% at 77 K at different output powers. The laser spectrum exhibited two peaks at 2723 nm and 2740 nm when the output power was less than 0.1 W, and shifted to 2798 nm with a linewidth of approximately 1.5 nm when the output power was higher than 0.7 W. This red shift in laser wavelength can be explained by the reabsorption effect induced by the population accumulation in the excited state $^4I_{13/2}$ [2-19].

A more intuitive explanation is illustrated in Fig. 2-8. The energy levels related to 3-μm laser transition in Er ions split into several sublevels due to the influence of the YAP matrix crystal field, including six sublevels in the upper laser level $^4I_{11/2}$ and seven sublevels in the lower laser level $^4I_{13/2}$. The Er ions absorbing 976-nm laser energy will transit from the ground state to the upper laser level and occupy each sublevel according to the Boltzmann distribution. At a low pump power, as the number of accumulated ions on the $^4I_{13/2}$ level is low, the laser transition occurs from the $^4I_{11/2}$ level to a relatively lower sublevel of the $^4I_{13/2}$ level, thus radiating high-energy photons (shorter wavelength). As the pump power and laser power increase, the number of ions on the $^4I_{13/2}$ level accumulates gradually owing to its long energy-level lifetime, driving the Er ions transit from the upper laser level to a relatively higher sublevel in the $^4I_{13/2}$ level and thus radiating low-energy photons (longer wavelength). This "driving force" is actually the laser gain of the Er:YAP crystal, which can be described by $g=\sigma\Delta n=\sigma(n_2-n_1)$, where σ represents the gain cross-section, and Δn represents the inverted population. Due to the mode competition in the resonator, the laser emission wavelength tends to the laser transition with the highest gain.

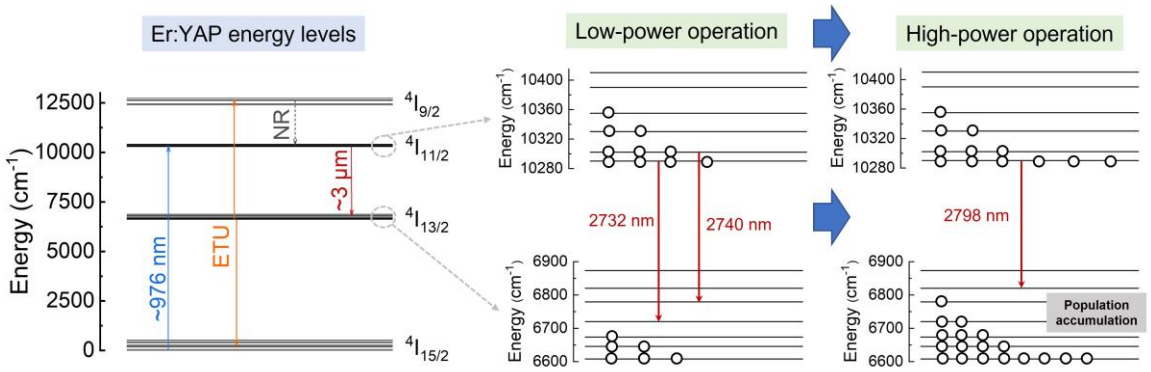

Fig. 2-8. Illustration of the red shift in lasing wavelength.

In addition, it is worth noting that at watt-level output power, the cryogenic Er:YAP laser emitted at 2798 nm while the room-temperature Er:YAP laser emitted at a much longer wavelength, i.e., 2920 nm [2-6]. This can also be explained by the lower reabsorption loss owing to the decreased lifetime of the $^4I_{13/2}$ multiplet (see Fig. 2-5), as well as the change in the Boltzmann distribution of the Stark levels at low temperatures. We can still use an energy-level diagram similar to Fig. 2-8 to explain the intrinsic

mechanism. At low temperatures, due to the reduced lifetime of the lower laser level $^4I_{13/2}$, the number of Er ions located at this level is low, such that the laser transition occurs between the upper laser level and a relatively lower sublevel in the $^4I_{13/2}$ level, thus emitting short-wavelength photons. In contrast, at a higher cooling temperature, the Er ions accumulated at the lower laser level will increase due to the increased energy-level lifetime, thus driving the laser to emit at a longer wavelength.

It should be noted that the metastable lower laser level of Er ions enables temperature tuning and power tuning of the 3-μm laser. Moreover, the strong crystal field of the YAP matrix makes the Er laser emit a narrow spectral linewidth. This power-scalable, wavelength-tunable, and narrow-linewidth characteristic of the Er:YAP laser allows it to match the lasing wavelength to a specific absorption peak of water isotopes at ~3 μm, thereby enabling high-precision water isotope detection.

2.3.3 Cavity Loss Analysis

Although the present experiment has demonstrated that cryogenic cooling can effectively improve the output power and efficiency of the Er:YAP laser, the 20% average slope efficiency is still lower than our previous results obtained at room temperature without cryostat [2-6]. This degradation in efficiency may be attributed to the increased cavity length due to the insertion of a cryostat in the cavity, which resulted in poor mode matching between the pump mode and cavity mode. However, considering that both experiments used a plane-plane cavity design, which relies on the thermal lensing effect in the crystal to achieve a stable laser resonator, the increase in cavity length would not significantly affect the mode-matching efficiency at low pump powers. Therefore, we primarily attribute the reduction in slope efficiency to the increase in passive loss of the cryogenically cooled Er:YAP laser cavity.

To analyze the source of the increased cavity loss, we calculated the passive loss of the Er:YAP resonator using the Caird analysis [2-20]. The Caird method is widely used to evaluate the passive cavity loss of a four-level laser system. An introduction to this method can be found in many laser-related reference books. Here we only present the core equation with its calculation results. The passive loss of a laser resonator can be calculated according

to:

$$\frac{1}{\eta}=\frac{1}{\eta_o}\left(1+\frac{L}{T}\right) \tag{2-1}$$

where η is the laser slope efficiency, η_o is a factor related to the limiting slope efficiency, L represents the passive loss, and T represents the output coupling transmission. Based on the output parameters (η and T) shown in Fig. 2-6, the passive loss of the cryogenically cooled Er:YAP laser was fitted to be approximately 3.5% (see blue curve in Fig. 2-9). However, the passive loss was only 0.4% (see red curve in Fig. 2-9) for our previously proposed room-temperature Er:YAP laser without cryostat [2-6].

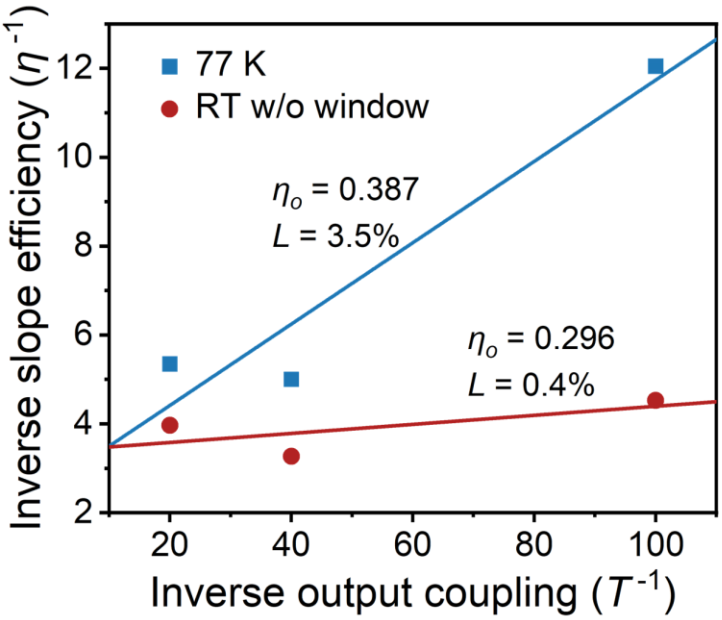

Fig. 2-9. Passive loss analysis of the Er:YAP lasers using the Caird method [2-20].

Possible reasons for the surge in cavity loss could be the insertion of a cryostat window, atmospheric vapor absorption, and thermal degradation, etc. A detailed analysis of each cause is as follows:

(1). Reflection loss of the cryostat window

The optics inserted in the cavity could cause reflection of the laser at its optical interfaces, thus introducing additional reflection loss in the resonator. However, in our experiment, we used an antireflection-coated sapphire plate as the cryostat window, the reflectivity of which was confirmed to be less than 0.3%. Therefore, such a high internal

loss (L=3.5%) was not mainly caused by the insertion of the cryostat window.

(2). Atmospheric vapor absorption

As the 3-μm band corresponds to the strongest absorption band of water molecules, the atmospheric water vapor can absorb the laser oscillating in the resonator, thus reducing the intracavity laser intensity. This loss can be regarded as an absorption loss. Therefore, the cavity length of a 3-μm solid-state laser is generally made as short as possible to minimize the vapor absorption loss. Although the cavity length of the present cryogenic Er:YAP laser was increased when compared with our previous arrangement [2-6], the length exposed to air was still very short (~5 mm), such that the increase in cavity loss may not be introduced by vapor absorption.

(3). Thermal degradation

Poor thermal management of the laser crystal may lead to severe thermal lensing effects at high-power operation, resulting in decreased mode-matching efficiency and hence lower laser efficiency, called thermal degradation. In this experiment, however, cryogenic cooling is supposed to achieve better thermal management than at room temperature. Additionally, the laser slope efficiency of the cryogenic Er:YAP laser is still lower than that obtained at room temperature even at low pump power levels. Therefore, thermal effects should not be the cause of the reduction in laser efficiency.

(4). Depolarization loss introduced by the sapphire substrate

Due to the optical anisotropy of YAP matrix, the Er:YAP can directly generate polarized laser oscillating in the resonator. Sapphire is also an optically anisotropic material and shows birefringent properties. As the sapphire window we used was cut randomly instead of along its c-axis, the laser passing through the window would be created a phase difference between its two orthogonal polarization components and thus become partially depolarized. When this depolarized laser passes through the Er:YAP for amplification, it will experience less gain because of the reduction of the polarization component that corresponds to the gain peak. As the laser makes multiple roundtrips within the cavity, it will experience this depolarization loss several times, resulting in a significant reduction in the attainable laser gain. Therefore, we attribute the large passive loss of the cryogenic Er:YAP laser primarily to the depolarization loss introduced by the sapphire window, which eventually leads to decreased laser efficiency and output power.

2.4 Conclusions and Outlook

In conclusion, the study in this chapter explores the feasibility of using cryogenic cooling technique to improve the power and efficiency of 3-μm Er-doped lasers. We investigated the spectroscopic properties and laser performance of a highly doped Er:YAP crystal at cryogenic temperatures. The spectroscopic studies demonstrated that as the cooling temperature decreased, the fluorescence lifetime of the upper laser level increased while the lifetime of the lower laser level decreased, suggesting that low temperatures are beneficial for 3-μm laser generation. In the laser experiment, a maximum output power of 1.2 W without thermal degradation was achieved at 2798 nm, which is the first watt-level Er:YAP laser that operates at cryogenic temperatures. The laser slope efficiency was 20%, which was 1.4 times higher compared to room-temperature operation with a same experimental arrangement, proving that a low cooling temperature can improve the efficiency of the 3-μm laser. The cavity loss analysis shows that the power and efficiency limits are primarily due to the additional depolarization loss introduced by the intracavity window, which was based on an optically anisotropic sapphire substrate. In future studies, further improvements in the laser performance can be realized with an appropriately-designed AR window and a longer crystal to absorb a greater fraction of the incident pump power.

More importantly, we demonstrated that the Er:YAP laser can emit a narrow spectral linewidth (< 2 nm) and can be wavelength-tuned by controlling the cooling temperature and laser power. The possibility for further power scaling and the ability to achieve narrow-linewidth, spectrally controllable laser output indicate that our proposed Er:YAP laser can meet the requirements of high-precision spectroscopy applications, which could be an ideal light source for water isotope detection.

References (Chapter II)

[2-1]. F. J. Hernandez, J. T. Brice, C. M. Leavitt, T. Liang, P. L. Raston, G. A. Pino, and G. E. Douberly, "Mid-infrared signatures of hydroxyl containing water clusters: Infrared laser Stark spectroscopy of OH–H_2O and OH$(D_2O)_n$ (n = 1-3)," The Journal of Chemical Physics, **143**(16), 164304 (2015).

[2-2]. H. Kawase and R. Yasuhara, "2.92 μm high-efficiency continuous-wave laser operation of diode-pumped Er:YAP crystal at room temperature," Optics Express, **27**(9), 12213–12220 (2019).

[2-3]. T. Sanamyan, M. Kanskar, Y. Xiao, D. Kedlaya, and M. Dubinskii, "High power diode-pumped 2.7-μm Er^{3+}:Y_2O_3 laser with nearly quantum defect-limited efficiency," Optics Express, **19**(105), A1082–A1087 (2011).

[2-4]. Y. O. Aydin, V. Fortin, R. Vallée, and M. Bernier, "Towards power scaling of 2.8 μm fiber lasers," Optics Letters, **43**(18), 4542–4545 (2018).

[2-5]. S. Tokita, M. Murakami, and S. Shimizu, "High Power 3 μm Erbium Fiber Lasers," in Advanced Solid State Lasers, OSA Technical Digest (online) (Optical Society of America, 2014), AM3A.4.

[2-6]. W. Yao, H. Uehara, H. Kawase, H. Chen, and R. Yasuhara, "Highly efficient Er:YAP laser with 6.9 W of output power at 2920 nm," Optics Express **28**(13), 19000–19007 (2020).

[2-7]. M. Ding, X. Li, F. Wang, D. Shen, J. Wang, D. Tang and H. Zhu, "Power scaling of diode-pumped Er:Y_2O_3 ceramic laser at 2.7 μm," Applied Physics Express, **15**(6) 062004 (2022).

[2-8]. W. Yao, H. Uehara, S. Tokita, H. Chen, D. Konishi, M. Murakami, and R. Yasuhara, "LD-pumped 2.8 μm Er:Lu_2O_3 ceramic laser with 6.7 W output power and >30% slope efficiency," Applied Physics Express, **14**(1), 012001 (2020).

[2-9]. J. I. Mackenzie, N. Ter-Gabrielyan, and Y.-F. Chen, "Frontiers in laser science—cryogenically cooled lasers: editorial," Applied Physics B, **127**, 49 (2021).

[2-10]. T. Sanamyan, J. Simmons, and M. Dubinskii, "Efficient cryo-cooled 2.7-μm Er^{3+}:Y_2O_3 ceramic laser with direct diode pumping of the upper laser level," Laser Physics Letters, **7**(8), 569–572 (2010).

[2-11]. Z. D. Fleischman and T. Sanamyan, "Spectroscopic analysis of Er^{3+}:Y_2O_3 relevant to 2.7μm mid-IR laser," Optics Materials Express, **6**(10), 3109–3118 (2016).

[2-12]. R. Svejkar, J. Sulc, M. Nemec, H. Jelínkova, K. Nejezchleb, and M. Cech, "Temperature influence on spectroscopic properties and 2.7-μm lasing of Er:YAP crystal," Proc. SPIE **10511**, 1051121 (2018).

[2-13]. C. Quan, D. Sun, J. Luo, H. Zhang, Z. Fang, X. Zhao, L. Hu, M. Cheng, Q. Zhang, and S. Yin, "2.7 μm dual-wavelength laser performance of LD end-pumped Er:YAP crystal," Optics Express, **26**(22), 28421–28428 (2018).

[2-14]. C. Quan, D. Sun, H. Zhang, J. Luo, L. Hu, Z. Han, Y. Qiao, K. Dong, Y. Chen, and M. Cheng, "Growth, spectroscopy and high-power laser operation of Er:YAP crystal with different Er^{3+} concentrations," Journal of Luminescence, **251**, 119122 (2022).

[2-15]. https://www.fluortools.com/software/decayfit-fluorescence-decay-analysis/decayfit-documentation-pages/fluorescence-intensity-decay-models

[2-16]. H. Uehara, S. Tokita, J. Kawanaka, D. Konishi, M. Murakami, S. Shimizu, and R. Yasuhara, "Optimization of laser emission at 2.8 μm by Er:Lu_2O_3 ceramics" Optics Express, **26**(3), 3497–3507 (2018).

[2-17]. V. A. Antonov, P. A. Arsenev, K. E. Kienert, and A. V. Potemkin, "Spectral properties of rare-earth ions in YAlO3 crystals," Physica Status Solidi (a), **19**(1), 289–299 (1973).

[2-18]. T. Jensen, A. Diening, G. Huber, and B. H. T. Chai, "Investigation of diode-pumped 2.8-μm Er:$LiYF_4$ lasers with various doping levels," Optics Letters, **21**(8), 585–587 (1996).

[2-19]. L. Wang, H. Huang, D. Shen, J. Zhang, H. Chen, Y. Wang, X. Liu, and D. Tang, "Room temperature continuous-wave laser performance of LD pumped Er:Lu_2O_3 and Er:Y_2O_3 ceramic at 2.7 μm," Optics Express, **22**(16), 19495–19503 (2014).

[2-20]. J. A. Caird, S. A. Payne, P. Staber, A. Ramponi, L. Chase, and W. F. Krupke, "Quantum electronic properties of the $Na_3Ga_2Li_3F_{12}$:Cr^{3+} laser" IEEE Journal of Quantum Electronics, **24**, 1077–1099 (1988).

III. 4-μm Fe:ZnSe Laser Oscillator End Pumped by an Er:YAP Laser

3.1 Research Status and Problem Statement

Lasers operating in the 4-μm band, especially the 4.4 μm, are ideally suited for measuring HTO because the absorption peaks of HTO are exactly located around the 4-μm band. Currently, there are three common methods to generate 4-μm lasers:

(1). Quantum cascade laser

Quantum cascade laser (QCL) is a type of semiconductor laser that operates based on a cascade of intersubband transitions within a repeated series of quantum wells [3-1]. Similar to other semiconductor lasers, QCL features a very compact structure that allows for integration into portable or handheld instruments, as well as deployment in space-constrained environments. Moreover, QCLs can achieve high electrical-to-optical conversion efficiency compared to other mid-infrared laser generation methods. However, the output power of QCLs is relatively low due to their intrinsic small active area [3-2]. Currently, commercially available products can only provide tens to hundreds of milliwatts of laser power.

(2). Nonlinear frequency conversion

Lasers based on nonlinear frequency conversion, such as frequency doubling [3-3], difference frequency generation [3-4], and optical parametric oscillation [3-5], are another effective means of generating 4-μm lasers. The nonlinear lasers are known for their powerful wavelength-tuning capabilities. By combining different nonlinear frequency conversion processes with different input lasers and nonlinear optical materials, it is possible to access the entire mid-infrared spectral region, including which is not easily attainable using direct laser emission [3-6]. However, a nonlinear device typically requires a multi-stage design, resulting in a complex architecture and a low wall-plug efficiency. Additionally, nonlinear devices often require stringent alignment of the input laser to achieve precise phase matching, which is critical in determining the output performance and laser spectrum. Therefore, the construction of a nonlinear frequency conversion device is quite tricky.

(3). Iron-doped II-VI chalcogenide

A more efficient approach to generating 4-μm lasers is based on the direct laser emission from iron-doped II-VI chalcogenides, of which the most commonly used material is iron-doped zinc selenide (Fe:ZnSe) [3-7]. Due to the broad absorption and emission bands as well as large cross-section values, Fe:ZnSe is capable of producing tunable lasers and ultrafast lasers with both high power and high efficiency. Additionally, Fe:ZnSe can be directly pumped by a 3-μm Er-doped laser and lase at ~4 μm, thus enabling a more compact structure and higher quantum conversion efficiency.

In contrast, the 4-μm laser based on the Fe:ZnSe is the most promising approach to combine high output power with high optical efficiency. Therefore, this study focuses on exploring new techniques to improve the power and efficiency of 4-μm Fe:ZnSe lasers.

To date, almost all known modes of laser operation, including free-running [3-8], gain-switching [3-9], continuous-wave (CW) [3-10], Q-switching [3-11], and mode-locking [3-12] with Fe:ZnSe single crystals or polycrystals have been studied and reported. However, despite the impressive laser performance presented by Fe:ZnSe, the development of the CW Fe:ZnSe lasers has remained limited, primarily due to the lack of reliable 3-μm CW pump sources with high output power and good beam quality. Thus far, only a few high-performance 3-μm lasers have been developed for pumping the Fe:ZnSe, which are primarily based on chromium-doped chalcogenides (Cr:CdSe, Cr:ZnSe) [3-10] and on erbium-doped crystals or fibers (Er:YAG, Er:Y_2O_3, Er:ZBLAN) [3-13][3-14]. Figure 3-1 summarizes the applicable pump sources for Fe:ZnSe with their laser wavelengths and output powers; the absorption spectrum of Fe:ZnSe is also shown to aid in the evaluation of pump absorption. The highest output power reported for the CW Fe:ZnSe lasers was achieved by employing a Cr:ZnSe laser as the pump source, which produced 9.2 W of output power with an optical-to-optical efficiency of 40% [3-15]. Recently, the Er:ZBLAN fiber laser has emerged as a promising pump source for the Fe:ZnSe laser, which presented 2.1 W of Fe:ZnSe output power with 59% of slope efficiency [3-16]. However, the Cr:ZnSe laser and the Er:ZBLAN fiber laser remain limited in operational durability because they both suffer from relatively weak mechanical strength and strong thermal effects during lasing process, thus requiring significant thermal management and elaborate design to

prevent damage to the gain elements [3-17][3-18]. In contrast, our proposed Er:YAP laser, which was able to generate nearly 7 W of output power from a simple and compact plane-plane cavity design [3-19], could be another promising pump source for Fe:ZnSe. The Er:YAP crystal possesses a lower thermo-optic coefficient than the Cr:ZnSe crystal and a more robust mechanical strength than the Er:ZBLAN fiber, indicating the low requirements for thermal management. Additionally, the room-temperature Er:YAP laser emits at 2920 nm, enabling a higher quantum efficiency and a higher pump absorption for pumping the Fe:ZnSe laser when compared to the Er:ZBLAN laser (typically emitting at 2800 nm [3-16]). The high performance, robustness, and low cost of the Er:YAP laser indicate its considerable potential for the pumping of the Fe:ZnSe laser.

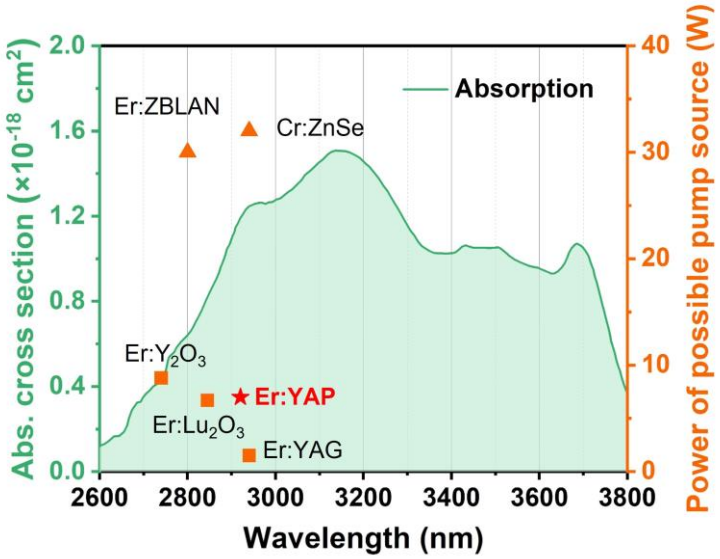

Fig. 3-1. 3-μm laser sources that can be used to pump Fe:ZnSe lasers.

In this study, we present the novel development of a 4-μm Fe:ZnSe laser oscillator, which is end pumped by our inhouse-built Er:YAP laser operating at 2920 nm. The detailed lasing characteristics, such as output power, spectra, and beam quality, are studied for both the Er:YAP pump source and the Fe:ZnSe laser. Further, we present a rate equation model to evaluate the laser performance of the CW Fe:ZnSe laser. The theoretical calculations are comprehensively compared with our experimental results to determine the validity of the proposed model. In addition, thermal analysis of the cryogenically cooled Fe:ZnSe laser is conducted using finite element analysis to predict the power scaling behavior of the Fe:ZnSe laser.

3.2 Laser Performance of Fe:ZnSe Pumped by Er:YAP Laser

3.2.1 Experimental Setup

We constructed a CW Er:YAP laser operating at room temperature to pump the Fe:ZnSe, which was based on a compact plane-plane cavity design, as shown in Fig. 3-2(a). A fiber-coupled laser diode with a stabilized central wavelength of 976.2 nm and a linewidth of 0.1 nm was used to pump the Er:YAP crystal. The reason for using a wavelength-stabilized laser diode was to mitigate the possible excited-state absorption ($^4I_{11/2} \rightarrow {}^4F_{7/2}$) of the Er:YAP crystal [3-20] and to ensure steady power stability during laser operation. The coupling fiber had a core diameter of 105 μm and a numerical aperture of 0.22. The laser output from the fiber pigtail was collimated by a 20 mm focal-length aspheric lens and was then focused into the Er:YAP crystal with a beam waist radius of ~260 μm by a plano-convex lens of 100-mm focal length. Compared to the system in [3-19], a relatively larger pump size was selected to mitigate the thermal lensing effects and thus achieve a higher beam quality at high power levels.

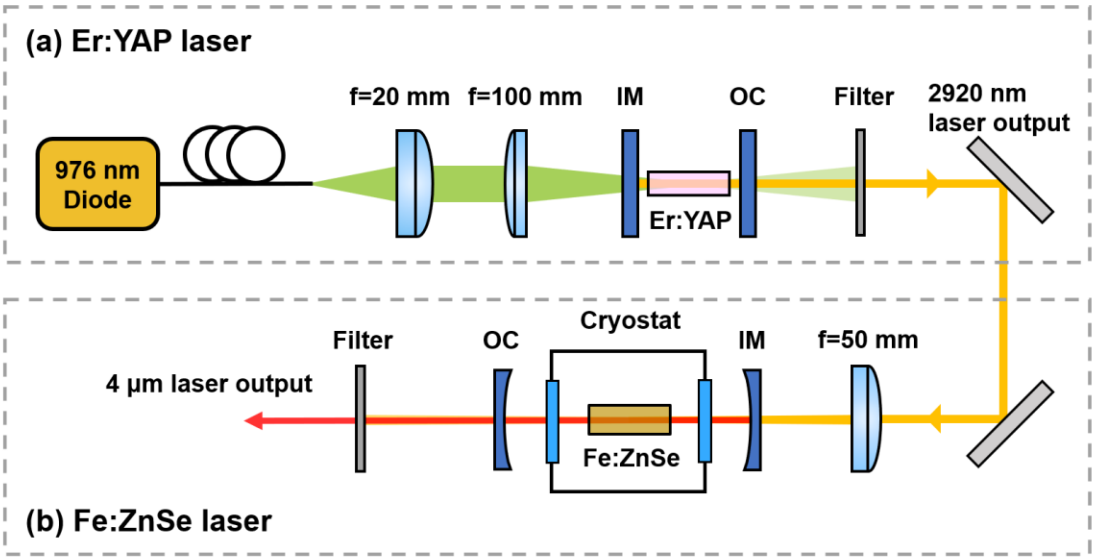

Fig. 3-2. Schematic of the (a) Er:YAP pump source and (b) Fe:ZnSe oscillator.

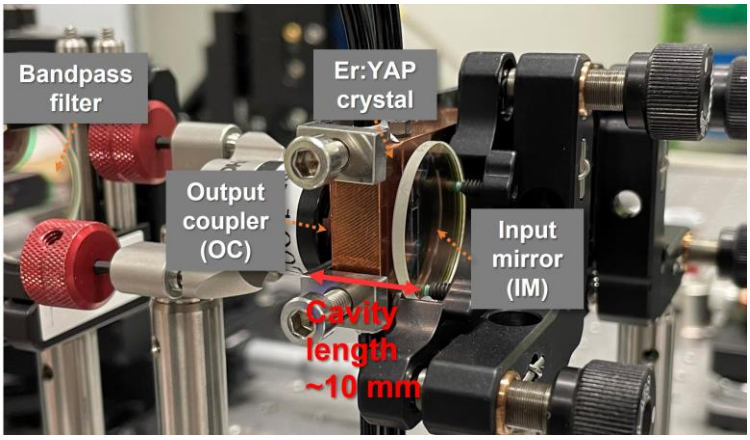

Fig. 3-3. Photograph of the Er:YAP laser resonator.

The Er:YAP resonator, as shown in Fig. 3-3, was based on a compact plane-plane cavity configuration, comprising a plane input mirror coated for high transmission (T>97%) at the pump wavelength of ~976 nm and high reflection (R>99%) at the lasing wavelength of ~2.9 μm, an uncoated b-cut Er:YAP crystal (space group: *Pbnm*), and a plane output coupler with a transmission of 2.5% at ~2.9 μm. The Er:YAP crystal had a doping concentration of 5 at.% and was cut in a slab shape with a cross-sectional area of 2 mm×5 mm and a length of 8 mm. It was wrapped in a 50-μm-thick indium foil and then mounted in a well-designed copper heat sink, which was water-cooled to 16 °C. The laser cavity was built as short as possible to minimize intracavity loss (primarily vapor absorption) and to ensure good stability during high-power operation. A bandpass filter operating at 2.5–3.1 μm was placed behind the cavity to separate the laser output from the residual pump light.

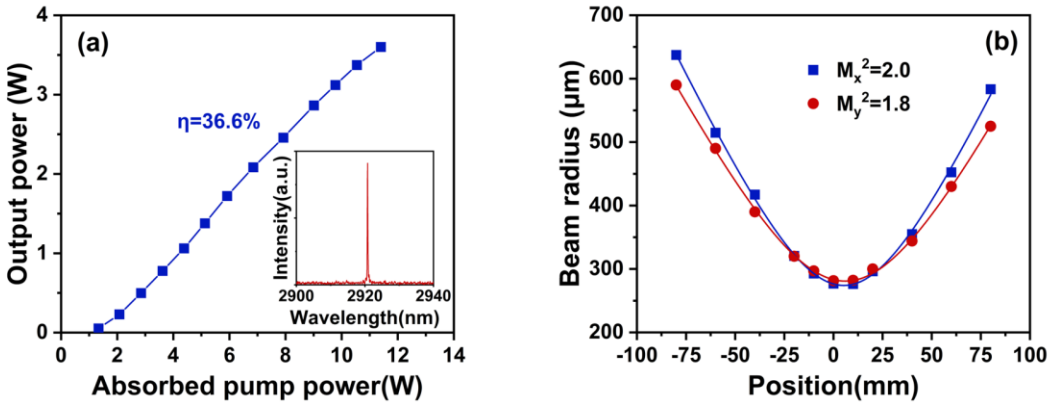

Fig. 3-4. Output characteristics of the Er:YAP pump source. (a) Output power versus absorbed pump power. (b) Laser beam quality.

Figure 3-4 shows the output characteristics of our self-constructed Er:YAP pump source. The Er:YAP crystal absorbed approximately 71% of the incident pump power. A maximum laser output power of 3.6 W was obtained at the absorbed pump power of 11.4 W, corresponding to an average slope efficiency of 36.6%, as shown in Fig. 3-4(a). Note that the achieved slope efficiency (36.6%) is higher than the Stokes limit (λ_{pump} / λ_{laser} = 33.4%) of the Er:YAP laser. This can be explained by the energy transfer up-conversion process (see Fig. 2-8: $^4I_{13/2} + {}^4I_{13/2} \rightarrow {}^4I_{9/2} + {}^4I_{15/2}$) in the Er laser systems [3-21], which could recycle the population of the lower laser level to the upper laser level and thus increase the quantum efficiency. The lasing wavelength of Er:YAP was centered at 2920.8 nm with a spectral linewidth of 0.2 nm (see the inset of Fig. 3-4(a)). Compared to the lasing wavelengths of ~2.7 μm reported in [3-22], our proposed Er:YAP laser emitted at 2920 nm at the output power of over 100 mW, which was attributed to the population accumulation of the lower laser level ($^4I_{13/2}$) at high pump intensities as well as the specific coating property of the output coupler. The power fluctuation at the highest output power was less than 3%. It is worth noting that a higher output power can be achieved with further increase in the pump power [3-19], but at the risk of higher power instability, degradation in beam quality, and even crystal damage. Therefore, the output power of the Er:YAP laser was not further increased in the subsequent Fe:ZnSe laser experiment. The laser beam quality at the maximum output power was measured using the 90/10 knife-edge method. The beam quality factors were M_x^2=2.0 and M_y^2=1.8 for the horizontal and vertical directions, respectively, as shown in Fig. 3-4(b).

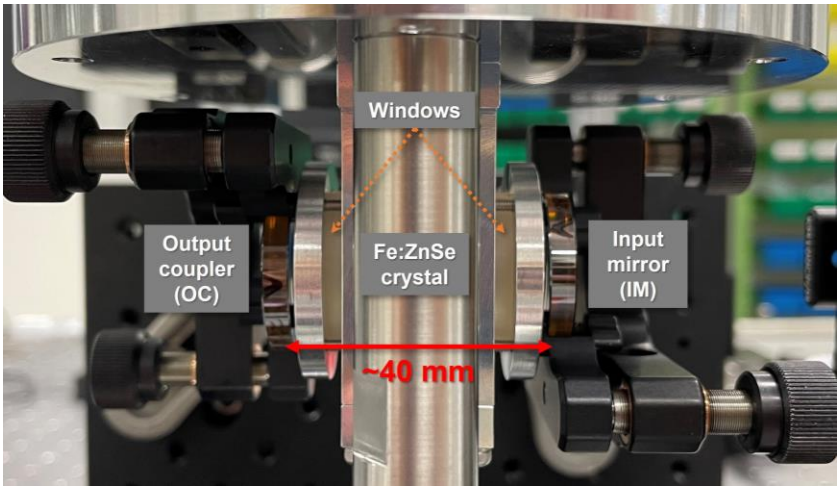

Fig. 3-5. Photograph of the Fe:ZnSe laser resonator.

For the 4-μm Fe:ZnSe laser, we constructed a compact concave-concave cavity (see Fig. 3-5) consisting of a 100 mm radius-of-curvature input mirror coated for high transmission (T>95%) at ~2.9 μm and high reflection (R>99%) at 3.8–5.1 μm, and a 100 mm radius-of-curvature output coupler. Three output coupling transmissions (T=2.5%, 10%, and 20%) were used to optimize the laser performance. The gain medium was an Fe:ZnSe in single-crystal form, which was grown from a vapor phase using the seeded physical vapor transport technique [3-23]. The crystal had a cross-sectional area of 2 mm×4 mm and a length of 8 mm; both the end facets were anti-reflection coated at the pump and lasing wavelengths. The Fe-ion doping concentration was determined to be 2.2×10^{18} cm^{-3} (0.01 at.%) according to the small-signal absorption measured at room temperature. The Fe:ZnSe crystal was mounted in a 10 mm long cryostat and was cryogenically cooled to 77 K by liquid nitrogen. Cryogenic cooling for Fe:ZnSe is necessary because it suffers from severe thermal quenching effect, which makes the fluorescence lifetime of the upper laser level so short at room temperature that CW laser operation cannot be obtained. Two BaF_2 plates, which were anti-reflection coated at 2–5 μm, served as the cryostat windows. The vacuum chamber was evacuated to a pressure below 1.5 mTorr. The total length of the Fe:ZnSe cavity was approximately 40 mm after taking into account the space occupied by the cryostat; thus, the TEM_{00} mode radius calculated from the ABCD matrix analysis was approximately 210 μm. A 50-mm focal-length CaF_2 lens was used to focus the output of the Er:YAP pump laser into the center of the Fe:ZnSe crystal. The pump coupling efficiency after the Er:YAP laser passing through the 3-μm bandpass filter, CaF_2 lens, input mirror, and BaF_2 window was measured to be 72%, resulting in a maximum pump power of 2.5 W incident upon the Fe:ZnSe crystal. The pump waist radius was experimentally measured to be approximately 140 μm. This relatively small pump beam radius was deliberately chosen to achieve a high pump intensity and a high lasing efficiency. A bandpass filter operating at 3.8–4.2 μm was placed behind the Fe:ZnSe resonator to block the unabsorbed pump light to measure the 4-μm laser power accurately.

3.2.2 Laser Output Characteristics

We first examined the pump absorption of the Fe:ZnSe by measuring the unabsorbed pump power that transmitted through the crystal under non-lasing conditions. The small-signal pump absorption was determined to be approximately 85%, which was used to calculate the absorbed pump power as the ground state bleaching can be considerably mitigated under the lasing conditions. Figure 3-6 shows the laser output characteristics of the Fe:ZnSe crystal pumped by Er:YAP laser. Laser performance was examined using three output couplers, as shown in Fig. 3-6(a). The threshold pump powers for the output couplers with T=2.5%, T=10%, and T=20% were 88 mW, 104 mW, and 153 mW, respectively, and the corresponding slope efficiencies with respect to the absorbed pump power were 10.8%, 30.8%, and 46.1%, respectively. Thus, the internal loss coefficient was calculated to be 0.13 cm^{-1} according to the Carid analysis [3-24]. This internal loss was primarily attributed to the imperfect anti-reflection coating of the two BaF_2 cryostat windows and the Fe:ZnSe crystal. A larger output coupling transmission (T=20%) was preferred for higher lasing efficiency and output power owing to the high gain of the Fe:ZnSe crystal. At the maximum absorbed pump power of 2.1 W, the Fe:ZnSe laser produced a maximum output power of 1 W, as shown in Fig. 3-6(b). The average slope efficiency and the optical-to-optical efficiency with respect to the absorbed Er:YAP laser power were 48% and 40%, respectively. More importantly, one should notice that the overall optical conversion efficiency, calculated from the initial 976-nm laser diode to the final 4-μm Fe:ZnSe laser, was 8.8%, which represents the highest conversion efficiency for the CW Fe:ZnSe laser reported thus far.

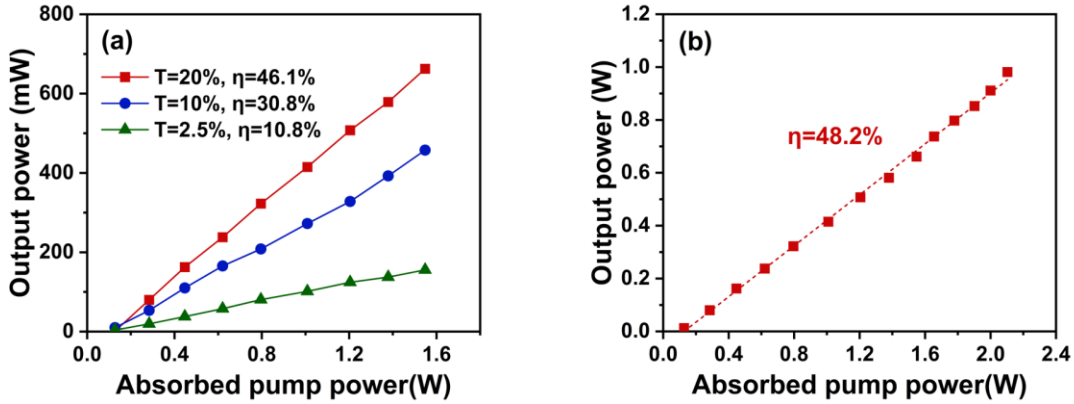

Fig. 3-6. Output characteristics of the Fe:ZnSe laser. (a) Output power versus absorbed pump power for three output coupling transmissions. (b) Power scaling performance.

Thereafter, we characterized the emission spectra of the Fe:ZnSe laser using a Fourier transform optical spectrum analyzer (771B-MIR, Bristol) with a spectral resolution of 0.1 nm. Figure 3-7(a) shows the typical lasing spectra recorded at the same power level, i.e., ~200 mW, for using output couplers with T=2.5%, T=10%, and T=20%. It can be seen that the emission spectra all exhibited a broadband and multi-peak structure. With the increase in the output coupling transmission, an obvious blue shift in the central lasing wavelength was observed, which can be explained by decreased reabsorption loss induced by a high population inversion ratio. Figure 3-7(b) shows the variations in the lasing central wavelength and wavelength span with the output power for using T=20%. With increased output power, the central wavelength shifted from 4012 nm to 4057 nm, and the lasing wavelength span increased from 35 nm to 115 nm. The changes in the central wavelength were primarily attributed to the localized temperature rise of the Fe:ZnSe crystal inside the pumping region, causing a redistribution of population among the energy levels of the Fe ions and the subsequent increase of reabsorption loss at shorter wavelengths. Additionally, it has been reported that the temperature rise would also result in the broadening of the emission spectrum of Fe:ZnSe [3-25], which is one of the reasons for the increase in the wavelength-spanning range. These spectral properties suggest the Fe:ZnSe laser can be coarsely tuned in laser wavelength by adjusting the cooling temperature and laser power. However, this broad-spectrum property makes it rather difficult to use the laser directly emitted from the Fe:ZnSe oscillator for high-precision spectroscopy applications.

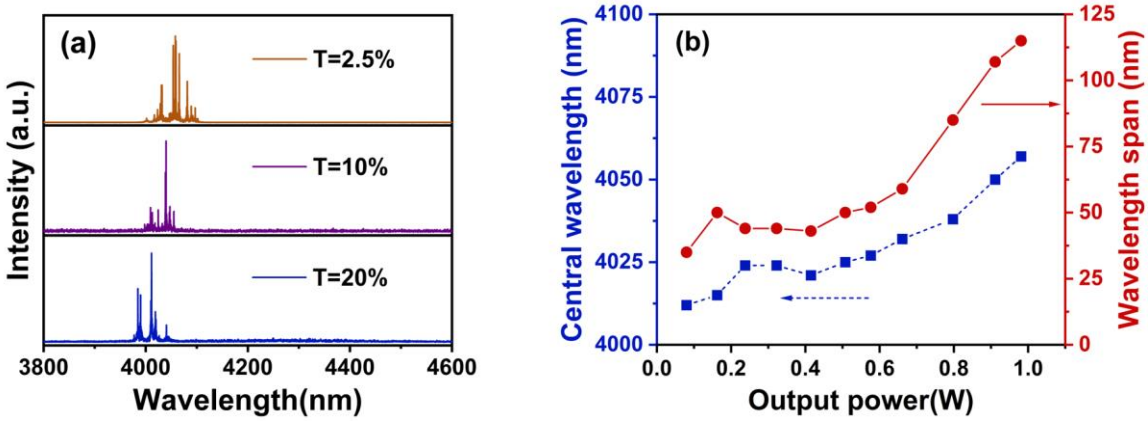

Fig. 3-7. Spectral characteristics of the Fe:ZnSe laser. (a) Typical laser spectra for using output couplers of T=2.5%, 10%, 20%. (b) Dependence of lasing central wavelength and wavelength span on the laser output power.

The laser beam quality at the maximum output power was measured by using the 90/10 knife-edge method. A CaF_2 lens with a focal length of 100 mm was used to focus the laser output to measure the beam radii along the propagation path. The beam quality factor M^2 was then hyperbolically fitted to be M_x^2=1.5 and M_y^2=1.6 along the horizontal and vertical directions, respectively, as shown in Fig. 3-8. The two-dimensional beam profile was recorded using an infrared camera (see the inset of Fig. 3-8). It can be seen that the profile shows a typical Gaussian energy distribution, verifying high-beam-quality laser operation over the entire pump power range.

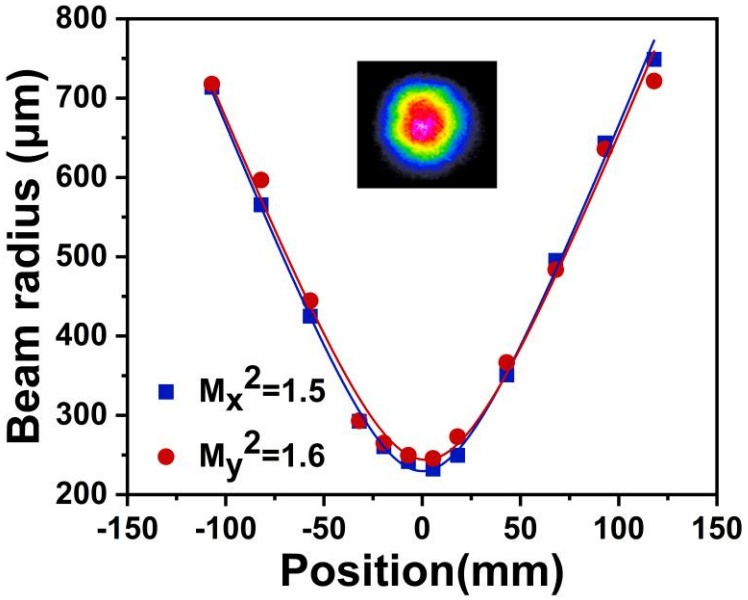

Fig. 3-8. Beam quality of the Fe:ZnSe laser measured at the maximum output power. Inset: two-dimensional beam profile.

3.3 Theoretical Modeling of Fe:ZnSe laser

3.3.1 Rate Equation Model

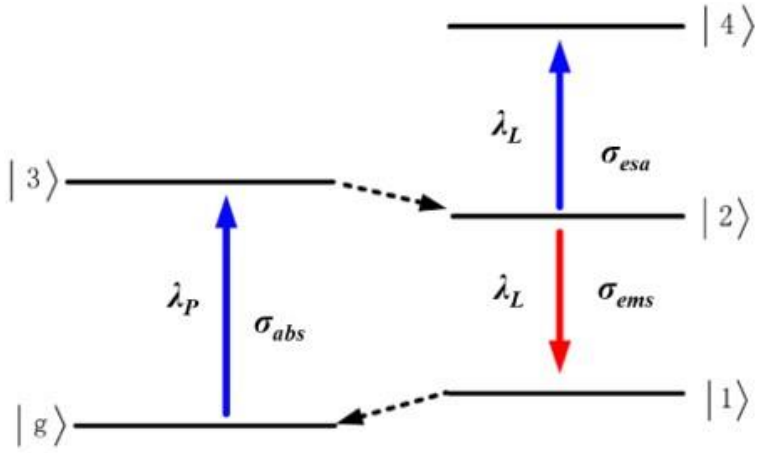

Fig. 3-9. Energy level diagram of the Fe:ZnSe.

Currently, the output power of the 4-μm Fe:ZnSe laser obtained experimentally is limited to the order of several watts, which is mainly limited by the available power of the

3-μm pump light. However, with the rapid development of the 3-μm laser, the output power of Fe:ZnSe laser is also expected to be further increased to a new order of magnitude. Therefore, it is required to theoretically analyze the power scaling capability of the Fe:ZnSe laser, anticipate the possible problems in the power improvement process, and then propose countermeasures. For this purpose, we propose a rate equation model for the Fe:ZnSe laser and conduct theoretical studies on its output characteristics.

Fe:ZnSe exhibits a typical four-level structure [3-26], the energy level diagram of which is illustrated in Fig. 3-9. The Fe ions can absorb the 3-μm photon energy and transit to the third excited state |3>, then relax to the second excited state |2> (i.e., the upper laser level) via a fast nonradiative decay process. The laser transition occurs between the level |2> and the first excited state |1>, resulting in the radiation of 4-μm photons. As the energy gap between the level |1> and the ground state |g> is very small, the Fe ions at level |1> will relax rapidly to the ground state through nonradiative transition, such that the population density of the lower laser level is negligible. Therefore, Fe:ZnSe can provide a large inverted population density and hence a high laser gain. In addition, as the energy difference between the upper laser level and the fourth excited state |4> is comparable to the energy released by the 4-μm laser transition, the Fe ions at the upper laser level may absorb the energy of the 4-μm laser and then transit to the level |4>, which is a process called excited-state absorption (ESA). This process depopulates the upper laser level and consumes the laser energy, thus causing a degradation in laser performance.

At steady state, the population densities in the energy levels |1>, |3>, and |4> can be reasonably neglected owing to the strong nonradiative relaxation processes. With this approximation, there is:

$$N_T(z) = N_g(z) + N_2(z) \tag{3-1}$$

where $N_T(z)$ represents the total doping concentration of the Fe ions; $N_g(z)$ and $N_2(z)$ are the population densities of the ground level and upper laser level, respectively.

Taking into account all the aforementioned energy transition processes, a rate equation to describe the population evolution of the upper laser level can be written as:

$$\frac{dN_2(z)}{dt} = \frac{\sigma_{abs}\lambda_P I_P(z)}{hc} N_g(z) - \frac{\sigma_{ems}\lambda_L I_L(z)}{hc} N_2(z) - \frac{\sigma_{esa}\lambda_L I_L(z)}{hc} N_2(z) - \frac{N_2(z)}{\tau_f} \tag{3-2}$$

where σ_{abs} is the absorption cross-section at the pump wavelength (λ_P); σ_{ems} and σ_{esa}

represent the emission and ESA cross-sections at the lasing wavelength (λ_L); $I_P(z)$ is the pump intensity [$I_P(z) = I_P^+(z) + I_P^-(z)$]; $I_L(z)$ is the laser intensity [$I_L(z) = I_L^+(z) + I_L^-(z)$]; and, τ_f represents the fluorescence lifetime of the upper laser level.

By combining equations (3-1) and (3-2), the steady-state population in the upper laser level can be solved analytically as follows:

$$N_2(z) = N_T \frac{\frac{I_P(z)}{I_{sa}}}{1 + \frac{(1+f) I_L(z)}{I_{se}} + \frac{I_P(z)}{I_{sa}}} \tag{3-3}$$

where I_{sa} represents the saturated absorption intensity ($I_{sa} = hc/\sigma_{abs}\lambda_P\tau_f$), I_{se} is the saturated emission intensity ($I_{se} = hc/\sigma_{ems}\lambda_L\tau_f$), and f represents the normalized ESA strength at the lasing wavelength ($f = \sigma_{esa}/\sigma_{ems}$).

In an end-pumped laser resonator, the pump light is gradually attenuated along the propagation path due to the absorption by the gain medium, while the laser circulating in the cavity is progressively amplified as it passes through the gain medium. Theoretically, this is a three-dimensional problem because the pump laser typically has a Gaussian intensity distribution in the lateral direction, and the pump absorption of the gain medium is not uniform along the propagation path owing to the end-pumping structure. However, in this study we are merely interested in the power scaling behavior of the end-pumped Fe:ZnSe laser; thus, the rate equations can be simplified to a one-dimensional problem by assuming a plane-wave approximation, i.e., ignoring the lateral intensity distribution of the pump and laser beams. This approximation is reasonable because strong interactions between the pump and laser beams only occur in the paraxial areas where the modes are highly overlapped. Therefore, a mode matching factor η was introduced to quantify the degree of overlap between the pump mode and the cavity mode [$\eta = 4wP_2w_L^2 / (w_P^2 + w_L^2)^2$] [3-27], where w_P and w_L are the beam radii of the pump and cavity modes, respectively. Then the transversal variations of the pump and the cavity intensities can be neglected, and only the longitudinal variations of the intensities are considered.

In addition, it is rather difficult to quantify each source of loss in the Fe:ZnSe resonator because it is impractical to precisely obtain the cavity parameters during lasing operation. Thus, we generally use one internal loss coefficient, which combines all possible losses and is assumed to be uniform within the cavity along the laser propagation path, to evaluate

the total cavity loss. This internal loss coefficient can be measured experimentally, e.g., using the Caird method [3-24] mentioned above. Therefore, we assume that the end facets of the Fe:ZnSe crystal are butted against the cavity mirrors such that the total internal cavity loss can be lumped upon the crystal length. The equivalent model of the laser resonator after simplification is illustrated in Fig. 3-10.

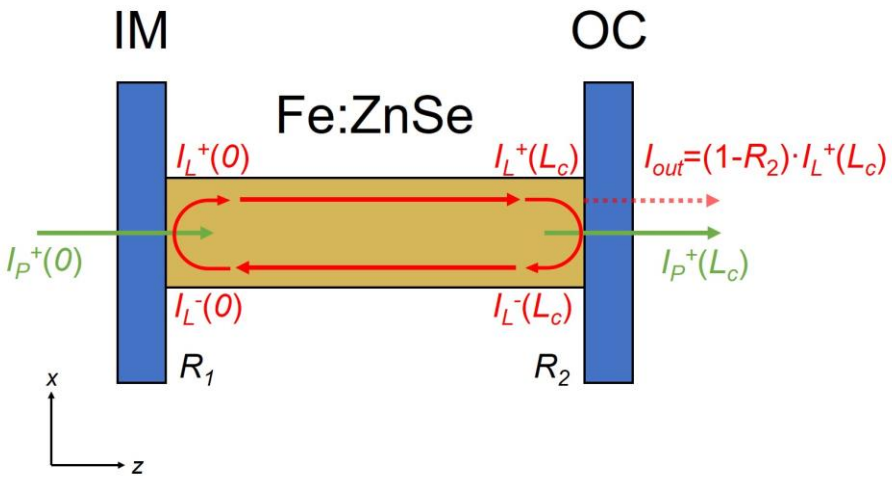

Fig. 3-10. Simplified model of pump and laser transmission in a resonator.

Considering the plane-wave approximation with the simplified resonator model, the differential equations used to describe the propagation of the pump and laser intensities can be written as:

$$\frac{dI_P^{\pm}(z)}{dz} = \mp I_P^{\pm}(z)\frac{\alpha_{P0}\left[1+\dfrac{(1+f)\eta I_L(z)}{I_{se}}\right]}{1+\dfrac{I_P(z)}{I_{sa}}+\dfrac{(1+f)\eta I_L(z)}{I_{se}}} \tag{3-4}$$

$$\frac{dI_L^{\pm}(z)}{dz} = \pm I_L^{\pm}(z)\left[\frac{g_T(1-f)\eta\dfrac{I_P(z)}{I_{sa}}}{1+\eta\dfrac{I_P(z)}{I_{sa}}+(1+f)\dfrac{I_L(z)}{I_{se}}}-\alpha_L\right] \tag{3-5}$$

where $I_P^+(z)$, $I_P^-(z)$, $I_L^+(z)$, and $I_L^-(z)$ are the forward and backward pump intensities and laser intensities, respectively; α_{P0} is the small signal absorption coefficient ($\alpha_{P0} = \sigma_{abs}N_T$); g_T is the maximum extractable small signal gain coefficient ($g_T = \sigma_{ems}N_T$); α_L is the intracavity loss coefficient excluding the output coupling loss. According to Fig. 3-10, the

boundary conditions are described by:

$$I_P^+(0)=I_P^l\ ,\ I_P^-(L_c)=I_P^r\ ,\ I_L^+(0)=R_1I_L^-(0)\ ,\ I_L^-(L_c)=R_2I_L^+(L_c) \qquad (3\text{-}6)$$

where $I_P{}^l$ and $I_P{}^r$ are the average intensities of the forward and backward pump lights, respectively; R_1 and R_2 are the reflectivities of the input mirror and the output coupler, respectively; and L_c represents the crystal length. This model is applicable to a dual-end-pumped laser configuration, but in our case we used a single-end-pumped arrangement and thus $I_P{}^r$=0. The parameters required for the calculation are based on the published spectroscopic data in conjunction with our practical experimental arrangement and are summarized in Table 3-1.

Table 3-1. The parameters for the modeling of Fe:ZnSe laser

Definition	**Symbol**	**Value/unit**
Doping concentration	N_T	2.2×10^{18} cm^{-3}
Absorption cross-section	σ_{abs}	1.2×10^{-18} cm^2 @2920 nm [3-28]
Emission cross-section	σ_{ems}	2.2×10^{-18} cm^2 @4000 nm [3-28]
Normalized ESA coefficient	f	0.17 [3-29]
Fluorescence lifetime	τ_f	57 μs at 77 K [3-7]
Pump beam radius	w_P	140 μm
Laser beam radius	w_L	210 μm
Crystal length	L_c	8 mm
Intracavity loss coefficient	α_L	0.13 cm^{-1}
Reflectivity of input mirror	R_1	99%
Reflectivity of output coupler	R_2	80%

The laser output performance can be predicted for various cavity configurations by numerically solving equations (3-4)–(3-5) with boundary conditions (3-6) and parameters in Table 1. Figure 3-11 shows a typical calculation result of the intracavity pump and laser powers for an incident pump power of 2.5 W. The pump power (blue triangles) attenuates gradually along the propagation path due to the absorption of Fe:ZnSe. The oscillations established in the resonator gradually tend to be self-consistent when the boundary conditions are satisfied. The difference between the forward (red circles) and backward (orange squares) laser powers at the position of the output coupler (z=8 mm) is the laser power coupled out of the cavity, i.e., the output power.

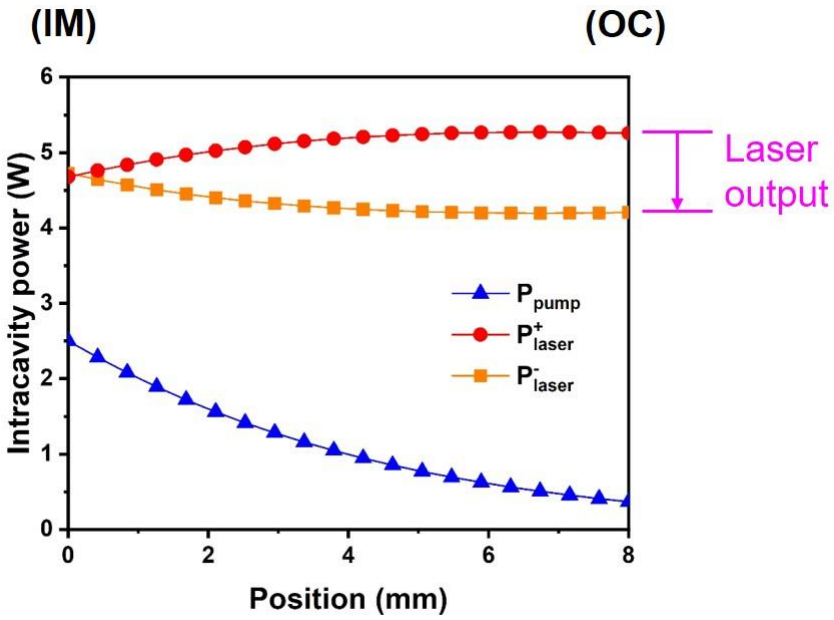

Fig. 3-11. Calculated results of the intracavity pump and laser powers for an incident pump power of 2.5 W.

Figure 3-12(a) shows the calculated output power as a function of the absorbed pump power, in which the experimental results are also shown for comparison. Note that the theoretical results agree well with our experimental results, proving the validity of our simplified rate equation model in estimating the output performance of the Fe:ZnSe laser. The minor difference between the theoretical and experimental results is partially attributed to the error in the calculation of the internal cavity loss owing to the lack of multiple output coupler samples, and also because the thermal effects inside the crystal are neglected, which will inevitably degrade the laser performance. In addition, the optical-to-optical efficiency was calculated as a function of the output transmission to determine the optimum transmission value. The results, shown in Fig. 3-12(b), indicate that the optimum output coupling transmission is approximately 60%, with an optical-to-optical efficiency of 60% and an output power of 1.5 W for 2.5 W of incident pump power. Moreover, we can learn from the theoretical calculations that further optimization of the output power can also be achieved by increasing the crystal length to obtain a higher pump absorption, and also by modifying the cavity design to obtain better mode matching. With the aid of the model, we can effectively predict the performance of the optimized laser system, guiding future Fe:ZnSe laser design.

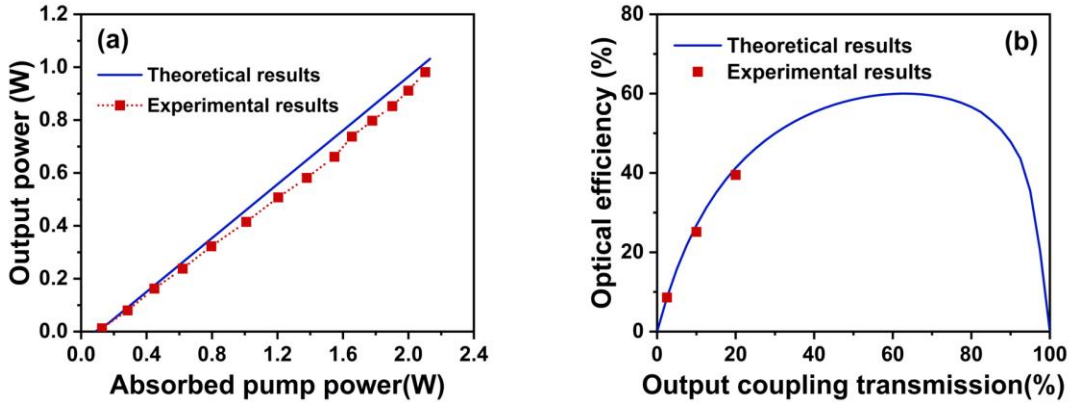

Fig. 3-12. Theoretical calculations of (a) the Fe:ZnSe laser power versus absorbed pump power, and (b) optical-to-optical efficiency versus output coupling transmission. The experimental results are also shown for comparison.

Notably, although our experimental parameters could have been more optimal, the proposed Fe:ZnSe laser still achieved one of the highest optical efficiencies with watt-level output power among all the Fe:ZnSe lasers reported thus far. Table 3-2 compares our experimental results with those of other reported Fe:ZnSe lasers. The Fe:ZnSe laser pumped by a 3 μm Er-doped laser only requires a two-stage pump architecture, compared to those pumped by Cr-doped lasers, indicating a simpler structure and a higher wall-plug efficiency. Further, our self-developed Er:YAP laser shows the advantage of both high output power and high efficiency among all the Er-doped lasers. Thus, due to the good pump source selection and Fe:ZnSe resonator design, we achieved the highest optical conversion efficiency of Fe:ZnSe laser reported thus far.

Table 3-2. Comparison of our results with other reported CW Fe:ZnSe lasers

1st-stage pump	**2nd-stage pump**	**3rd-stage pump**	**Power**	**Efficiency[a]**	**Reference**
LD (--)	Tm:fiber laser (3 W)	Cr:CdSe laser (0.6 W)	0.16 W	5.3% [b]	[3-10]
LD (--)	Er:YAG laser (2.17 W)	--	0.84 W	--	[3-13]
LD (27.7 W)	Er:Y_2O_3 laser (3.15 W)	--	0.42 W	1.5%	[3-14]
LD (--)	Tm:fiber laser (76.5 W)	Cr:ZnSe laser (23 W)	9.2 W	12% [b]	[3-15]
LD (35 W)	Er:ZBLAN laser (3.9 W)	--	2.1 W	6%	[3-16]
LD (11.4 W)	Er:YAP laser (2.5 W)	--	1.0 W	8.8%	**This work**

[a]The overall optical conversion efficiency calculated from the LD to the Fe:ZnSe laser unless otherwise noted.

[b]The optical efficiency with respect to the second-stage pump sources (Tm:fiber lasers).

3.3.2 Thermal Analysis

The major problems hindering power scaling in high-power laser systems are thermal effects, including thermal quenching, thermal lensing, and thermal stress-induced fracture. For Fe:ZnSe crystals, the thermal quenching effect is particularly severe as the lifetime of the upper laser level decreases dramatically with increasing temperature, such that CW lasing cannot be achieved at room temperature. In the rate equation model presented above, the thermal effects were not taken into account because we were operating the laser at low power levels, at which state the thermal effects were mild, and calculated results agreed well with the experimental results. However, to predict the power scaling behavior of the Fe:ZnSe laser, it is necessary to consider the influence of thermal effects on the laser performance at high-power operation. Therefore, we performed a thermal analysis of the end-pumped CW Fe:ZnSe laser using the finite element method.

The main contribution to heat generation in the Fe:ZnSe crystal is generally considered to be quantum defect heating, i.e., the energy difference between the 3-μm pump and the 4-μm laser photon. The heat source function of an end-pumped Fe:ZnSe crystal can be described by [3-30]:

$$Q(r,z)=\frac{2P_p\alpha\gamma}{\pi w_p^2(z)}\exp(-\alpha z)\exp\left(-\frac{2r^2}{w_p^2(z)}\right) \tag{3-7}$$

where $Q(r,z)$ is the heat power per unit volume, P_p is the incident pump power (Er:YAP laser), α is the absorption coefficient of Fe:ZnSe at the pump wavelength (2920 nm), γ is the heat generation efficiency, and $w_p(z)$ represents the pump beam radius, which is assumed to be constant within the crystal. As the Fe:ZnSe crystal was mounted in a copper heat sink that was conductively cooled by liquid nitrogen to 77 K, the boundary conditions for these cooling surfaces can be described by:

$$T|_{x=0}=T|_{x=4}=T|_{y=0}=T|_{y=2}=77\ K \tag{3-8}$$

The other two end facets (z=0 and z=8) were considered as thermally insulating surfaces because the Fe:ZnSe crystal was sealed in an evacuated cryostat. The parameters used for the thermal calculations were based on actual experimental arrangements in conjunction with published data, which are summarized in Table 3-3.

Table 3-3. The parameters used for thermal calculations of Fe:ZnSe laser

Definition	Symbol	Value/unit
Pump absorption coefficient	α	2.6 cm^{-1}
Heat generation efficiency	γ	52% (when using T=20%)
Pump beam radius	w_p	140 μm
Thermal conductivity	K_c	1.03 W/(cm·K) at 80 K [3-31]
Thermal expansion coefficient	α_l	1.8×10^{-6} /K at 80 K [3-32]
Density	ρ	5.3 g/cm^3
Heat capacity	C	331 J/(kg·K)
Young's modulus	E	67.2 GPa

A thermomechanical model was constructed using the COMSOL Multiphysics software to calculate the temperature and thermal stress distribution in the Fe:ZnSe crystal. Figures 3-13 and 3-14 show the typical calculation results for an incident Er:YAP laser pump power of 40 W. The maximum thermal stress occurs at the 4-mm long edge at the pumped surface (see Fig. 3-13), which is mainly attributed to the compressive stress between the crystal and the heat sink induced by thermal expansion. The highest temperature, on the other hand, occurs at the center of the pump area at the front end of the crystal (see Fig. 3-14) because the pump absorption is strongest at this position.

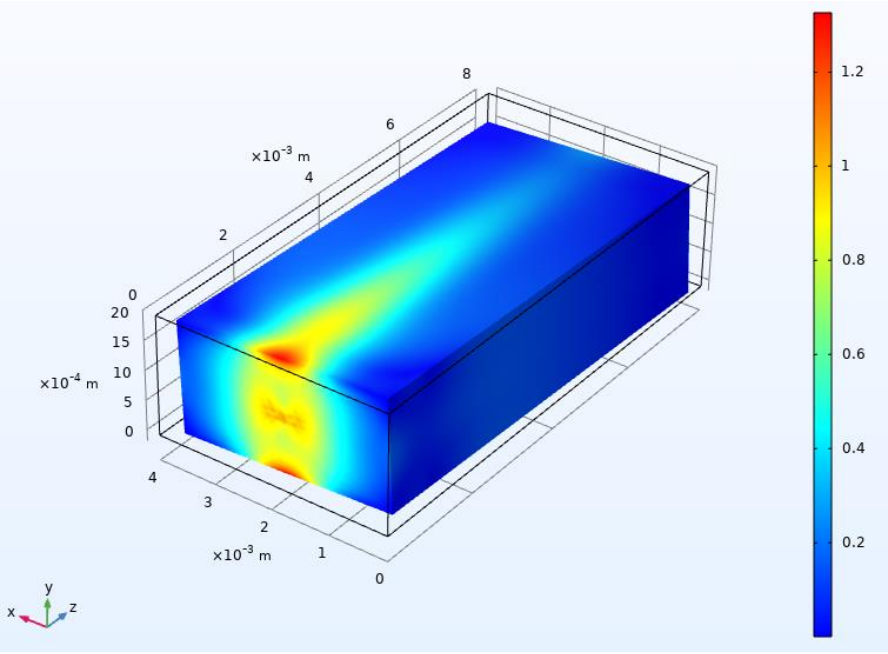

Fig. 3-13. Thermal stress (unit: MPa) distribution of the Fe:ZnSe crystal for an incident pump power of 40 W.

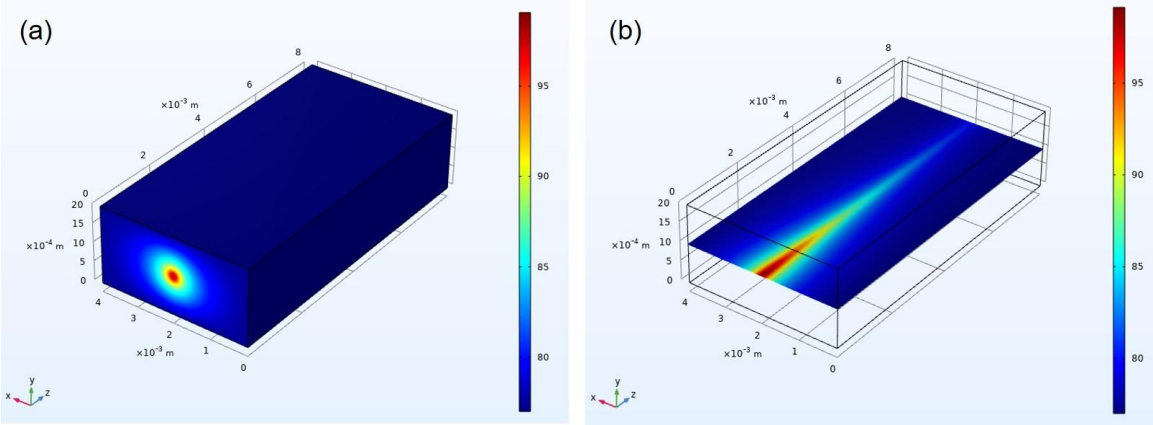

Fig. 3-14. Temperature (unit: K) distribution of the (a) surface and (b) central section of the Fe:ZnSe crystal for an incident pump power of 40 W.

The elevated temperature and the increased stress are the main causes of thermal quenching and thermally induced fracture in Fe:ZnSe lasers, respectively. Here we use the thermal analysis in this section to predict the most dominant reason hindering the power scaling of Fe:ZnSe laser and try to propose possible countermeasures. Figure 3-15(a) shows the maximum temperature and thermal stress inside the Fe:ZnSe crystal as a function of the incident pump power. The maximum temperature increases with a slope of 0.55 K/W with respect to the incident pump power, while the thermal stress increases slightly with a slope of 0.03 MPa/W owing to the small thermal expansion coefficient (~1.8×10^{-6} /K at 80 K [3-32]) of ZnSe at cryogenic temperatures. It has been reported that the laser output power decreases rapidly due to the thermal quenching effect when the crystal temperature exceeds 100 K [3-33], which corresponds to an incident pump power of more than 40 W based on our calculation results (see Fig. 3-15(a)). The maximum stress at an incident pump power of 40 W is calculated to be ~1.3 MPa, which is only 2.6% of the tensile strength of ZnSe (50 MPa), indicating the low likelihood of crystal damage. Therefore, in terms of temperature rise and thermal stress, it is clear that temperature is the more critical factor restricting the power increase.

Another major factor limiting the power scaling of an end-pumped laser is the thermal lensing effect caused by the radial heat flow. This radial heat flow makes the laser medium act equivalently as a lens due to temperature-dependent variation of the refractive index, thus leading to a mismatch between the pump and laser modes or even a destabilization of the laser resonator. Additionally, the presence of a thermal lens can cause wavefront

distortion and hence degrade the laser beam quality. Therefore, it is crucial to evaluate the thermal lensing effect of the gain medium at high power levels. The equivalent thermal focal length of an edge-cooled, end-pumped laser medium can be calculated by [3-34]:

$$f_{th} = \frac{\pi K_c w_P^2}{P_p \gamma (dn/dT)} \left[\frac{1}{1 - \exp(-\alpha_P L_c)} \right] \tag{3-9}$$

where K_c represents the thermal conductivity (~1.03 W/cm·K at 80 K [3-31]), P_p is the incident pump power, γ is the fraction of the absorbed pump power that converted to heat (52% in our case), and dn/dT is the thermo-optic coefficient (~4.7×10^{-5} /K at 4 μm at 80 K [3-35]).

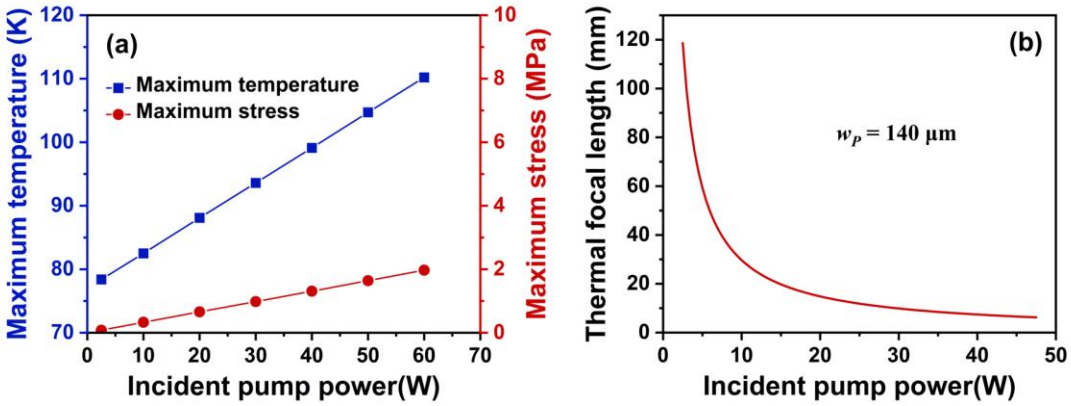

Fig. 3-15. (a) The maximum temperature and thermal stress inside the Fe:ZnSe crystal versus incident pump power. (b) The equivalent thermal focal length versus incident pump power.

Figure 3-15(b) shows the calculated equivalent thermal focal length as a function of the incident pump power for a pump beam radius of 140 μm. The thermal lensing effect is predicted to be relatively strong owing to the large thermo-optic coefficient of the ZnSe matrix. In our experimental arrangement, the minimum thermal focal length which prevents a significant mode mismatch is approximately 11 mm, corresponding to a maximum tolerable incident pump power of about 27 W. Based on this pump power and the rate equation model presented in Section 3.3.1, a highest CW laser power of more than 11 W can be expected with the use of an improved pump source in future studies. For higher output power it is required to mitigate the thermal lensing. One straightforward approach

is to increase the pump beam radius, i.e., the wp in formula (3-9), but this method will inevitably be accompanied by a decrease in lasing efficiency. Additionally, several measures can be taken for active compensation of thermal lensing, such as inserting additional compensating lenses or designing a special surface shape for the crystal.

3.4 Conclusions and Outlook

In conclusion, the study in this chapter presents an efficient and simple way to obtain a compact, watt-level 4-μm CW laser, which is based on an Fe:ZnSe oscillator end pumped by our self-constructed Er:YAP laser. The Er:YAP pump laser generated a stable output power of 3.6 W at 2920 nm, an average slope efficiency of 36.6%, and a beam quality of $M^2 < 2.0$. The Fe:ZnSe oscillator produced a maximum output power of 1 W with a good beam quality ($M^2 < 1.6$) at an absorbed pump power of 2.1 W, corresponding to an average slope efficiency of 48% and an optical-to-optical efficiency of 40%. More importantly, the overall optical conversion efficiency, calculated from the 976-nm diode laser to the 4-μm Fe:ZnSe laser, was 8.8%, which is the highest value reported thus far. These results indicate that the Er:YAP laser can be a reliable pump source for the Fe:ZnSe laser, owing to its high performance, low cost, and power scalable properties. Thus, the Er:YAP-laser-pumped Fe:ZnSe oscillator is a promising approach to achieving a high-efficiency 4-μm laser with compactness and low cost.

Additionally, this study presents a rate equation model of the Fe:ZnSe laser to predict the optimized laser performance. Theoretical calculations demonstrate the considerable scope for further improvement in the power performance by increasing the output coupling transmission to approximately 60% and employing a relatively longer Fe:ZnSe crystal to absorb a greater fraction of the pump light. Moreover, a detailed thermal analysis was performed to evaluate the influence of thermal effects on the power scaling capability of the Fe:ZnSe laser. The thermal lensing effect was found to be the most critical factor hindering the power scaling of the Fe:ZnSe laser. To the best of our knowledge, this is the first study that combines experiment and theoretical analysis in a CW Fe:ZnSe laser system. The theoretical model presented in this study is expected to provide a rough guide for

scaling the power levels of the Fe:ZnSe lasers to the order of tens of watts in future studies.

This study also demonstrates that the Fe:ZnSe laser is capable of combining high output power with high efficiency, indicating that it is an appealing light source for spectroscopy applications. However, the direct lasing from an Fe:ZnSe oscillator is not wavelength controllable. The laser spectrum typically features multiple emission peaks and a wide spanning range, which cannot be matched with a specific absorption peak of the target molecule and is thus unsuitable for applications requiring high measurement precision. Therefore, achieving fine spectral control of Fe:ZnSe lasers is still one of the pressing challenges for the laser community.

References (Chapter III)

[3-1]. M. S. Vitiello, G. Scalari, B. Williams, and P. De Natale, "Quantum cascade lasers: 20 years of challenges," Optics Express, **23**(4), 5167–5182, (2015).

[3-2]. M. Troccoli, C. Gmachl, F. Capasso, D. L. Sivco, and A. Y. Cho, "Mid-infrared (λ~7.4μm) quantum cascade laser amplifier for high power single-mode emission and improved beam quality," Applied Physics. Letters, **80**(22), 4103–4105 (2002).

[3-3]. S. Y. Tochitsky, V. O. Petukhov, V. A. Gorobets, V. V. Churakov, and V. N. Jakimovich, "Efficient continuous-wave frequency doubling of a tunable CO_2 laser in $AgGaSe_2$," Applied Optics, **36**(9), 1882–1888 (1997).

[3-4]. A. Ruehl, A. Gambetta, I. Hartl, M. E. Fermann, K. S. E. Eikema, and M. Marangoni, "Widely-tunable mid-infrared frequency comb source based on difference frequency generation," Optics Letters, **37**(12), 2232–2234 (2012).

[3-5]. P. A. Budni, L. A. Pomeranz, M. L. Lemons, C. A. Miller, J. R. Mosto, and E. P. Chicklis, "Efficient mid-infrared laser using 1.9-μm pumped Ho:YAG and $ZnGeP_2$ optical parametric oscillators," Journal of the Optical Society of America B, **17**(5), 723–728 (2000).

[3-6]. F. K. Tittel, A. A. Kosterev, Y. A. Bakhirkin, G. Wysocki, C.B. Roller, S. So, D. Weidmann, M. Horstjann, and R.F. Curl, "Recent advances of trace gas sensors based on diode and quantum cascade lasers," The 17th Annual Meeting of the IEEE Lasers and Electro-Optics Society, 2004. LEOS 2004. IEEE, **2**, 559–560 (2004).

[3-7]. S. B. Mirov, I. S. Moskalev, S. Vasilyev, V. Smolski, V. V. Fedorov, D. Martyshkin, J. Peppers, M. Mirov, A. Dergachev, and V. Gapontsev, "Frontiers of Mid-IR Lasers Based on Transition Metal Doped Chalcogenides," IEEE Journal of Selected Topics in Quantum Electronics, **24**(5), 1–29 (2018).

[3-8]. Y. Li, L. Xu, Y. Ju, B. Yao, and T. Dai, "Free-running Fe:ZnSe laser pumped by an Er:YAG radiation along the cavity axis," Optik, **194**, 162949 (2019).

[3-9]. D. V. Martyshkin, V. V. Fedorov, M. Mirov, I. Moskalev, S. Vasilyev, and S. B. Mirov, "High average power (35 W) pulsed Fe:ZnSe laser tunable over 3.8-4.2 μm," in CLEO: 2015, (Optical Society of America, 2015), OSA Technical Digest (online), p. SF1F.2.

[3-10]. A. A. Voronov, V. I. Kozlovsky, Yu. V. Korostelin, A. I. Landman, Yu. P. Podmar'kov, Ya. K. Skasyrsky, and M. P. Frolov, "A continuous-wave Fe^{2+}:ZnSe laser," Quantum Electronics, **38**(12), 1113–1116 (2008).

[3-11]. H. Uehara, T. Tsunai, B. Han, K. Goya, R. Yasuhara, F. Potemkin, J. Kawanaka, and S. Tokita, "40 kHz, 20 ns acousto-optically Q-switched 4 μm Fe:ZnSe laser pumped by fluoride fiber laser," Optics Letters, **45**(10), 2788–2791 (2020).

[3-12]. A. V. Pushkin, E. A. Migal, S. Tokita, Y. V. Korostelin, and F. V. Potemkin, "Femtosecond graphene mode-locked Fe:ZnSe laser at 4.4 μm," Optics Letters, **45**(3), 738–741 (2020).

[3-13]. J. W. Evans, P. A. Berry, and K. L. Schepler, "840 mW continuous-wave Fe:ZnSe laser operating at 4140 nm," Optics Letters, **37**(23), 5021–5023 (2012).

[3-14]. J. W. Evans, T. Sanamyan, and P. A. Berrya, "A continuous-wave Fe:ZnSe laser pumped by an efficient Er:Y_2O_3 laser," Proc. SPIE, **9342**, 93420F (2015).

[3-15]. D. V. Martyshkin, V. V. Fedorov, M. Mirov, I. Moskalev, S. Vasilyev, V. Smolski, A. Zakrevskiy, and S. B. Mirov, "High Power (9.2 W) CW 4.15 μm Fe:ZnSe laser," in Conference on Lasers and Electro-Optics, OSA Technical Digest (online) (Optical Society of America, 2017), STh1L.6.

[3-16]. A. V. Pushkin, E. A. Migal, H. Uehara, K. Goya, S. Tokita, M. P. Frolov, Y. V. Korostelin, V. I. Kozlovsky, Y. K. Skasyrsky, and F. V. Potemkin, "Compact, highly efficient, 2.1 W continuous-wave mid-infrared Fe:ZnSe coherent source, pumped by an Er:ZBLAN fiber laser," Optics Letters, **43**(24), 5941–5944 (2018).

[3-17]. I. Moskalev, S. Mirov, M. Mirov, S. Vasilyev, V. Smolski, A. Zakrevskiy, and V. Gapontsev, "140 W Cr:ZnSe laser system," Optics Express, **24**(18), 21090–21104 (2016).

[3-18]. S. Tokita, M. Murakami, and S. Shimizu, "High Power 3 μm Erbium Fiber Lasers," in Advanced Solid State Lasers, OSA Technical Digest (online) (Optical Society of America, 2014), AM3A.4.

[3-19]. W. Yao, H. Uehara, H. Kawase, H. Chen, and R. Yasuhara, "Highly efficient Er:YAP laser with 6.9 W of output power at 2920 nm," Optics Express, **28**(13), 19000–19007 (2020).

[3-20]. J. Koetke and G. Huber, "Infrared excited-state absorption and stimulated-emission cross sections of Er^{3+}-doped crystals," Applied Physics B, **61**(2), 151–158 (1995).

[3-21]. T. Li, K. Beil, C. Kränkel, and G. Huber, "Efficient high-power continuous wave Er:Lu_2O_3 laser at 2.85 μm," Optics Letters, **37**(13), 2568–2570 (2012).

[3-22]. C. Quan, D. Sun, J. Luo, H. Zhang, Z. Fang, X. Zhao, L. Hu, M. Cheng, Q. Zhang, and S. Yin, "2.7 μmdual-wavelength laser performance of LD end-pumped Er:YAP crystal," Optics Express **26**(22), 28421–28428 (2018).

[3-23]. A. A. Voronov, V. I. Kozlovskii, Yu. V. Korostelin, A. I. Landman, Yu. P. Podmar'kov, and M. P. Frolov, "Laser parameters of a Fe:ZnSe laser crystal in the 85-255K temperature range," Quantum Electronics, **35**(9), 809–812 (2005).

[3-24]. J. A. Caird, S. A. Payne, P. Staber, A. Ramponi, L. Chase, and W. F. Krupke, "Quantum electronic properties of the $Na_3Ga_2Li_3F_{12}$:Cr^{3+} laser" IEEE Journal of Quantum Electronics, **24**, 1077–1099 (1988).

[3-25]. J. W. Evans, T. R. Harris, B. R. Reddy, K. L. Schepler, and P. A. Berry, "Optical spectroscopy and modeling of Fe^{2+} ions in zinc selenide," Journal of Luminescence, **188**, 541–550 (2017).

[3-26]. Q. Pan, F. Chen, J. Xie, C. Wang, Y. He, D. Yu, and K. Zhang, "Theoretical study of the characteristics of a continuous wave iron-doped ZnSe laser," Laser Physics, **28**(3), 035002 (2018).

[3-27]. A. Sennaroglu, A. Ozgun Konca, and C. R. Pollock, "Continuous-wave power performance of a 2.47-μm Cr^{2+}:ZnSe laser: Experiment and modeling," IEEE Journal of Quantum Electronics, **36**(10), 1199–1205 (2000).

[3-28]. J. W. Evans, R. W. Stites, and T. R. Harris, "Increasing the performance of an Fe:ZnSe laser using a hot isostatic press," Optical Materials Express, **7**(12), 4296–4303 (2017).

[3-29]. H. Cankaya, U. Demirbas, A. K. Erdamar, and A. Sennaroglu, "Absorption saturation analysis of Cr^{2+}:ZnSe and Fe^{2+}:ZnSe," Journal of the Optical Society of America B, **25**(5), 794–800 (2008).

[3-30]. H. Zhang, Y. Wen, L. Zhang, Z. Fan, J. Liu, and C. Wu, "Influences of pump spot radius and depth of focus on the thermal effect of Tm:YAP crystal," Current Optics and Photonics, **3**(5), 458–465 2019.

[3-31]. G. Slack, “Thermal Conductivity of II-VI Compounds and Phonon Scattering by Fe^{2+} Impurities,” Physical Review B, **6**(10), 3791–3800 (1972).

[3-32]. J. S. Browder and S. S. Ballard, “Low temperature thermal expansion measurements on optical materials,” Applied Optics, **8**(4), 793–798 (1969).

[3-33]. J. W. Evans, P. A. Berry, and K. L. Schepler, “A broadly tunable continuous-wave Fe:ZnSe laser,” Proc. SPIE **8599**, 85990C (2013).

[3-34]. M. E. Innocenzi, H. T. Yura, C. L. Fincher, and R. A. Fields, “Thermal modeling of continuous-wave end-pumped solid-state lasers,” Applied Physics Letters, **56**(19), 1831–1833 (1990).

[3-35]. D. B. Leviton, B. J. Frey, and T. Kvamme, “High accuracy, absolute, cryogenic refractive index measurements of infrared lens materials for JWST NIRCam using CHARMS,” Proc. SPIE **5904**, 59040O (2005).

IV. Hybrid Fe:ZnSe Amplifier for High-power, Narrow-linewidth, and Widely Tunable MIR Lasers

4.1 Problems of Fe:ZnSe Oscillator and Solutions

As described in the previous chapter, despite the remarkable lasing performance of Fe:ZnSe, the difficulties in achieving spectrally narrow-linewidth laser operation have restricted their usage in high-precision spectroscopy applications. Typically, a CW Fe:ZnSe laser with watt-level output power emits multiple spectral peaks with a spanning range of approximately 100 nm [4-1][4-2], as shown in Fig. 4-1. This broad-spectrum property is primarily attributed to the inhomogeneous broadening [4-3] of Fe:ZnSe, which results in an ultrabroad and smooth emission spectrum (see the orange curve in Fig. 4-1). In a non-selective laser resonator, this spectral property makes the laser oscillation can occur at multiple wavelengths. Figure 4-2 schematically diagrams the mechanism of this broadband lasing behavior [4-4]. Due to the Fabry-Perot interference effect, the resonator only allows discrete optical frequencies that satisfy the constructive interference to oscillate within the cavity. Therefore, for a gain medium with a broader and smoother fluorescence spectrum, more frequencies can meet the oscillation condition, i.e., the net gain is sufficiently above the laser threshold and oscillate in the cavity, thus emitting multiple laser wavelengths. In the example shown in Fig. 4-2, the laser can oscillate at seven modes.

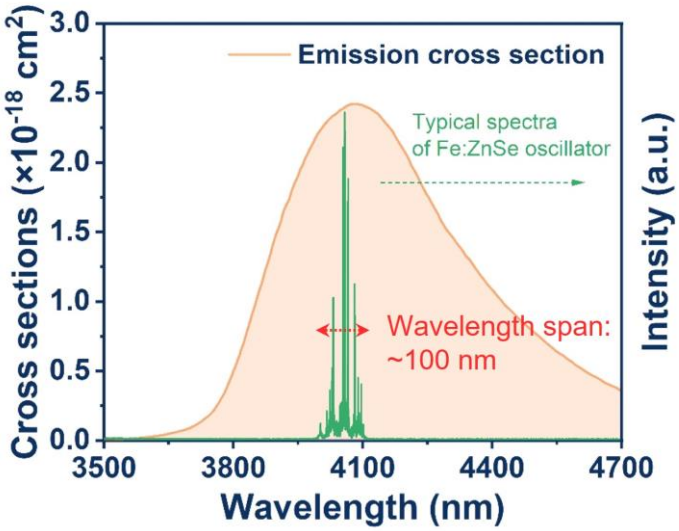

Fig. 4-1. Typical emission spectrum of a watt-level Fe:ZnSe laser oscillator.

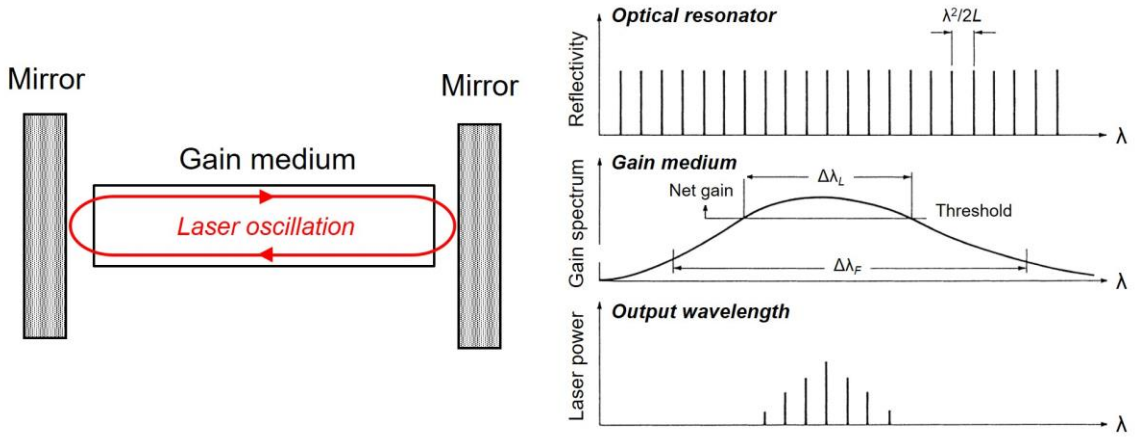

Fig. 4-2. Typical Fabry-Pérot resonator and the mechanism of its spectral output [4-4].

Several wavelength selection methods can be used to narrow the laser linewidths and achieve tunable laser outputs, such as the deployment of prisms [4-5], filters [4-6], or diffraction gratings [4-7] inside the resonator. The purpose of inserting these elements is to limit the number of optical frequencies that can build up oscillations within the cavity, i.e., the number of modes in optical resonator in Fig. 4-2. Nevertheless, the shortest spectral linewidth achieved to date from Fe:ZnSe laser using this method is only 2 nm (FWHM) [4-7]. Single-frequency mid-infrared sources or those with narrower linewidths are still urgently needed to fulfill the requirements of high-resolution spectroscopy applications.

A previous study reported that hot isostatic press treatment of an Fe:ZnSe crystal could convert it from an inhomogeneously broadened gain medium to a homogeneously broadened one, thus narrowing its lasing linewidth to < 1 nm [4-3]. However, tunable lasing characteristics were not investigated, and single-frequency laser operation still could not be achieved using this method alone. Combining several spectral narrowing components, such as a birefringent filter and an etalon, with a short cavity appears to be effective in achieving single-frequency operation; however, it inevitably introduces large cavity losses and thus degrades the laser power. Therefore, it has not received much attention.

In this study, we propose a more straightforward method to achieve a high-power single-frequency 4–5 μm laser, which is based on an Fe:ZnSe amplifier design. Laser amplifiers are another common architecture other than laser oscillators for generating high-power lasers. A schematic diagram of an end-pumped laser amplifier is illustrated in Fig. 4-3. The main function of the laser amplifier is to increase the brightness of an input signal,

namely the seed light. Therefore, the spectral, spatial, and temporal properties of the output from a laser amplifier are completely determined by the input seed light.

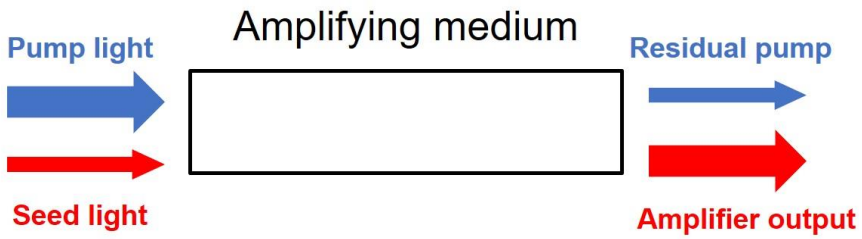

Fig. 4-3. Schematic diagram of an end-pumped, end-injected laser amplifier.

In the Fe:ZnSe amplifier scheme, the Fe:ZnSe is simply used to increase the power of the injected seed light while keeping its spectral and spatial properties unchanged. Thus, finding a suitable narrow-linewidth laser source as the input signal is the first priority. The quantum cascade laser (QCL) has been a commercial success since its invention. Currently, the QCLs can easily achieve single-frequency laser operation by incorporating a Bragg grating inside the QCL chip, namely the distributed feedback QCL (DFB-QCL), or by building a grating-coupled external cavity outside the QCL, namely the external-cavity QCL (EC-QCL) [4-8]. Figure 4-4 shows schematically the DFB-QCL and EC-QCL architectures. However, the output powers of these QCL architectures are generally limited to the order of tens of milliwatts owing to their introduction of strong mode confinement and the intrinsically small active area of the QCL chip. Thus, a single-frequency QCL and an Fe:ZnSe amplifier can complement each other well. Their combination is thus natural and expected to realize high-power, single-frequency laser operation in the 4–5 μm band.

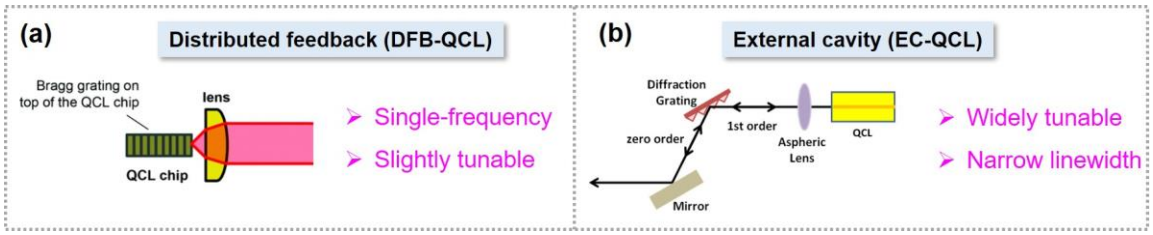

Fig. 4-4. Possible narrow-linewidth seed lasers for Fe:ZnSe amplifiers: (a) Distributed feedback QCL. (b) External cavity QCL.

In this chapter, we first present a proof-of-concept study on a hybrid Fe:ZnSe laser amplifier seeded with commercial Fabry-Perot QCLs to verify the feasibility of Fe:ZnSe in amplifying spectrally broadband lasers operating at ~4.0 μm and ~4.6 μm. Thereafter, we seed the Fe:ZnSe amplifier using a commercial DFB-QCL and an inhouse-built EC-QCL, demonstrating a record high-power, pure single-frequency laser operating at 4.3 μm and a high-power, narrow-linewidth, and widely tunable laser with a tuning range of 630 nm, respectively. The input-output, temporal, spatial, and spectral characteristics of the Fe:ZnSe amplifier are studied in detail. Furthermore, a theoretical model based on the Fe:ZnSe rate equations applicable to the amplifier regime is proposed, and approaches for optimizing performance are discussed.

4.2 Proof-of-concept Study on the Hybrid Fe:ZnSe Amplifier

4.2.1 Experimental Setup of FP-QCL/Fe:ZnSe Amplifier

We first conducted a proof-of-concept experiment on this hybrid Fe:ZnSe amplifier scheme. A single-pass laser amplifier system consisting of a seed-injection section and an Fe:ZnSe amplifier section was constructed, as shown in Fig. 4-5. Two Fabry-Perot QCLs (FP-QCLs) emitting broadband spectra with lasing central wavelengths of ~4.0 μm (QF4050T1, Thorlabs) and ~4.6 μm (QF4600T2, Thorlabs) were used as seeds. The output from the FP-QCL was first collimated by an aspheric lens with 3-mm focal length and then focused to an elliptical beam radius of approximately 150×200 μm in the vertical and horizontal directions, respectively, by a 100-mm focal-length lens. A free-space optical isolator (ISO in Fig. 4-5) was inserted between the two lenses to block back reflections, preventing the impact of feedback on the FP-QCL performance. The seed laser was steered into the amplifier stage via a dichroic mirror (DM1) with high reflectivity (HR>95%) in the range 3.6–5.0 μm and high transmission (HT>90%) at 2.6–3.1 μm. With the above optical elements in space, the maximum incident seed powers on the Fe:ZnSe crystal were 200 mW and 150 mW for the 4.0-μm and 4.6-μm FP-QCLs, respectively.

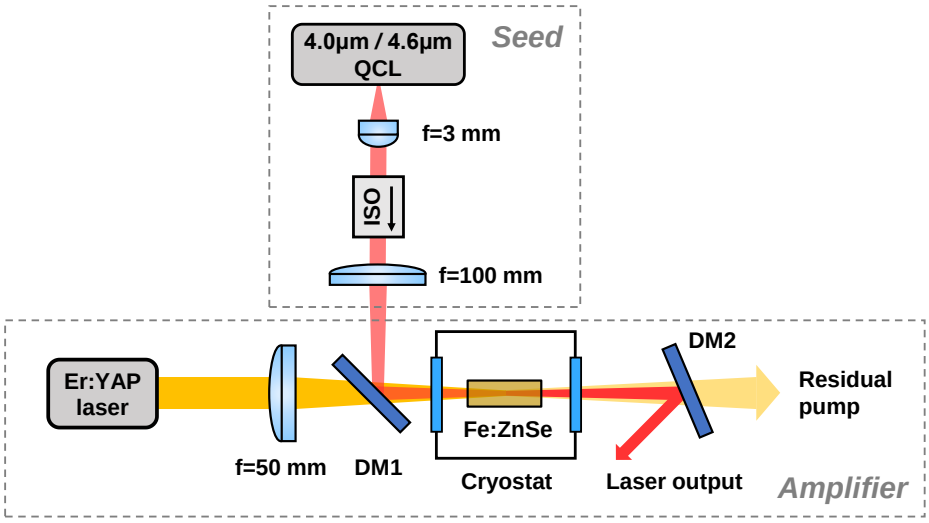

Fig. 4-5. Schematic of the single-pass Fe:ZnSe amplifier seeded by an FP-QCL.

The pump source of the Fe:ZnSe amplifier was the same Er:YAP laser as described in Section 3.2.1, Fig. 3-2(a). The Er:YAP pump laser could provide 3.6 W of output power with a stably high beam quality. The output from the Er:YAP laser was directly focused to a beam radius of approximately 140 μm using a CaF_2 lens with a focal length of 50 mm. This 140-μm pump radius was deliberately selected to be slightly smaller than the minor axis of the seed beam to ensure a high mode-matching efficiency. The overall transmission of the pump delivery optics was approximately 70%, resulting in a maximum of 2.5 W of pump power incident upon the Fe:ZnSe crystal.

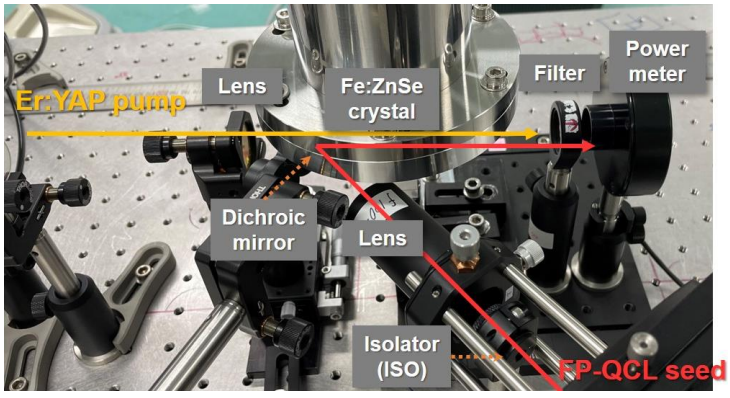

Fig. 4-6. Photograph of the Fe:ZnSe amplifier section.

Figure 4-6 shows the photograph of the Fe:ZnSe amplifier section. Two Fe:ZnSe single crystals with different Fe^{2+}-ion doping concentrations were used in the experiments. The low-doped crystal was grown by the seeded physical vapor transport technique [4-9], which

had an Fe^{2+}-ion concentration of 2.2×10^{18} cm^{-3} with a dimension of 2 mm×4 mm in cross-section and 8 mm in length. The high-doped crystal was commercially ordered from 3photon, which had an Fe^{2+}-ion concentration of 1×10^{19} cm^{-3} with a dimension of 2 mm × 5 mm in cross-section and 2.73 mm in length. Figure 4-7 shows the typical transmission spectrum of the high-doped Fe:ZnSe sample measured using a Fourier-transform infrared spectroscopy analyzer. By comparing the transmittance outside the absorption band of Fe:ZnSe (around 1500 nm) with the ideal Fresnel transmittance calculated from the refractive index of ZnSe, the passive optical loss for both the high-doped and low-doped crystals was estimated to be <0.04 cm^{-1}. Both the Fe:ZnSe crystals were antireflection coated at 2.8–5.2 μm on their end facets. The small-signal absorption of the low-doped Fe:ZnSe and high-doped Fe:ZnSe at 2920 nm was experimentally measured to be about 85% and 96%, respectively, at the liquid-nitrogen cooling temperature (77 K). The crystal was liquid-nitrogen-cooled to prevent the thermal quenching effect, thus providing sufficient gain. The two cryostat windows were made of BaF_2, which was antireflection coated at 2-5 μm with transmissions of 91% and 99% at the pump and laser wavelengths, respectively. Another dichroic mirror (DM2), coated for high reflectivity (HR>99%) at the lasing wavelengths and high transmission (HT>90%) at the pump wavelength, was placed behind the amplifier to separate the amplified laser output from the residual pump light. A thermopile power meter (919P-003-10, Newport) in conjunction with a bandpass filter was used to measure the laser output power.

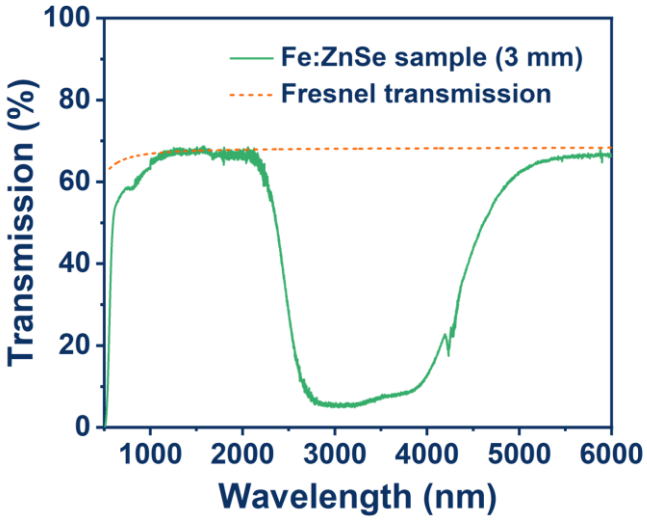

Fig. 4-7. Transmission spectrum of the high-doped Fe:ZnSe sample.

4.2.2 Laser Output Characteristics

The 4.0-μm FP-QCL was first used to seed the Fe:ZnSe amplifier. The detailed amplification properties of the high-doped and low-doped Fe:ZnSe crystals were studied for various incident pump power and injected seed power. The small-signal gain (SSG) coefficient g_0 as a function of the incident pump power is shown in Fig. 4-8(a). To measure the SSG, a probe light with a power of approximately 2 mW was injected into the amplifier. The SSG coefficients g_0 increased almost linearly with the incident pump power for both high-doped and low-doped crystals, and the SSG coefficient of the low-doped Fe:ZnSe was considerably smaller than that of the high-doped one at high pump power levels, which was primarily due to the small inverted population (i.e., $g_0 = \sigma n$, where σ represents the gain cross-section and n represents the inverted population) because of the low doping concentration. Maximum SSG coefficients at 2.5 W of incident pump power were measured to be 12.7 cm^{-1} and 2.6 cm^{-1} for the high-doped and low-doped crystals, respectively. Notably, there was no saturation of the SSG with increasing pump power, indicating that further increase in the SSG can be achieved by slightly increasing the pump intensity, however it will be limited by the onset of parasitic oscillation owing to the imperfect antireflection coating of the crystal end facets. Parasitic oscillation is the phenomenon that laser oscillation can build up spontaneously when the inverted population in the gain medium is sufficiently large and the gain is sufficiently high, thus resulting in rapid consumption of the stored energy. This phenomenon is particularly pronounced in the presence of internal reflections or strong feedback. The critical conditions for the onset of parasitic oscillation can be given by [4-10]:

$$R_1 R_2 \exp(2 g_0 l) \geq 1 \tag{4-1}$$

where R_1 and R_2 represent the reflectivities of the two end facets of Fe:ZnSe, which were experimentally measured to be about 4%; and l represents the crystal length. The upper limit of g_0 for the onset of parasitic oscillation for the high-doped Fe:ZnSe crystal was calculated to be $g_0 = 14.3$ cm^{-1}, corresponding to a threshold pump power of 2.7 W.

Figure 4-8(b) shows the variation in the amplifier gain with respect to the injected seed power. The amplifier gains decreased as the injected seed power increased owing to the saturation effect and became relatively steady when the seed power exceeded 100 mW,

which were approximately 4.4 and 3.2 for the high-doped and low-doped Fe:ZnSe, respectively. This indicates that effective laser amplification can also be achieved even with the injection of a watt-level seed, implying the feasibility of deploying multiple-stage amplifier chains based on our amplifier design to achieve a higher laser power. It is also worth noting that with the increase of the injected seed power, the gains of the high-doped and low-doped Fe:ZnSe amplifiers tend to be consistent. This can also be attributed to the gain saturation effect at high seed power levels, as the laser gain provided by the Fe:ZnSe crystal was no longer as high as the small-signal gain due to the significant depletion of the inverted population.

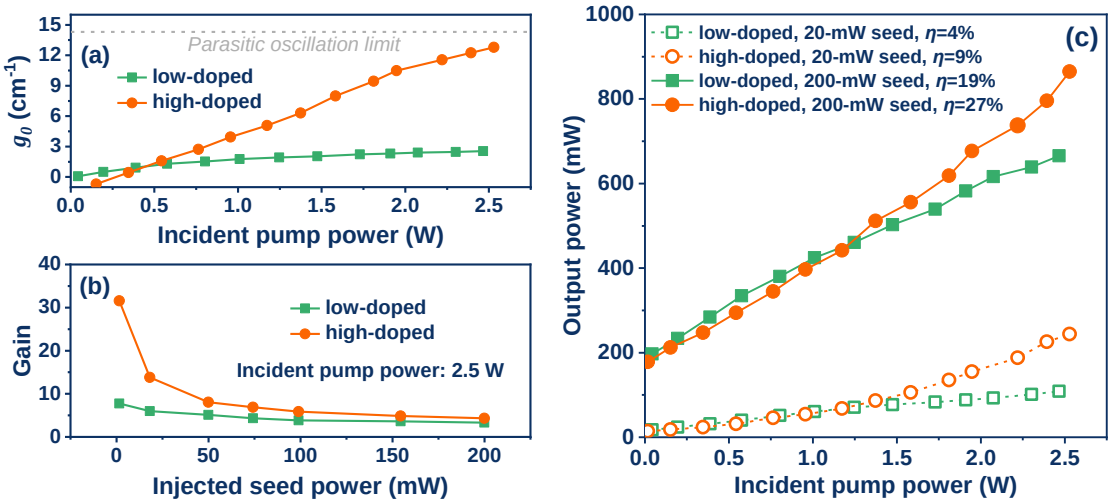

Fig. 4-8. Output performance of the Fe:ZnSe amplifier seeded by a 4.0-μm FP-QCL. (a) Small-signal gain versus incident pump power. (b) Amplifier gain versus injected seed power at 2.5 W of incident pump power. (c) Output power versus incident pump power for amplifying 20-mW and 200-mW seeds.

Figure 4-8(c) shows the amplifier output power as a function of the incident pump power for amplifying 20-mW and 200-mW seeds. The threshold pump power for positive net gain was typically below 150 mW, and the high-doped crystal showed a higher threshold owing to the larger reabsorption loss, resulting in higher output power for the low-doped crystal at pump powers below 1.2 W. At the maximum injected seed power of 200 mW, both the high-doped and low-doped crystals exhibited higher average slope efficiencies than those injected with a 20-mW seed. This is because a higher seed power

can enhance the stimulated emission, thereby enabling a higher extraction efficiency (the ratio of the extracted laser power to the absorbed pump power). Additionally, compared to the low-doped Fe:ZnSe crystal, the high-doped one had a higher gain at the high-power level because a greater fraction of the incident pump power can be absorbed, and consequently a larger inverted population can be achieved. At an incident pump power of 2.5 W, the high-doped Fe:ZnSe amplifier produced a maximum output power of 870 mW for amplifying a 200-mW seed, corresponding to a gain of approximately 4.4. The extraction efficiency was 30%, which was about 41% of the Stokes limit, implying that a further increase in the extraction efficiency could be achieved by using a multipass amplifier design or slightly increasing the seed power.

We then characterized the laser spectra before and after amplification using a Fourier transform optical spectrum analyzer (Bristol 771B-MIR) with a spectral resolution of 0.1 nm. Figure 4-9(a) shows the measured spectra at the maximum seed power (orange dashed curve) and the maximum amplifier output power (green solid line). Two major emission peaks located at 3950 nm and 3970 nm exist in the spectrum, and the longer wavelength (i.e., 3970 nm) experienced a higher gain compared to that of 3950 nm after amplification because it is closer to the gain peak of the Fe:ZnSe crystal [4-3]. The spectral bandwidth was approximately 50 nm. Note that there was no amplified spontaneous emissions or parasitic oscillations during the amplification process, indicating that the Fe:ZnSe amplifier preserved the spectral properties of the FP-QCL seed well.

Thereafter, the laser beam qualities before and after amplification were characterized using the 90/10 knife-edge method. We deployed a CaF_2 lens with a focal length of 75 mm to focus the output from the amplifier and then measured the beam radii along the propagation path. Figure 4-9(b) depicts the measured beam qualities at the highest output power before and after amplification. Note that a minor improvement in the beam quality was observed after amplification. The beam-quality factor M^2 was measured to be M_x^2 = 1.6 and M_y^2 = 1.5 before the amplifier, and then decreased to M_x^2 = 1.3 and M_y^2 = 1.2 after amplification. This improvement in beam quality can be attributed to the relatively smaller pump spot size compared to that of the seed beam, such that the center of the beam was significantly amplified, while the energy at the edges could be neglected.

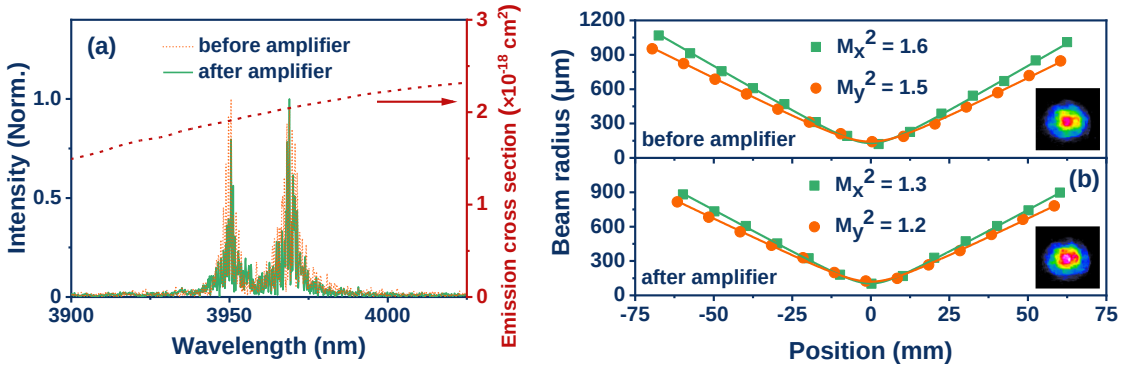

Fig. 4-9. (a) Laser spectra measured before and after amplification. The red dashed line is the emission cross-section of Fe:ZnSe at 80 K [4-3]. (b) Laser beam qualities measured before and after amplification. The insets show the two-dimensional beam profiles recorded by an infrared camera.

To investigate the amplification properties near the gain edge of Fe:ZnSe, we then used the 4.6-μm FP-QCL to seed the Fe:ZnSe amplifier. Figure 4-10 summarizes its output characteristics. At the maximum incident pump power of 2.5 W, the SSGs were measured to be 1.46 and 1.38 for the high-doped and low-doped Fe:ZnSe crystals, respectively, corresponding to SSG coefficients g_0 of 1.39 cm^{-1} and 0.4 cm^{-1}, respectively. In contrast to amplifying the 4.0-μm FP-QCL, the gains at 4.6 μm decreased almost linearly with increasing seed power (see Fig. 4-10(a)) rather than exhibiting a saturation trend as an inversely proportional function. We attribute this linear decrease to a high saturation intensity value due to the low emission cross-section of Fe:ZnSe at 4.6 μm. It is known that efficient energy extraction from a laser amplifier requires the input seed intensity to be comparable to the saturation intensity of the corresponding laser transition [4-11]. The saturation intensity I_s can be given by:

$$I_s = h\nu / \sigma\tau_f \tag{4-2}$$

where $h\nu$ is the 4.6-μm photon energy, σ represents the emission cross-section (0.5×10^{-18} cm^2 at 4.6 μm), and τ_f represents the fluorescence lifetime of the upper laser level (57 μs). Therefore, in the case of amplifying a 4.6-μm seed, the seed intensity required to efficiently extract the stored energy is calculated to be 1.5 kW/cm^2, indicating that a watt-level input signal is required to obtain a higher extraction efficiency.

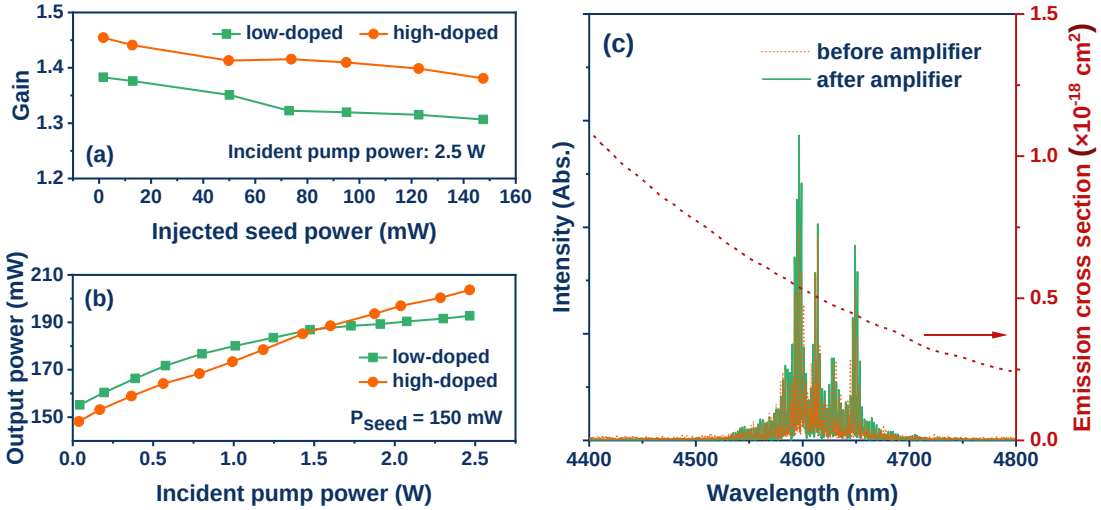

Fig. 4-10. Output characteristics of the Fe:ZnSe amplifier seeded by a 4.6-μm FP-QCL. (a) Amplifier gain versus injected seed power at 2.5 W of incident pump power. (b) Output power versus incident pump power for amplifying a 150-mW seed. (c) Laser spectra measured before and after amplification. The red dashed line is the emission cross-section of Fe:ZnSe at 80 K [4-3].

Figure 4-10(b) shows the amplifier output power as a function of the incident pump power for amplifying a 150-mW seed. The thresholds for positive net gain were reached for an incident pump power of approximately 50 mW. These relatively lower thresholds compared to those of the 4.0-μm amplifiers were primarily owing to the lower reabsorption loss of Fe:ZnSe at 4.6 μm. The high-doped Fe:ZnSe amplifier produced a maximum output power of 204 mW at the maximum incident pump power of 2.5 W, and the corresponding single-pass gain was only 1.38. This relatively low gain was attributed to the small emission cross-section of Fe:ZnSe at 4.6 μm, which is about four times smaller than that at 4.0 μm. The maximum extraction efficiency achieved experimentally was 3.5%, and the maximum slope efficiency was 2.3%, implying that a large fraction of the stored energy was not effectively extracted by the input signal. More efficient energy extraction and hence a higher laser gain can be achieved by using a multipass amplifier arrangement.

The laser spectra of the 4.6-μm Fe:ZnSe amplifier were also recorded before and after amplification, as shown in Fig. 4-10(c). The spectra showed an emission peak at 4590 nm with a spectral bandwidth of about 155 nm. The relatively weak increase in spectral intensity after amplification evidenced the low single-pass gain of Fe:ZnSe at 4.6 μm.

4.2.3 Theoretical Modeling of Fe:ZnSe Laser Amplifier

In the analysis of the experimental results mentioned above, several viable approaches have been proposed to enhance the extraction efficiency and hence output power of the amplifier system. To predict the performance of the optimized amplifier system, we then conducted theoretical modeling of the Fe:ZnSe laser amplifier by modifying the rate equations presented in Section 3.3.1. As the laser signal in the amplifier regime only passes through the gain medium once or a few times and no reflecting cavity mirrors are used, the boundary conditions for solving these rate equations do not need to satisfy the self-consistency as in the case of an oscillator regime. Figure 4-11 illustrates the model of an end-pumped, end-injected single-pass Fe:ZnSe laser amplifier. The boundary conditions can be described by:

$$I_P^+(0) = I_P^l \ , \ I_P^-(L_c) = I_P^r \ , \ I_L^+(0) = I_{seed} \ , \ I_L^-(L_c) = R_2 I_L^+(L_c) \qquad (4\text{-}3)$$

where $I_P{}^l$ and $I_P{}^r$ are the average intensities of the forward and backward pump lights, respectively; for our experimental case, $I_P{}^r = 0$. I_{seed} is the input signal intensity, which was assumed to be forward propagation; and R_2 represents the reflectivity of the rear surface of Fe:ZnSe, induced by the imperfect coating. For the single-pass amplifier configuration, the output performance can be calculated by numerically solving the rate equations (3-4)–(3-5) only once using the boundary conditions (4-3).

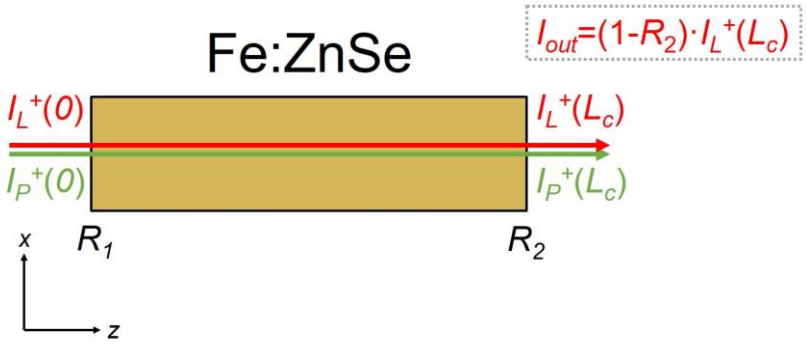

Fig. 4-11. Model of an end-pumped, end-injected single-pass Fe:ZnSe amplifier.

In addition, note that some approximations can be used to simplify the calculation. First, the mode-matching factor η in Equations (3-4) and (3-5) can be considered to be 1 because the entire pump area is within the seed beam area. Thus, all the stored energy in the

pumping volume can be extracted by the input signal. Furthermore, it was assumed that the seed intensity in the outer regions of the pump area was negligible, which is reasonable because the QCL has a typical Gaussian intensity distribution with most of the energy located near the center, such that all the injected seed power is considered to be amplified. Figure 4-12 shows a typical calculation result of the theoretical Fe: ZnSe amplifier model.

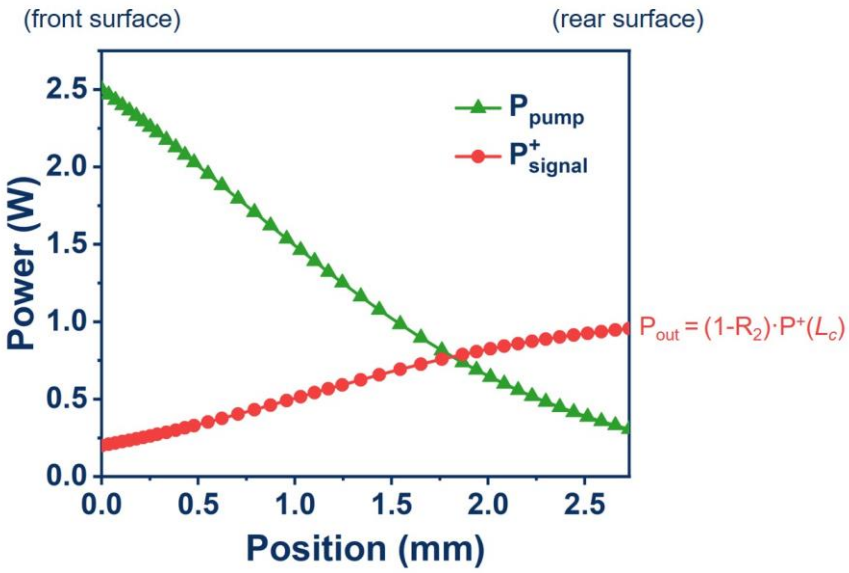

Figure 4-12. Typical calculation result of amplifying a 200-mW, 4-μm seed using the high-doped Fe:ZnSe at an incident pump power of 2.5 W.

The output characteristics can be calculated for various amplifier configurations using this modified rate equation model applicable to the amplifier regime. Here, we mainly predicted the output performance of the high-doped Fe:ZnSe amplifier because it experimentally enabled a better amplification performance. Figure 4-13(a) shows the calculated amplifier output power as a function of the incident pump power when amplifying the 200-mW, 4.0-μm and 150-mW, 4.6-μm signals. The experimental results are also included for comparison. The theoretical calculations concurred with our experimental results at low pump power levels. At high power levels, the calculated output powers are slightly higher than the experimental results for both amplifiers, which can be attributed to the mode mismatch caused by thermal lensing within the crystal. Figures 4-13(b) and 4-13(c) show the calculated amplifier gain as a function of the injected seed power at 2.5 W of incident pump power for the 4.0-μm and 4.6-μm amplifiers, respectively. The calculated gain of the 4.0-μm amplifier (see Fig. 4-13(b)) can be fully saturated when

the seed power reaches nearly 1 W. The saturated gain was calculated to be approximately 2, predicting an output power of 2 W for an injected seed power of 1 W. The corresponding extraction efficiency of this single-pass 4.0-μm amplifier could reach approximately 42%. Furthermore, we can predict that further scaling up the output power to over tens of watts is possible by building a multistage system with several amplifier stages in cascade, i.e., an amplifier chain. For the 4.6-μm amplifier, we can notice an appreciable difference between the calculated and experimental results (see Fig. 4-13(c)). This discrepancy can be attributed to the low extraction efficiency of the 4.6-μm amplifier, such that a large fraction of the absorbed pump power is converted to heat, which strengthens the thermal lensing and thermal quenching effects, thereby degrading the experimental amplification performance. Further improvement in the calculation accuracy of the theoretical model could be achieved by incorporating the influence of thermal effects (thermal lensing on mode-matching efficiency and thermal quenching on fluorescence lifetime) into the model.

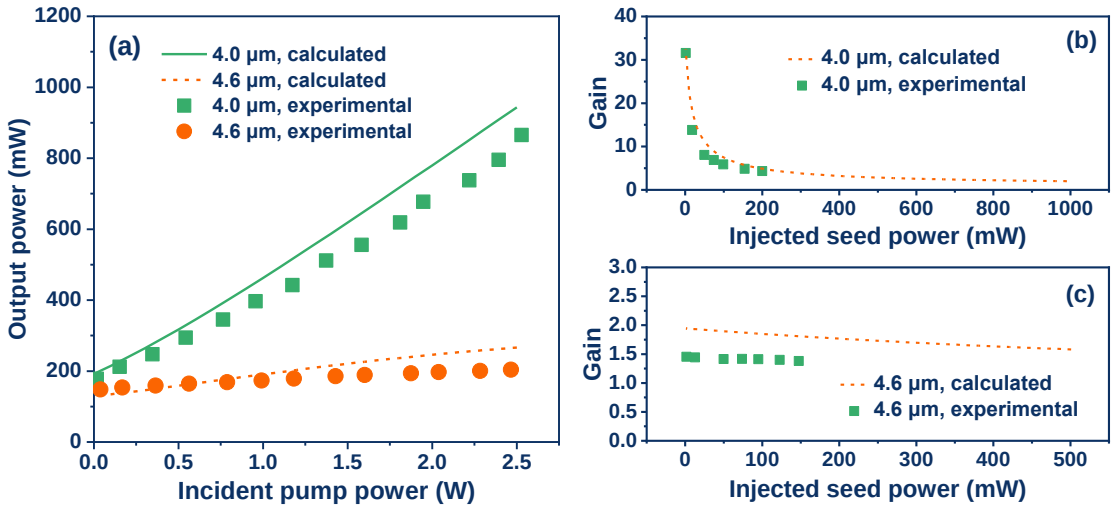

Fig. 4-13. Calculated output performance of the Fe:ZnSe amplifier. (a) Amplifier output power versus incident pump power. (b) Amplifier gain versus injected seed power for the 4.0-μm amplifier. (c) Amplifier gain versus injected seed power for the 4.6-μm amplifier.

A highly effective way to increase the extraction efficiency and thus the overall amplifier gain at a limited pump power is to employ a multipass amplifier arrangement, in which the input signal can be directed through the amplifier several times to experience multiple amplification processes. With several passes through the gain medium, the stored

energy in Fe:ZnSe can be efficiently extracted, resulting in a significant enhancement of the signal intensity. To predict the output performance of a multipass Fe:ZnSe amplifier, we modified the theoretical model by applying the output intensity of each pass as the initial input condition for the next pass. A reflection loss of 1% was introduced to realistically describe the reflected injection of the seed. Figure 4-14 shows the calculated output power and extraction efficiency as functions of the number of passes. For amplifying a 200-mW, 4.0-μm seed, the output power and extraction efficiency will saturate after the second pass (see Fig. 4-14(a)), resulting in an output power of more than 1.1 W and an extraction efficiency of over 40%. For amplifying a 150-mW, 4.6-μm seed, the amplification will saturate after the fourth pass (see Fig. 4-14(b)), with an output power of more than 540 mW and an extraction efficiency of more than 18%. Altogether, theoretical calculations demonstrate that the multipass configuration is reasonably effective in promoting energy extraction and increasing output power.

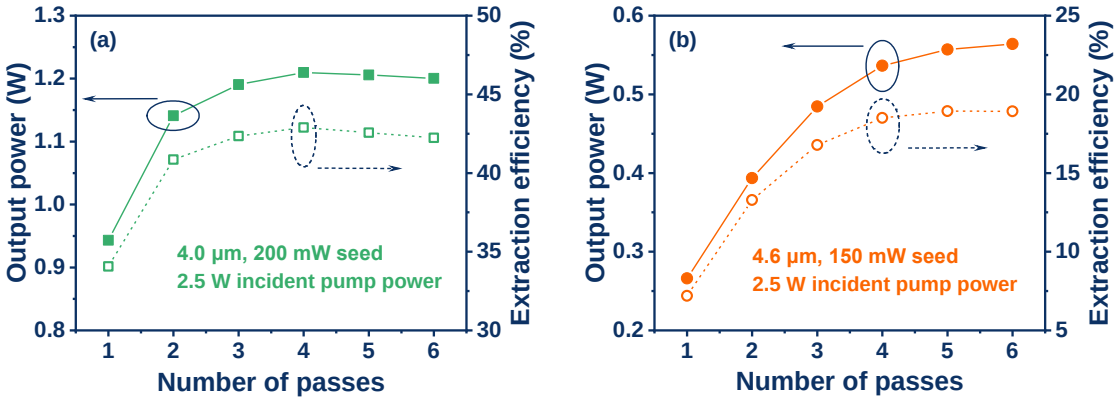

Fig. 4-14. Calculated output characteristics of the multipass Fe:ZnSe amplifier for (a) amplifying a 200-mW, 4.0-μm seed and (b) a 150-mW, 4.6-μm seed.

In this proof-of-concept study, we have demonstrated the excellent capability of Fe:ZnSe to provide broadband gain in the 4.0–4.6 μm band. The proposed Fe:ZnSe amplifier was successfully used to achieve effective power amplification of commercial FP-QCLs while well maintaining the original spectral properties and beam qualities. Additionally, we have presented a valid rate equation model applicable to the amplifier regime to provide guidance for the design of future Fe:ZnSe amplifiers.

4.3 High-power, Spectral-controlled Mid-infrared Laser

The study in this section aims at the implementation of high-power, spectral-controlled mid-infrared lasers using the hybrid Fe:ZnSe amplifier scheme. We first demonstrate a DFB-QCL seeded Fe:ZnSe amplifier capable of producing a record-high-power, pure single-frequency laser operating at 4.3 μm. Additionally, we present a widely tunable mid-infrared laser generating high-power and narrow-linewidth output with a tuning range of 630 nm, which is based on an Fe:ZnSe amplifier injection-seeded by our self-constructed EC-QCL. The prospects for further improvement in performance and extension of the tuning range are also discussed, based on theoretical calculations using the rate equation model and the existing novel designs of broadly tunable QCLs.

4.3.1 High-power, Single-frequency Laser Based on DFB-QCL/Fe:ZnSe Amplifier

(1). Experimental setup

The layout of the DFB-QCL seeded Fe:ZnSe laser amplifier is illustrated in Fig. 4-15. The DFB-QCL used was a commercially available product ordered from Hamamatsu Photonics, which could produce a maximum seed power of 55 mW with single-frequency operation at 4.3 μm. The output from the DFB-QCL was collimated using a 3-mm focal-length aspheric lens and focused into an Fe:ZnSe crystal using a 75-mm focal-length lens, yielding an elliptical beam waist radius of approximately 85 μm × 110 μm in the vertical and horizontal directions, respectively. The Fe:ZnSe single crystal (supplied by 3photon) had a relatively high doping concentration (~1×10^{19} cm^{-3}) so that the pump absorption was adequately high to provide sufficient laser gain. It was cut into a slab shape with dimensions of 2 mm × 5 mm × 2.7 mm (H × W × L). The crystal was mounted in a liquid-nitrogen-cooled copper heat sink and placed inside a vacuumed cryostat for efficient heat removal and the prevention of thermal quenching. An inhouse-built, 2920-nm Er:YAP laser (same as the one described in Section 3.2.1), producing 3.6 W of output power, served as the pump source for Fe:ZnSe. The pump laser was focused into the Fe:ZnSe crystal using a

50-mm focal-length CaF_2 lens to provide a pump spot size slightly larger than that of the signal beam.

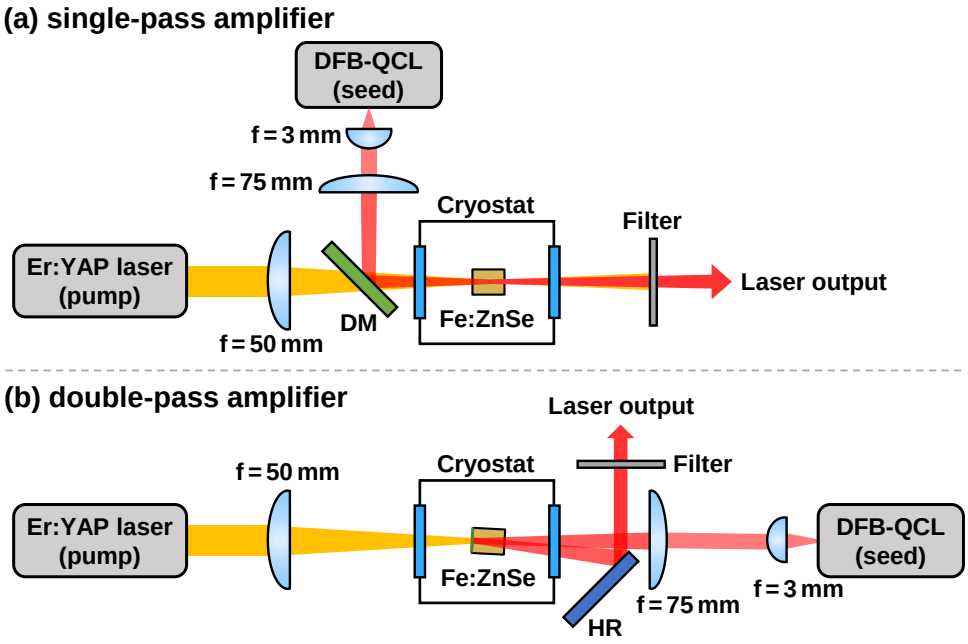

Fig. 4-15. Schematic of the DFB-QCL/Fe:ZnSe amplifier setup. (a) Single-pass amplifier. (b) Double-pass amplifier. DM, dichroic mirror; HR, high reflector.

The amplification performance was studied for the single- and double-pass configurations. For the single-pass amplifier (Fig. 4-15(a)), the Fe:ZnSe crystal was broadband antireflection-coated for 2800–5000 nm. The signal light was steered into the Fe:ZnSe amplifier using a dichroic mirror (DM), which had high reflectivity at 3800–5000 nm and high transmission at 2700–3000 nm, to propagate collinearly with the pump laser. A bandpass filter operating at 4–4.5 μm was placed behind the Fe:ZnSe amplifier to block the unabsorbed pump laser and transmit only the desired 4.3 μm laser. To obtain a higher extraction efficiency, and eventually, a higher output power, the crystal coating was specially designed to enable a double-pass configuration (see Fig. 4-15(b)). The seed-injection face of the Fe:ZnSe crystal was antireflection-coated for 2800–5000 nm, and the pumped face was dichroic-coated for high transmission at the pump wavelength of 2920 nm and high reflectivity at 3800–5000 nm, thus enabling the retroreflection of the signal light to provide a second pass through the Fe:ZnSe crystal. The crystal was slightly tilted to generate a small angle between the second pass and the initial incident beam, thereby

enabling the laser output to be steered to the power meter via a high reflector (HR).

(2). Experimental results and analysis

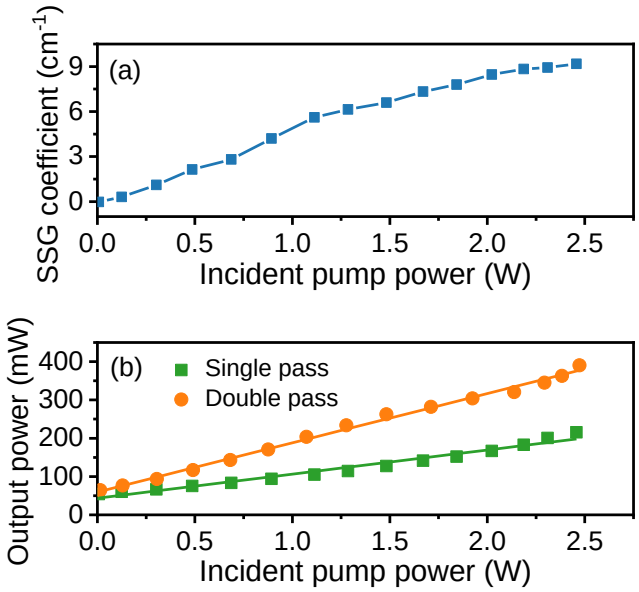

Fig. 4-16. Output characteristics of the DFB-QCL/Fe:ZnSe amplifier. (a) SSG coefficient versus incident pump power. (b) Amplifier output power versus incident pump power.

Figure 4-16 shows the output characteristics of the DFB-QCL/Fe:ZnSe amplifiers. We first measured the small-signal gain (SSG) of the Fe:ZnSe at 4.3 μm by injecting a 1-mW probe light in the single-pass configuration. The SSG coefficient as a function of incident pump power is shown in Fig. 4-16(a). It can be seen that the SSG coefficient increased almost linearly with increasing pump power when the incident pump power was below 1.5 W. For pump powers more than 1.5 W, a notable decrease in the increase rate was observed; this is attributed to the gain clamping caused by ground-state bleaching, as well as the thermal quenching induced by the high heat load at high pump power levels. At the maximum available pump power, the SSG coefficient was measured to be 9.1 cm^{-1}. Figure 4-16(b) shows the laser output power versus incident pump power for amplifiers injection-seeded with a 55-mW signal light. As there was no reabsorption loss of Fe:ZnSe at 4.3 μm, the threshold pump power for positive net gain was relatively low at < 20 mW. For the single-pass amplifier, a maximum output power of 215 mW was obtained at an incident pump power of 2.5 W, and the corresponding extraction efficiency was 7%, considering a

pump absorption of approximately 95%. For further power scaling of the amplifier, we then deployed the dichroic coating on the pumped surface of the Fe:ZnSe crystal to achieve a double-pass amplifier (see Fig. 4-15(b)). The double-pass configuration produced a maximum output power of 390 mW, which is believed to be the largest value reported thus far for a single-frequency 4.3-μm laser. Additionally, although the 4.3 μm is slightly farther from the gain peak of Fe:ZnSe [4-12], the extraction efficiency can still reach more than 14% in this experiment.

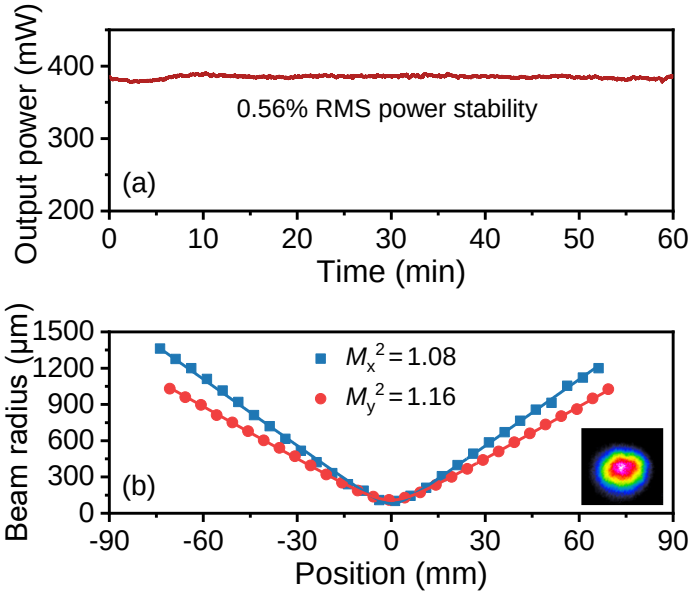

Fig. 4-17. (a) Temporal power stability and (b) laser beam quality of the DFB-QCL/Fe:ZnSe amplifier at the maximum output power.

Figure 4-17(a) shows the temporal power stability of the double-pass DFB-QCL/Fe:ZnSe amplifier recorded at the maximum power level. Good temporal stability was observed over 1 h of monitoring with an RMS power stability of approximately 0.56%. This slight power fluctuation was mainly caused by the mechanical vibrations introduced by the vacuum pump. The output from the double-pass amplifier was focused by a 75-mm focal-length CaF_2 lens, and the laser beam quality was examined using the knife-edge method. As shown in Fig. 4-17(b), the beam quality for the maximum output power was very good, with measured M^2 values of $M_x^2 < 1.1$ and $M_y^2 < 1.2$, revealing that the output was a typical TEM_{00} mode. The two-dimensional far-field beam profile (inset of Fig. 4-17(b)) confirmed the single-transverse mode of operation.

The spectral properties of the DFB-QCL/Fe:ZnSe amplifier are presented in Fig. 4-18. The fine spectral characteristics after laser amplification were analyzed using a scanning Fabry–Pérot interferometer (Thorlabs) with a free spectral range of 1.5 GHz. The laser was confirmed to be single-frequency and no mode-hopping or parasitic oscillation was observed during the amplification process. The frequency spectrum showed an FWHM linewidth of 29.6 MHz (Fig. 4-18(a)), corresponding to a linewidth in wavelength of approximately 1.9 pm. In addition, the temperature tuning of the DFB-QCL seed offers precise control of the output spectra of the hybrid amplifier. Figure 4-18(b) shows the typical tuning spectra measured using a laser spectrum analyzer (Bristol). The Fe:ZnSe amplifier can be tuned from 4322 to 4333 nm by adjusting the cooling temperature of the DFB-QCL seed from 10 to 35 ℃ and emitted >300-mW output power over the entire tuning range. This fine spectral tunability, with a range of more than 10 nm, allows a specific overlap between the laser wavelength and a molecular absorption peak; for example, the fundamental vibration frequency of HTO at 4.3 μm [4-13], which is of significant interest in environmental monitoring of nuclear fusion reactors.

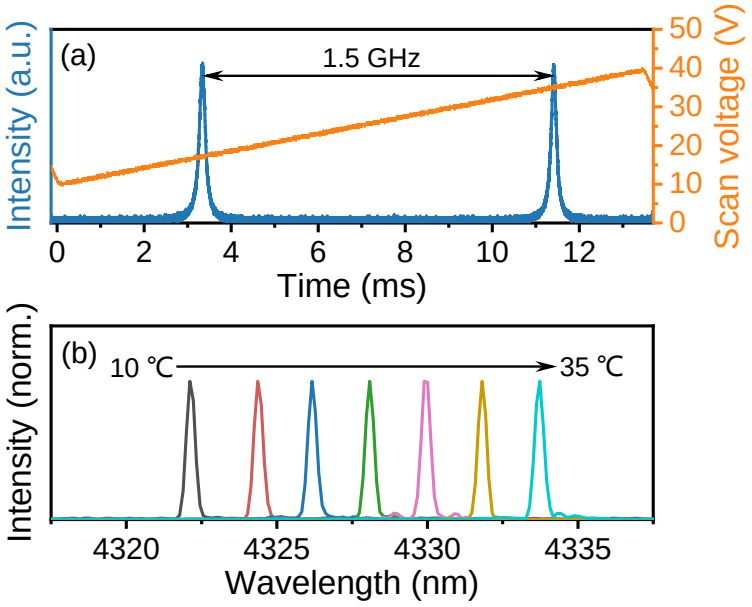

Fig. 4-18. Spectral characteristics of the DFB-QCL/Fe:ZnSe amplifier. (a) Fine spectrum examined using a scanning Fabry–Pérot interferometer. (b) Temperature tuning behavior.

(3). Theoretical analysis and discussion

Although the single-frequency laser power achieved from the Fe:ZnSe amplifier is comparable with that obtained from nonlinear devices [4-14] or QCL MOPA designs [4-15], several approaches can be used to further increase the extraction efficiency and output power. One straightforward method is to optimize the length of the Fe:ZnSe crystal to achieve the highest gain while overcoming a modest passive loss. To investigate the optimum crystal length, we calculated the amplifier output power using the theoretical model of the Fe:ZnSe amplifier presented in Section 4.2.3. Here, we slightly modified the model to make it applicable to a reverse-seeded, double-pass amplifier configuration, i.e., the same as our realistic experimental configuration shown in Fig. 4-15(b). The simplified equivalent model of this double-pass Fe:ZnSe amplifier is illustrated in Fig. 4-19. As it is a reverse-seeding structure, the boundary conditions for the calculation should be revised to:

$$I_P^+(0)=I_P^l\ ,\ I_P^-(L_c)=I_P^r\ ,\ I_L^+(0)=R_1 I_L^-(0)\ ,\ I_L^-(L_c)=I_{seed} \tag{4-4}$$

where $I_P{}^l$ and $I_P{}^r$ are the average intensities of the forward and backward pump lights, respectively; for this case, $I_P{}^r = 0$. I_{seed} is the input signal intensity; note that the seed laser propagates backward so that the boundary condition should be $I_L{}^-(L_c) = I_{seed}$. R_1 represents the reflectivity of the pumped surface of Fe:ZnSe, which was dichroic-coated to be high reflection ($R_1 \approx 97\%$) at the signal wavelength.

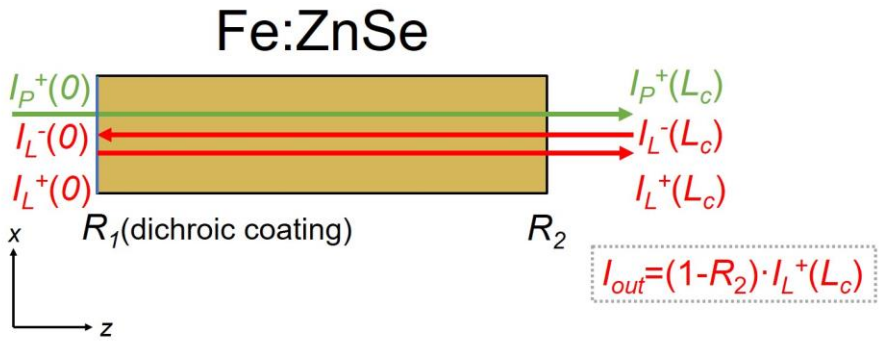

Fig. 4-19. Model of a reverse-seeded, double-pass Fe:ZnSe amplifier.

The calculation with this model uses parameters based on our experimental configuration and published spectroscopic data [4-3]. Figure 4-20 shows a typical

calculation result of the power evolution inside the Fe:ZnSe crystal for amplifying a 55-mW, 4.3-μm signal using this reverse-seeded, double-pass amplifier design. Theoretical calculations evidence that the second pass of the signal light can help to efficiently extract more energy from the Fe:ZnSe crystal.

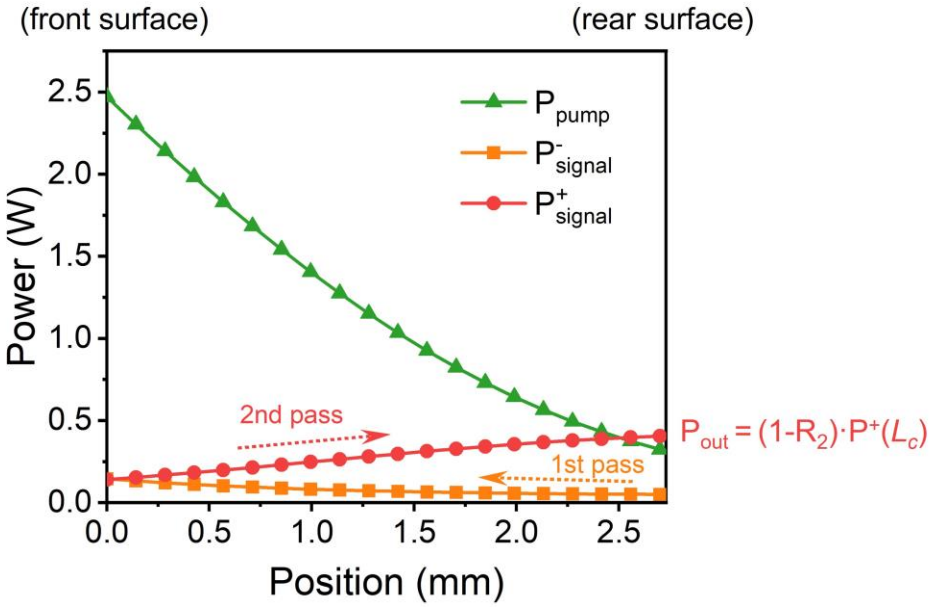

Fig. 4-20. Calculated power evolution inside the Fe:ZnSe crystal for amplifying a 55-mW, 4.3-μm signal using a reverse-seeded, double-pass amplifier.

The amplifier output power can be evaluated based on the calculated forward laser intensity at the rear surface of Fe:ZnSe. Figure 4-21(a) shows the predicted output power as a function of the crystal length for the double-pass amplifier at the maximum available pump power. The results indicate that crystal lengths in the range of 4–5 mm are optimal, with output power levels in excess of 455 mW for 2.5 W of incident pump power. A shorter crystal length causes insufficient gain owing to the significant bleaching of the ground state at high pump powers, whereas a considerably longer crystal length results in a larger intrinsic loss that can compensate for the increase in absorption efficiency, thus decreasing the amplification performance.

Another effective method for improving the extraction efficiency is to further increase the number of passes through the amplifier by guiding the beams to traverse the gain medium at slightly different angles at each pass. The rate equations used to describe the

multipass arrangements were iteratively solved, and the predicted output power versus the number of passes was numerically calculated, as shown in Fig. 4-21(b). The experimental results are also displayed (star symbols) for comparison. The good agreement between the predicted values and the experimental data confirmed the validity of the model. Our calculations indicate that increasing the number of passes can effectively increase the output power of the amplifier, and a six-pass amplifier can generate a maximum output power of 630 mW for amplifying a 55-mW signal at 2.5-W incident pump power, corresponding to an overall gain of 11.5. It should be noted that after four passes through the amplifier, further increasing the number of passes to a five- or six-pass configuration does not lead to significant power improvements because of gain saturation effects resulting from the considerable depletion of extractable energy by the driving signal. However, in this study, the implementation of a multipass (>3 passes) amplifier while maintaining good mode-matching for each pass is difficult, primarily because of the large space occupied by the cryostat. Considerably higher output powers can be expected by using longer Fe:ZnSe crystals and by implementing a multipass arrangement with a specially designed space-reduced cryostat.

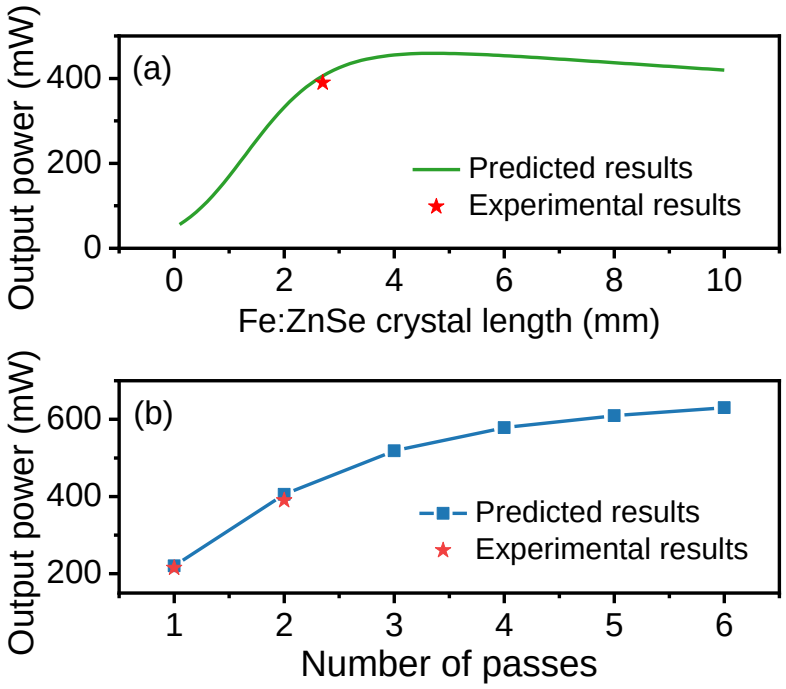

Fig. 4-21. Predicted amplifier output power (a) as a function of crystal length and (b) as a function of number of passes. The experimental results are also shown for comparison.

4.3.2 Widely Tunable, Narrow-linewidth Laser Based on EC-QCL/Fe:ZnSe Amplifier

The above results demonstrate that the DFB-QCL/Fe:ZnSe amplifier is well suited for achieving high-power, mode-hop-free single-frequency mid-infrared laser, but its main disadvantage is the limited tuning capability owing to the strong wavelength confinement introduced by the integrated grating. A laser system with a much wider tuning range would be versatile and preferable in spectroscopy applications, as it would allow high-sensitivity detections of multiple gas molecules with the use of only one light source. Moreover, there is substantial scope to extend the tuning range because the Fe:ZnSe possesses a significantly broad emission band and is therefore theoretically capable of providing laser gain in the 3.7–5.2 μm range.

To further improve the tuning ability of our system, we then modified the amplifier setup by building an EC-QCL as the input signal, aiming to achieve widely tunable and high-power laser outputs in the 4-μm spectral band. Figure 4-22 shows the photograph of our inhouse-built EC-QCL, which was deliberately designed based on a Littman-Metcalf configuration [4-16] for good laser pointing behavior and narrow spectral linewidth. Compared to the commonly used Littrow-type external cavity, one round-trip laser oscillation in a Littman-Metcalf cavity undergoes two diffraction processes such that the spectral linewidth of its output laser can be narrower.

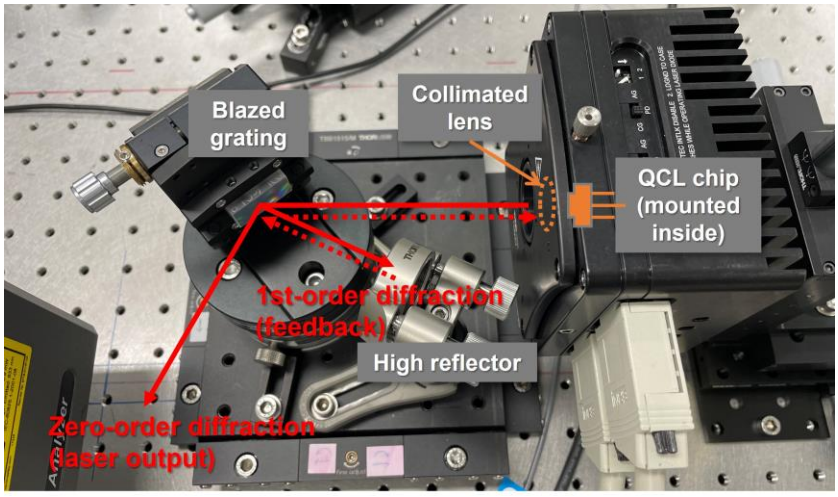

Fig. 4-22. Photograph of our inhouse-built EC-QCL seed.

Figure 4-23 depicts the experimental arrangement of the entire EC-QCL/Fe:ZnSe amplifier system. For the EC-QCL seed, two QCL chips (ordered from Thorlabs) with electroluminescence spectral peaks of 4 μm and 4.6 μm were used as the gain medium. An external diffraction grating blazed at 3.5 μm with 300 lines/mm in conjunction with a high reflector provided a wavelength selective tunable feedback (1st-order diffraction) via an aspheric lens with a 3-mm focal length. The laser output was the 0th-order reflection from the diffraction grating and was focused into the Fe:ZnSe crystal by a 75-mm focal-length lens. The Fe:ZnSe amplifier section was maintained the same single-pass arrangement as the one described in Fig. 4-6.

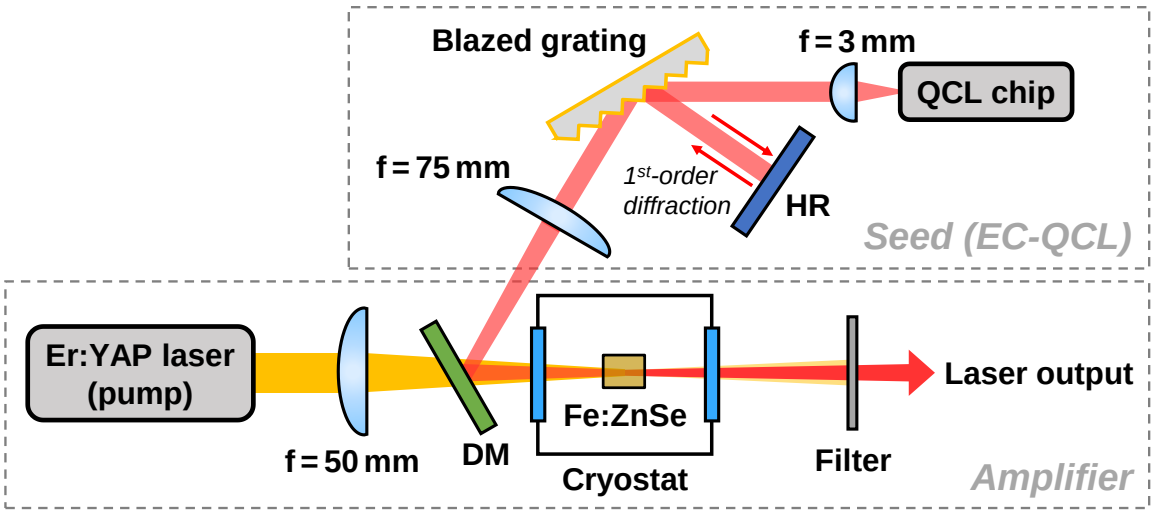

Fig. 4-23. Schematic diagram of the EC-QCL/Fe:ZnSe amplifier setup. DM, dichroic mirror; HR, high reflector.

Wavelength tuning was achieved through the rotation of the high reflector (HR in Fig. 4-23). The EC-QCL seed could be tuned over a wavelength range of ~630 nm, from 3850 to 4110 nm when using the 4-μm chip, and from 4420 to 4790 nm when using the 4.6-μm chip, with output powers in the range 1–20 mW depending on the operating wavelength. Figures 4-24 and 4-25 show the coarse tuning ability of the EC-QCL seeds based on the 4.0-μm chip and 4.6-μm chip, respectively. Outside these tuning ranges, parasitic oscillations were observed because the chip Fabry–Pérot modes would dominate the mode competition with the external-cavity modes at the gain edge wavelengths of the QCL chips.

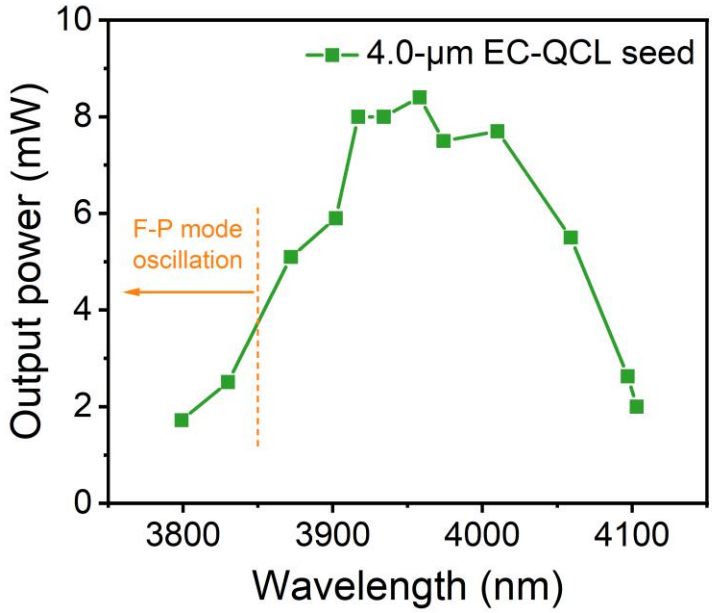

Fig. 4-24. Tuning behavior of the EC-QCL seed based on the 4.0-μm chip.

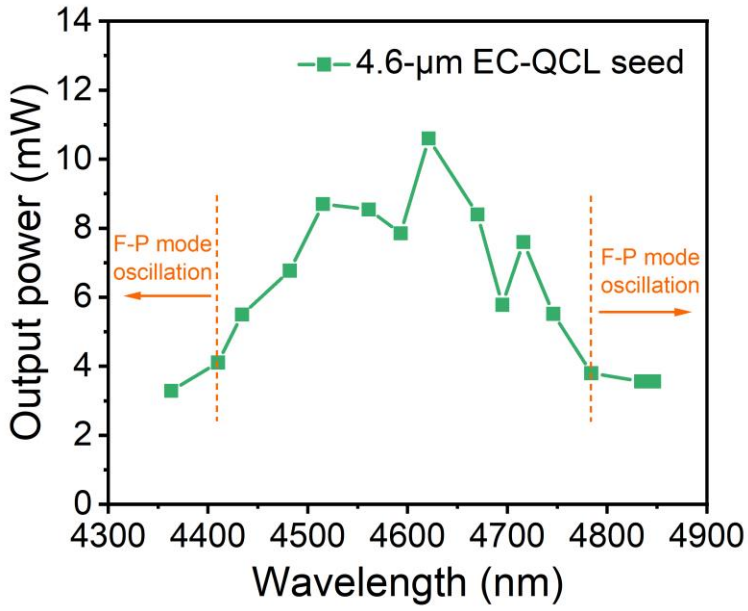

Fig. 4-25. Tuning behavior of the EC-QCL seed based on the 4.6-μm chip.

Benefiting from the broadband gain characteristics of Fe:ZnSe, the signal lasers can be effectively amplified over the entire tuning range. Figure 4-26 shows the tuning behavior of the EC-QCL/Fe:ZnSe amplifiers with their corresponding output power. For amplifying

the EC-QCL based on the 4-μm chip, the output power was more than 177 mW over a tuning range of 260 nm from 3850 to 4110 nm, and the maximum output power was 270 mW at 4015 nm (see Fig. 4-26(a)). For amplifying the EC-QCL with the 4.6-μm chip, the output power was more than 13 mW over a tuning range of 370 nm from 4420 to 4790 nm, and the maximum output power was 23 mW at 4620 nm (see Fig. 4-26(b)). The corresponding extraction efficiencies were nearly 10% and < 1% for amplification in the shorter and longer wavelength regions, respectively. The low output power and efficiency for the longer wavelength region were due primarily to the small emission cross section of Fe:ZnSe at 4.4–5 μm [4-3]. Likewise, a multipass arrangement is necessary to improve the energy extraction and hence amplifier output power. The linewidth of the output beam remained approximately constant over the whole tuning range and was confirmed to be less than 0.3 nm everywhere.

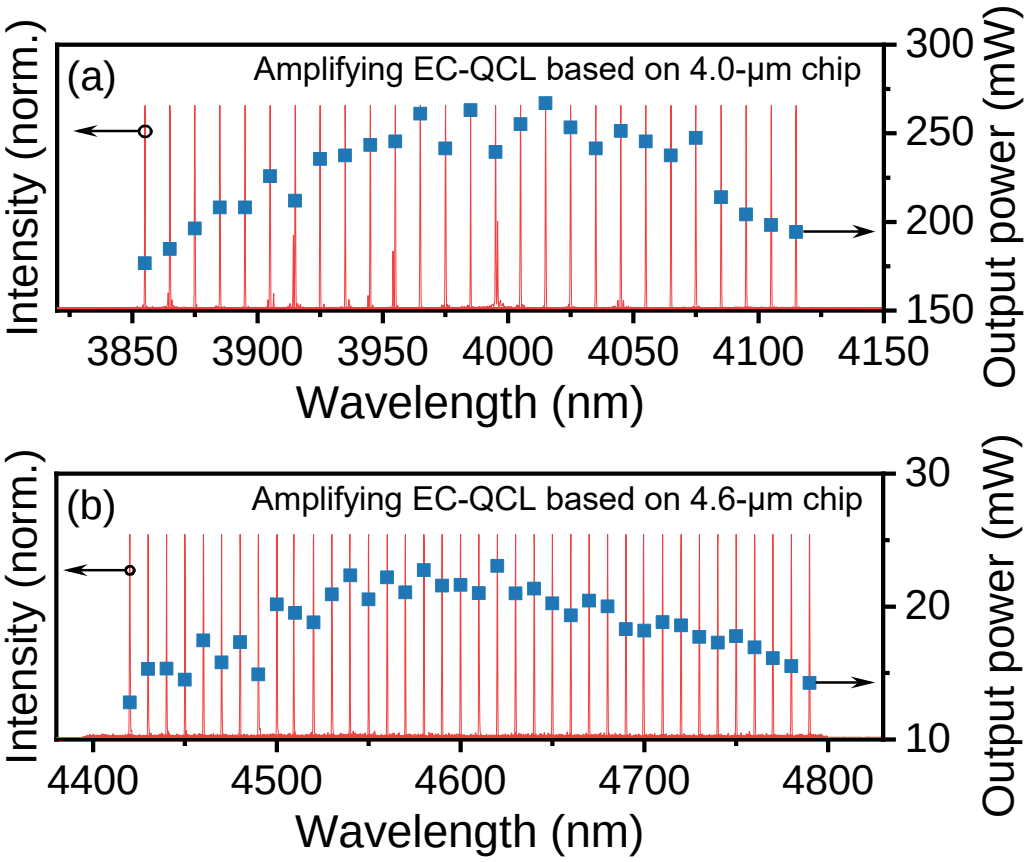

Fig. 4-26. Tuning behavior of the Fe:ZnSe amplifier injection-seeded by EC-QCLs based on (a) 4-μm chip and (b) 4.6-μm chip.

Although the tuning range demonstrated above is already large, the accessible wavelength range may also be further extended by using AR-coated chips as the gain medium of EC-QCL. Due to the absence of AR coating on the emitting facet of the chip we used, lasing of parasitic Fabry–Pérot modes occurred when tuning the wavelength beyond these two regions. By depositing an AR coating on the QCL chips, it is possible to increase the relative losses of the Fabry–Pérot modes compared to the losses of the EC modes, such that the parasitic Fabry–Pérot oscillations can be effectively suppressed, and a wider tuning range can be expected. In addition, tailoring the luminescence spectrum of the gain chip in an EC-QCL using a bound-to-continuum design [4-17] is another interesting approach that can specifically overlap with the emission spectrum of Fe:ZnSe and enable a tuning range beyond 1000 nm. Future work will be focused on the implementation of a high-power, single-frequency mid-infrared laser with a much broader tuning range using this hybrid Fe:ZnSe amplifier scheme.

4.4 Conclusions and Outlook

In conclusion, the study in this chapter presents a new path to achieve a high-power, spectra-controlled mid-infrared laser, which is based on a hybrid Fe:ZnSe amplifier scheme. First, a preliminary proof-of-concept experiment was conducted, demonstrating that the Fe:ZnSe amplifier can provide efficient power amplification in the 4.0–4.6 μm band. A maximum output power of 870 mW with an extraction efficiency of 30% was achieved from an Fe:ZnSe amplifier seeded by a 200-mW laser at 4.0 μm, corresponding to a gain of approximately 4.4. When the amplifier was seeded by a 150-mW laser at 4.6 μm, an effective gain of approximately 1.4 was obtained. Additionally, a modified rate equation model that is applicable to the Fe:ZnSe amplifier regime was proposed to predict the optimized amplifier performance.

Further, this hybrid Fe:ZnSe amplifier scheme was applied to demonstrate high-power, narrow-linewidth and widely tunable mid-infrared lasers. We have demonstrated a high-power, pure single-frequency laser operating at 4.3 μm, based on a DFB-QCL seeded Fe:ZnSe amplifier scheme. A maximum output power of 390 mW was produced with an extraction efficiency of approximately 14% and a spectral linewidth of 29.6 MHz from a

compact double-pass amplifier design, which is to the best of our knowledge, the highest output power reported thus far for a 4.3-μm single-frequency laser. Theoretical calculations show that a further increase in the extracted output power can be achieved using a slightly longer Fe:ZnSe crystal or by employing a multipass amplifier arrangement. This study opens a new avenue for the development of MIR lasers with a high power spectral density using Fe:ZnSe.

Furthermore, a widely tunable and narrow-linewidth laser was successfully constructed based on an Fe:ZnSe amplifier seeded by a self-constructed EC-QCL, producing output powers in the order of tens or hundreds of milliwatts in the 3.8–4.8 spectral region. The numerous wavelength options across the 630 nm tuning band and the narrow spectral linewidth of less than 0.3 nm can meet the requirements of high-sensitivity spectroscopy applications and are therefore well suited for real-time, in-situ detection of HTO isotopes in nuclear fusion reactors. Besides that, they are also of significant interest for diverse applications such as breath analysis and nonmetallic laser processing.

References (Chapter IV)

[4-1]. E. Li, H. Uehara, W. Yao, S. Tokita, F. Potemkin, R. Yasuhara, "High-efficiency, continuous-wave Fe:ZnSe mid-IR laser end pumped by an Er:YAP laser," Optics Express, **29**(26), 44118–44128 (2021).

[4-2]. A. V. Pushkin, E. A. Migal, H. Uehara, K. Goya, S. Tokita, M. P. Frolov, Y. V. Korostelin, V. I. Kozlovsky, Y. K. Skasyrsky, and F. V. Potemkin, "Compact, highly efficient, 2.1 W continuous-wave mid-infrared Fe:ZnSe coherent source, pumped by an Er:ZBLAN fiber laser," Optics Letters, **43**(24), 5941–5944 (2018).

[4-3]. J. W. Evans, R. W. Stites, and T. R. Harris, "Increasing the performance of an Fe:ZnSe laser using a hot isostatic press," Optical Materials Express, **7**(12), 4296–4303 (2017).

[4-4]. W. Koechner, "Solid-state laser engineering," Chapter 5, Springer, 2013.

[4-5]. M. E. Doroshenko, H. Jelínková, P. Koranda, J. Šulc , T. T. Basiev, V. V. Osiko, V. K. Komar, A. S. Gerasimenko, V. M. Puzikov, V. V. Badikov, and D. V. Badikov, "Tunable mid-infrared laser properties of Cr^{2+}:ZnMgSe and Fe^{2+}:ZnSe crystals," Laser Physics Letters, **7**, 38–45 (2010).

[4-6]. J. W. Evans, P. A. Berry, and K. L. Schepler, "A broadly tunable continuous-wave Fe:ZnSe laser," Proc. SPIE **8599**, 85990C (2013).

[4-7]. A. V. Pushkin, E. A. Migal, H. Uehara, K. Goya, S. Tokita, M. P. Frolov, Y. V. Korostelin, V. I. Kozlovsky, Y. K. Skasyrsky, and F. V. Potemkin, "Directly fiber-pumped mid-IR Fe:ZnSe CW laser tunable from 3.8 up to 5.1 μm," in Laser Congress 2019 (ASSL, LAC, LS&C), OSA Technical Digest (Optica Publishing Group, 2019), paper ATu4A.6.

[4-8]. A. Hugi, R. Maulini, and J. Faist, "External cavity quantum cascade laser," Semiconductor Science and Technology, **25**(8), 083001 (2010).

[4-9]. V. I. Kozlovsky, V. A. Akimov, M. P. Frolov, Yu. V. Korostelin, A. I. Landman, V. P. Martovitsky, V. V. Mislavskii, Yu. P. Podmar'kov, Ya. K. Skasyrsky, and A. A. Voronov, "Room-temperature tunable mid-infrared lasers on transition-metal

doped II–VI compound crystals grown from vapor phase," Physica Status Solidi (b), **247**(6), 1553–1556 2010.

[4-10]. W. Koechner, "Solid-state laser engineering," Chapter 3, Springer, 2013.

[4-11]. W. Koechner, "Solid-state laser engineering," Chapter 4, Springer, 2013.

[4-12]. J. W. Evans, T. R. Harris, B. R. Reddy, K. L. Schepler, and P. A. Berry, "Optical spectroscopy and modeling of Fe^{2+} ions in zinc selenide," Journal of Luminescence, **188**, 541–550 (2017).

[4-13]. M. J. Down, J. Tennyson, M. Hara, Y. Hatano, and K. Kobayashi, "Analysis of a tritium enhanced water spectrum between 7200 and 7245 cm^{-1} using new variational calculations," Journal of Molecular Spectroscopy, **289**, 35–40 (2013).

[4-14]. M. K. Shukla and R. Das, "High-Power Single-Frequency Source in the Mid-Infrared Using a Singly Resonant Optical Parametric Oscillator Pumped by Yb-Fiber Laser," IEEE Journal of Selected Topics in Quantum Electronics, **24**(5), 1–6 (2018).

[4-15]. M. Bertrand, A. Shlykov, M. Shahmohamadi, M. Beck, S. Willitsch, and J. Faist, "High-Power, Narrow-Linewidth Distributed-Feedback Quantum Cascade Laser for Molecular Spectroscopy," Photonics, **9**(8), 589 (2022).

[4-16]. M. G. Littman, and H. J. Metcalf, "Spectrally narrow pulsed dye laser without beam expander," Applied Optics, **17**(14), 2224–2227 (1978).

[4-17]. J. Faist, M. Beck, T. Aellen, and E. Gini, "Quantum-cascade lasers based on a bound-to-continuum transition," Applied Physics Letters, **78**(2), 147–149 (2001).

V. Preliminary Study on Water Isotope Detection Using Mid-infrared Laser

In addition to laser developments, we conducted a preliminary study on water isotope detection using mid-infrared lasers. The main purpose of this study is to develop a portable and in-situ usable system for spectroscopic measurement with a simple and compact structure. Thus, we employed a conventional "light → sample → detector" architecture [5-1] for the system design.

One necessary step in isotope analysis is to identify and calibrate a specific absorption peak of the target molecule. Although it is possible to simulate the absorption spectrum of a molecule using the HITRAN database [5-2], the absorption characteristics of molecules could be influenced by environmental factors, such as temperature, pressure, or humidity, resulting in shifts in line position or changes in linewidth. Thus, calibration is essential for the characterization and correction of these effects, ensuring that the observed absorption lines are not falsely attributed to the molecule of interest.

In this work, we present a compact detection system for gaseous water isotopes. The absorption peaks at 6.3 μm and 7.4 μm were calibrated for three isotope samples (H_2O, HDO, and $H_2{}^{18}O$). Finally, we introduce the preparations of a long-optical-path architecture using a multipass gas cell for weak-trace-gas absorption spectroscopy applications.

5.1 Experimental Setup for Water Isotope Detection

In these preliminary experiments, we used two commercially ordered DFB-QCLs operating at 6.3 μm and 7.4 μm as the detection light source instead of our self-developed 3–5 μm lasers described in the above sections. This is because the 6–7 μm band can avoid atmospheric CO_2 absorption, which is strongest near the 4 μm band [5-3]. In addition, the 6–7 μm band corresponds to the second strongest absorption band of water isotopes (see Fig. 1-8), thus also enabling the measurement of low-concentration samples. As we did not deploy a pure gas circulator [5-4] to exclude the influence of atmospheric CO_2 and water

vapor in this preliminary experiment, using a 6–7 μm laser is a much simpler and more practical option for the measurements.

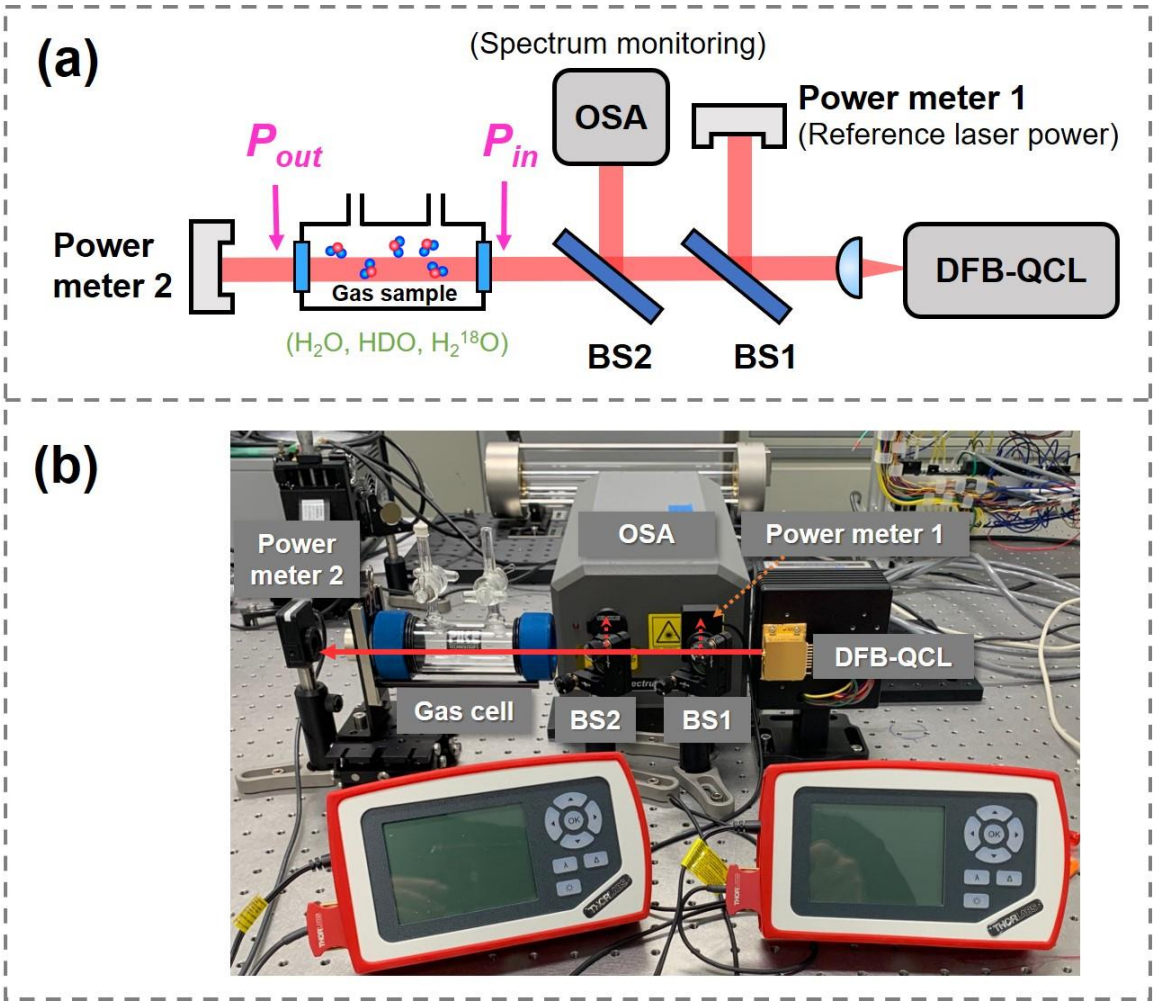

Fig. 5-1. (a) Schematic diagram and (b) photograph of the isotope detection setup. BS: beam splitter; OSA: optical spectrum analyzer.

Figure 5-1 shows the schematic diagram and the photograph of the isotope detection setup, which was constructed based on a conventional "light source → sample → detector" scheme. Two single-frequency DFB-QCLs operating at 6.3 μm and 7.4 μm were employed as the light source, the wavelength of which can be precisely tuned by controlling the driving current in conjunction with the operating temperature of the QCL chips. Figures 5-2 and 5-3 show the laser output power and central wavelength as functions of the input current for the 6.3-μm and 7.4-μm QCLs, respectively. The 6.3-μm QCL can produce a maximum output power of 32 mW at a cooling temperate of 10 ℃. The laser wavelength

can be precisely tuned with a range of 13.4 nm, from 6252.6 nm to 6266.0 nm. The 7.4-μm QCL can emit a stronger laser radiation, with a maximum output power of 55 mW. With a larger range of adjustable currents, the tuning range of the 7.4-μm QCL is also broader, with an overall tuning range of nearly 22 nm, from 7363.6 nm to 7385.4 nm. Both QCLs can keep single-frequency operation over the entire tuning range, according to the information provided by the vendor.

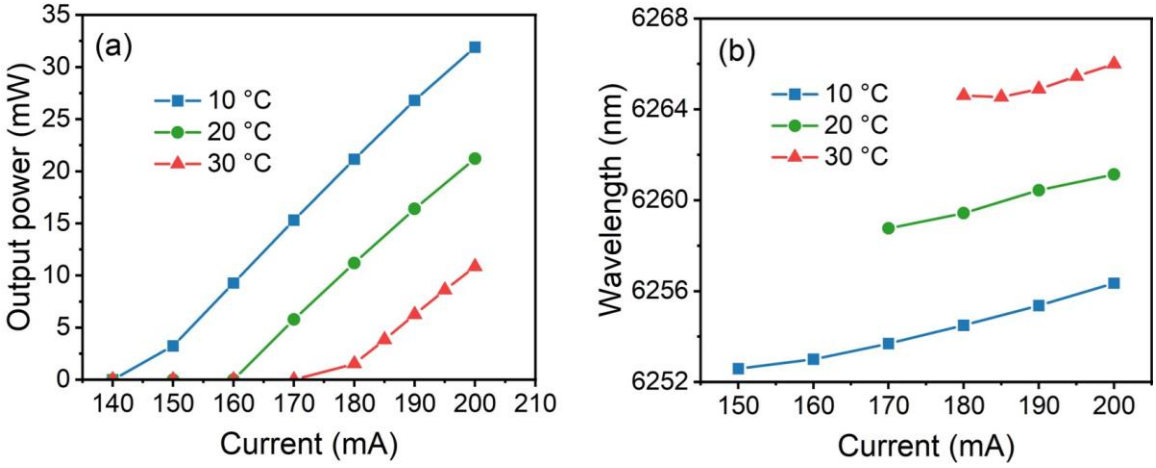

Fig. 5-2. Output characteristics of the 6.3-μm QCL. (a) Output power versus driving current. (b) Central wavelength versus driving current.

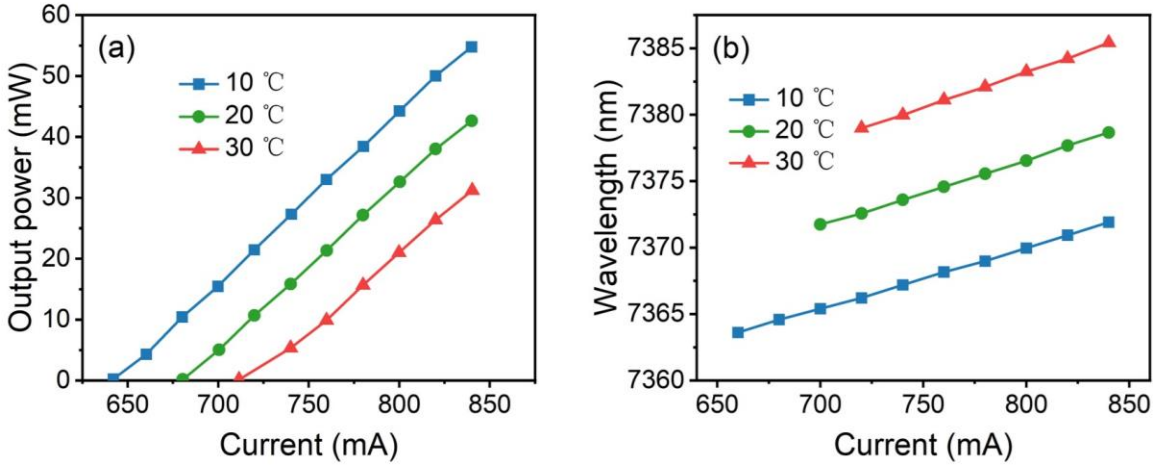

Fig. 5-3. Output characteristics of the 7.4-μm QCL. (a) Output power versus driving current. (b) Central wavelength versus driving current.

The output from the DFB-QCL was collimated using an aspheric ZnSe lens with a focal length of 4.8 mm to a beam radius of approximately 2 mm. Two plate beam splitters (BS1 and BS2 in Fig. 5-1), which were optimized for 50:50 beamsplitting at a 45° angle of incidence, were placed behind the DFB-QCL in sequence to reflect parts of the laser energy for monitoring the reference laser power and laser spectrum simultaneously. The laser transmitting through these two beam splitters was passing through the gas cell and absorbed by the internal gas molecules. The gas sample to be measured was sealed in a 10-cm long gas cell with a pressure of approximately 5 Torr. The two windows of the gas cell were made of uncoated CaF_2, which could provide more than 90% transmission at both wavelength bands. In this preliminary study, we used two high-resolution thermal power sensors to measure the laser powers. Although the response of the thermal sensor is not fast enough, it can provide sufficient measurement accuracy when the laser source is sufficiently stable and powerful. Additionally, an optical spectrum analyzer (OSA in Fig. 5-1) was used to monitor the laser wavelength simultaneously.

5.2 Measurement Results

In the experiment, we designed a LABVIEW program to help collect the experimental data. Figure 5-4 shows the main page of the LABVIEW program. The central wavelength of the DFB-QCL was precisely tuned by adjusting the driving current with a sweeping step of 0.02 mA. At each current value, the laser powers measured by the power meters 1 and 2 and the laser wavelength measured by the OSA were recorded simultaneously. To evaluate the power absorbed by the gas sample, two measurements were performed with and without the sample (vacuumized gas cell). Figure 5-5 shows a typical result of laser powers recorded behind the gas cell when measuring HDO isotopes using the 6.3-μm QCL. Note that the measured laser power under conditions without the gas sample (blue curve in Fig. 5-5) is supposed to increase linearly with input current; however, a reduction in slope efficiency was observed in the current range of 170–180 mA and 190–200 mA. This phenomenon can be attributed to the absorption caused by other gas molecules in the atmosphere. Even though, two absorption peaks of HDO can still be clearly observed. The concentration of HDO in the gas cell can

be thus derived by comparing the difference in measured power with and without the sample.

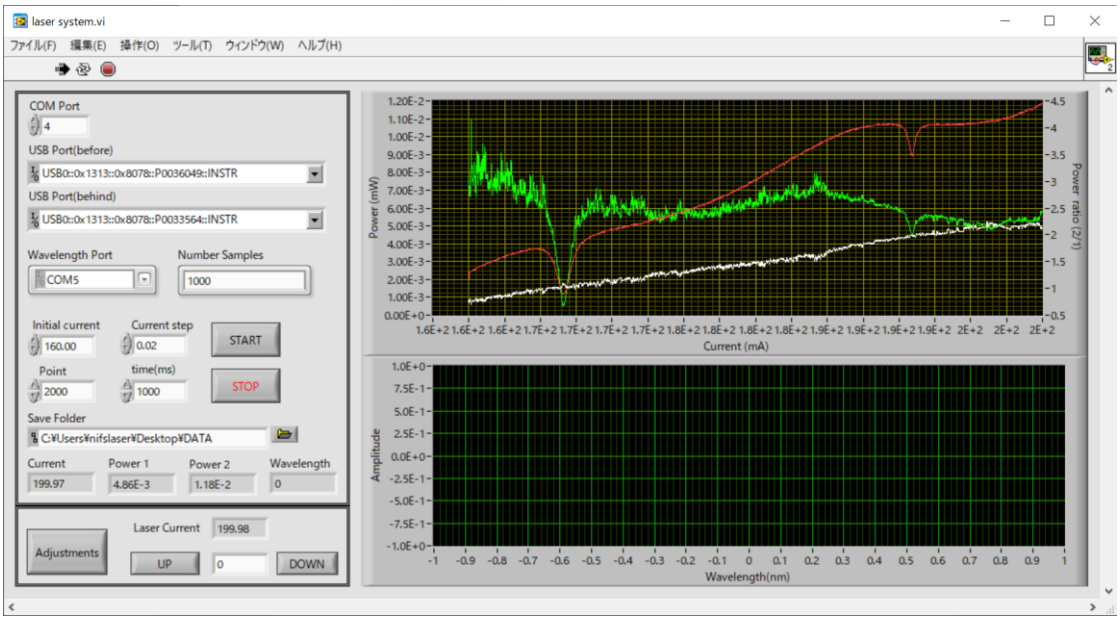

Fig. 5-4. LABVIEW program for data collection.

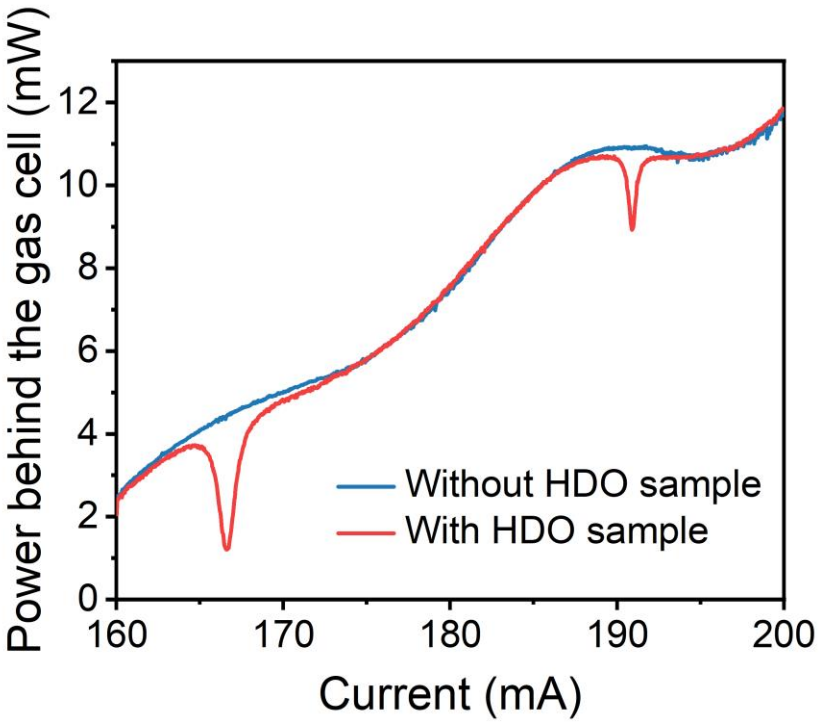

Fig. 5-5. Typical results of measuring HDO isotopes using the 6.3-μm QCL.

The transmittance of the gas sample can be calculated by the ratio of the power measured in the presence of the gas sample to the power measured with a vacuum cell. We measured the transmission spectra of pure water (H_2O), heavy water (HDO), and heavy-oxygen water ($H_2{}^{18}O$) using the 6.3-μm and 7.4-μm DFB-QCLs, respectively. Figure 5-6 summarizes the measurement results when using the 6.3-μm QCL. Two absorption peaks of HDO (orange dashed line) and one absorption peak of $H_2{}^{18}O$ (blue solid line) were identified in the tuning range of the 6.3-μm QCL. Additionally, pure H_2O also presented a weak absorption peak around 6255 nm (green dotted line). The close proximity of this absorption line to the strong absorption peak of HDO suggests that the HDO detection could be affected by atmospheric water vapor, which may interfere with the accuracy of the measurement results. Therefore, it is preferable to tune the laser wavelength to the absorption line at 6257 nm for the measurement of HDO.

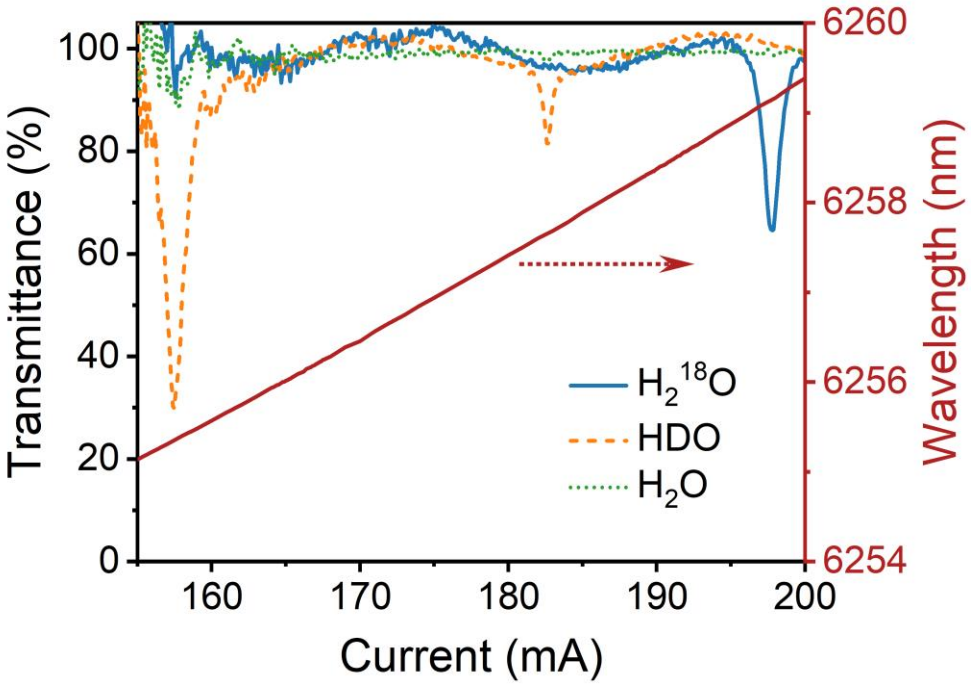

Fig. 5-6. Transmittance spectra of water isotopes measured using the 6.3-μm QCL.

These experimentally measured absorption peaks were carefully compared with simulated results from the HITRAN database [5-2], as shown in Table 5-1. There is a slight

difference between the experimental and simulated results, which can be attributed to the influence of environmental factors [5-5]. With this measurement, we have successfully calibrated the accurate absorption peaks of water isotopes in the 6.3-μm band, which is instrumental for the subsequent trace isotope analysis.

Table 5-1. Comparison of measurement results with HITRAN database for absorption lines at the 6.3-μm band.

Water isotope	**HITRAN data [5-2]**	**Measured data**
H_2O	1598.26 cm^{-1} (6256.79 nm)	1598.62 cm^{-1} (6255.39 nm)
HDO	1598.45 cm^{-1} (6256.07 nm)	1598.63 cm^{-1} (6255.34 nm)
HDO	1597.86 cm^{-1} (6258.38 nm)	1598.04 cm^{-1} (6257.66 nm)
$H_2{}^{18}O$	1597.48 cm^{-1} (6259.86 nm)	1597.66 cm^{-1} (6259.14 nm)

Figure 5-7 shows the transmittance spectra measured using the 7.4-μm QCL. The absorption peaks of all three water isotopes in this wavelength band were successfully calibrated. Two major absorption peaks of $H_2{}^{18}O$ and four major absorption peaks of HDO can be observed. Moreover, we found that the absorption peaks of pure H_2O almost overlap with those of HDO at longer wavelengths (7373–7377 nm), indicating that these absorption peaks may be caused by the stretching vibration of the hydroxyl group, which is present in both molecules. No absorption lines of H_2O were observed at wavelengths shorter than 7373 nm, thus suggesting that a short laser wavelength can effectively circumvent the interference from the atmospheric vapor absorption when measuring HDO or $H_2{}^{18}O$ samples.

Likewise, we compared the experimentally measured absorption lines with simulated results from the HITRAN database, as summarized in Table 5-2. It can be seen that the experimental results coincide well with the simulated results for HDO and $H_2{}^{18}O$. However, there is a relatively large difference of approximately 1–2 nm in the experimental and simulated results of H_2O. The reason for this large discrepancy is yet unknown, but we are certain that the environmental factor must be one of the influences.

Based on these calibrated transmission spectra, interference-free detection of individual samples can be conducted by tuning the laser to a distinguishable wavelength, hence

enabling accurate calculation of the gas concentration. Future work will be focused on the measurement of trace amounts of gaseous isotopes using a specific strong absorption line and on the verification of the feasibility for interference-free in-situ measurements.

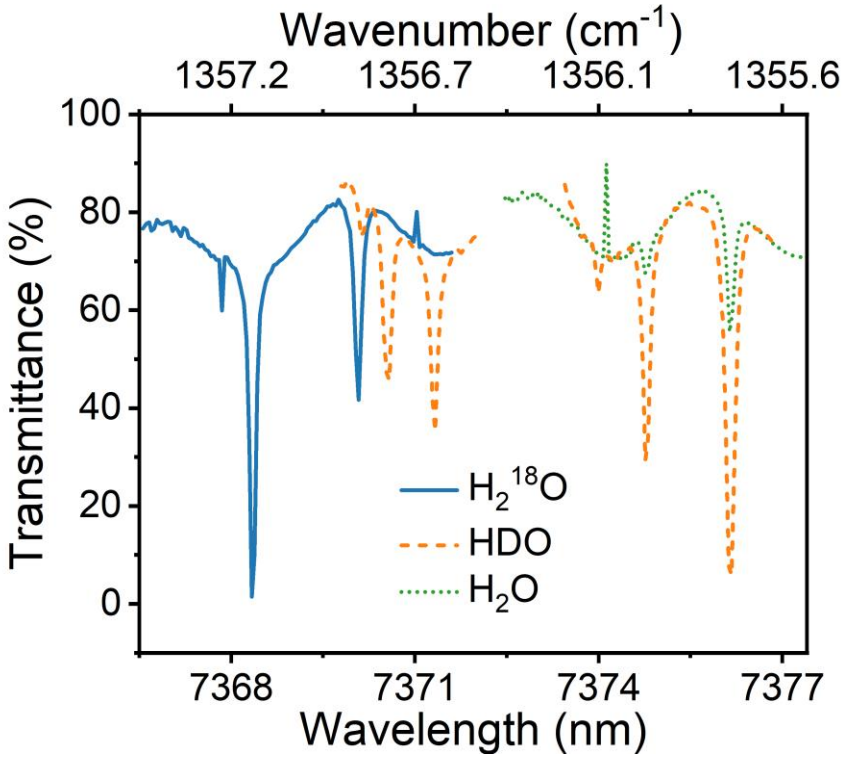

Fig. 5-7. Transmittance spectra of water isotopes measured using the 7.4-μm QCL.

Table 5-2. Comparison of measurement results with HITRAN database for absorption lines at the 7.4-μm band.

Water isotope	**HITRAN data [5-2]**	**Measured data**
H_2O	1356.16 cm^{-1} (7373.76 nm)	1355.98 cm^{-1} (7374.76 nm)
H_2O	1356.04 cm^{-1} (7374.41 nm)	1355.72 cm^{-1} (7376.14 nm)
HDO	1356.77 cm^{-1} (7370.45 nm)	1356.74 cm^{-1} (7370.58 nm)
HDO	1356.76 cm^{-1} (7370.50 nm)	degenerate in 7370.58 nm
HDO	1356.63 cm^{-1} (7371.21 nm)	1356.61 cm^{-1} (7371.33 nm)
HDO	1355.99 cm^{-1} (7374.69 nm)	1355.98 cm^{-1} (7374.76 nm)
HDO	1355.74 cm^{-1} (7376.05 nm)	1355.72 cm^{-1} (7376.17 nm)
$H_2{}^{18}O$	1357.16 cm^{-1} (7368.33 nm)	1357.16 cm^{-1} (7368.33 nm)
$H_2{}^{18}O$	1356.84 cm^{-1} (7370.07 nm)	1356.84 cm^{-1} (7370.08 nm)

5.3 Conclusions and Outlook

In conclusion, the study in this chapter presents our preliminary study on water isotope detection using mid-infrared lasers. We have constructed a laser absorption spectroscopy system based on the "light → sample → detector" design. The absorption peaks of three water isotopes (H_2O, HDO, and $H_2{}^{18}O$) were successfully calibrated using two single-frequency DFB-QCLs operating at 6.3 μm and 7.4 μm as light sources. The experimental results verify the usability of our detection system. Additionally, it is worth noting that the compact size of our proposed system, which has a footprint of about 20 cm × 20 cm, makes it easily portable and thus can be applied to real-time, in-situ measurements. This study also lays a solid foundation for the subsequent detection of lower-concentration isotopes using more advanced spectroscopy techniques.

In future studies, high-sensitivity water isotope detection can be expected by using absorption enhancement techniques in combination with high-performance mid-infrared laser sources. One of the simplest ways is to use a multipass gas cell with two high reflectors at either ends of the cell to allow multiple internal reflections of the laser, thereby increasing the optical path length of the laser-sample interaction. We have already designed and preliminarily built a multipass spectroscopy system based on a Herriott-type gas cell, as shown in Fig. 5-8. Additionally, a high-finesse optical cavity designed for cavity ring-down spectroscopy has been manufactured, as shown in Fig. 5-9. Validation experiments for ultra-sensitive isotope detection using these advanced gas cells are in progress.

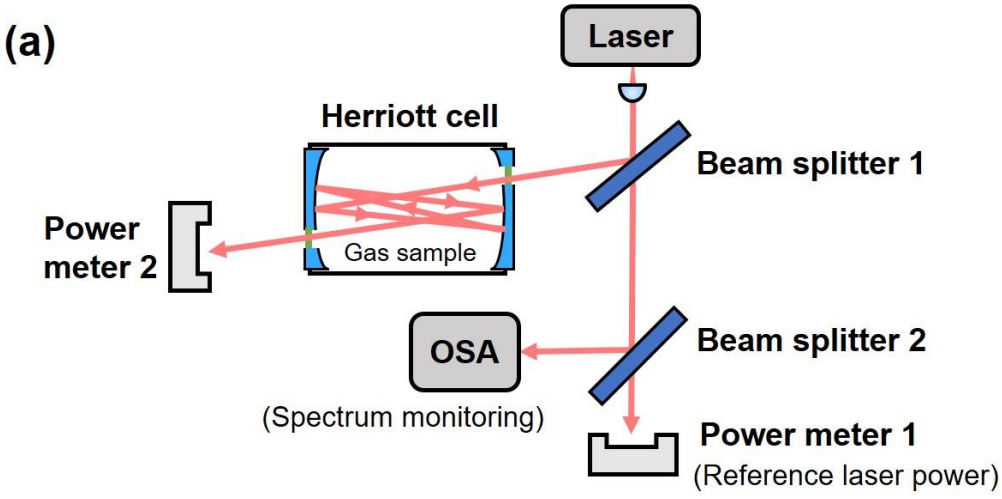

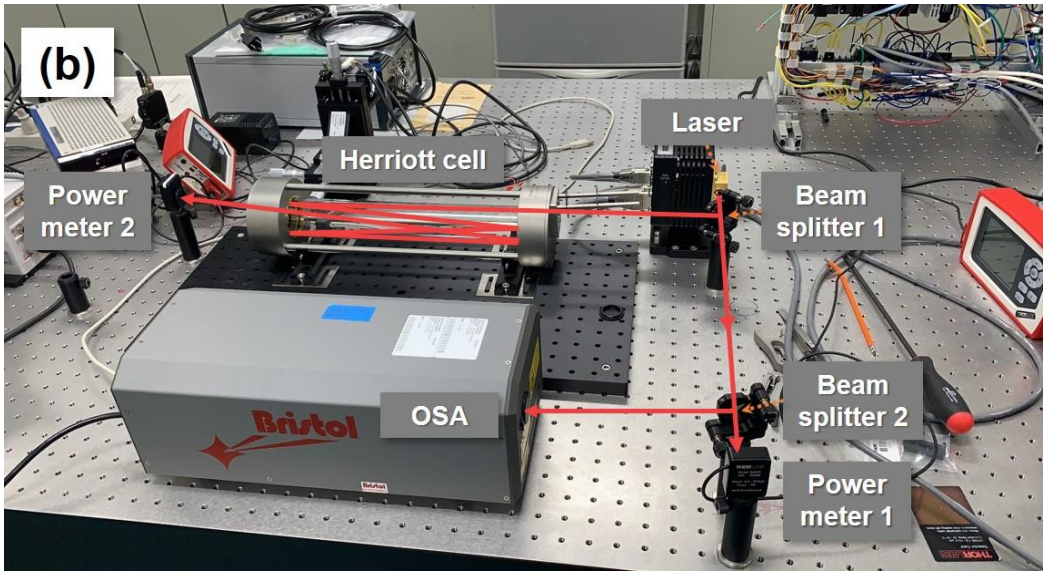

Fig. 5-8. (a) Schematic diagram and (b) photograph of the multipass isotope detection system using a Herriot-type gas cell.

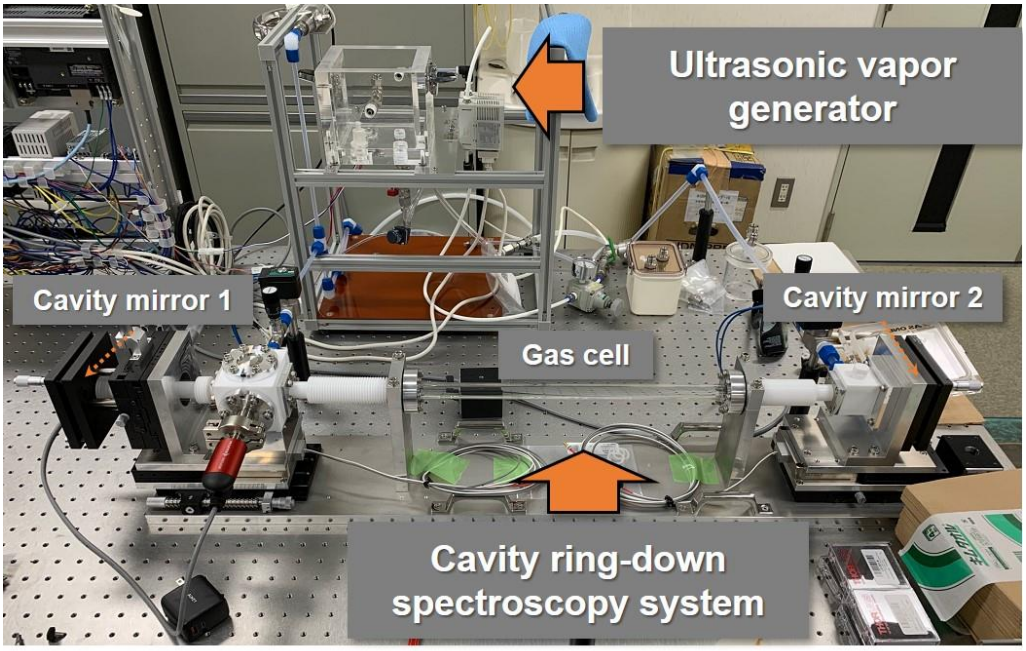

Fig. 5-9. Photograph of the cavity ring-down spectroscopy system.

References (Chapter V)

[5-1]. C. Liu, and L. Xu, "Laser absorption spectroscopy for combustion diagnosis in reactive flows: A review," Applied Spectroscopy Reviews, **54**(1), 1–44 (2019).

[5-2]. https://hitran.iao.ru/molecule/simlaunch

[5-3]. W. Zhong, and J. D. Haigh, "The greenhouse effect and carbon dioxide," Weather, **68**(4), 100–105 (2013).

[5-4]. https://www.thorlabs.com/newgrouppage9.cfm?objectgroup_id=6485

[5-5]. P. L. King, M. S. Ramsey, P. F. McMillan, and G. Swayze, "Laboratory Fourier transform infrared spectroscopy methods for geologic samples," Infrared Spectroscopy in Geochemistry, Exploration, and Remote Sensing, **33**, 57–91 (2004).

VI. Conclusion

6.1 Summary of this dissertation

This research focuses on the development of high-performance mid-infrared laser sources for water isotope detection in nuclear fusion environments. The ultimate objective is to develop novel mid-infrared lasers capable of combining high power, narrow linewidth, and widely tunable capabilities, aiming to advance the development of laser absorption spectroscopy-based isotope diagnostics techniques, which is expected to overcome the inherent limitations of difficult for real-time, in-situ measurements in conventional mass spectrometry or liquid scintillation counter. This dissertation presents several self-developed, state-of-the-art mid-infrared lasers suitable for ultrasensitive spectroscopy applications. Additionally, a preliminary exploration of water isotope detection using mid-infrared lasers is demonstrated.

The first part of this dissertation focuses on the development of a 3-μm laser based on an Er:YAP crystal. A cryogenic cooling scheme was proposed to improve the thermal management of the Er:YAP laser and achieve high laser performance. Experimental studies demonstrate that the low temperature can facilitate the population inversion in a 3-μm Er-laser system and can effectively increase the lasing efficiency of Er:YAP. The cryogenic Er:YAP laser shows promise for breaking the power limit of current Er-lasers and provides discrete tunability in the 3-μm spectral region. Moreover, the tunable and narrow-linewidth spectral property of Er:YAP laser is of significant interest for water isotope detection.

The second part presents the novel development of a 4-μm laser based on an Fe:ZnSe crystal. A compact design of Fe:ZnSe laser end pumped by our self-constructed Er:YAP laser was proposed to achieve a miniaturized, high-efficiency 4-μm laser. The proposed Fe:ZnSe laser demonstrates the generation of a record-high optical efficiency 4-μm laser with watt-level output power and good beam quality, indicating that the Er:YAP laser is a reliable and cost-effective pump source for Fe:ZnSe. Further, a theoretical modeling of Fe:ZnSe laser was proposed to provide guidance for future optimization.

The third part introduces a hybrid Fe:ZnSe amplifier scheme for achieving high-power, narrow-linewidth, and widely tunable 4–5 μm mid-infrared lasers. This hybrid amplifier

scheme can effectively solve the problem of difficulty in precise spectral control of Fe:ZnSe oscillators. Using the Fe:ZnSe amplifiers injection-seeded by quantum cascade lasers, a record-high-power, pure single-frequency 4.3-μm laser and a high-power, narrow-linewidth laser with a total tuning range of 630 nm were successfully demonstrated. The developed laser systems combining high output power, narrow spectral linewidth, and wide tuning range within 4–5 μm can meet the requirements of high-precision spectroscopy applications and are thus promising light sources for water isotope detection.

Finally, a preliminary study is conducted on water isotope detection using mid-infrared DFB-QCLs operating at 6.3 μm and 7.4 μm. The experiments demonstrate the successful calibration of absorption peaks of three water isotopes (H_2O, HDO, and $H_2{}^{18}O$) and the feasibility of interference-free detection. The proposed compact and portable detection system shows great potential for real-time, in-situ measurements.

Overall, this work presents a comprehensive investigation into the development and application of mid-infrared laser sources for water isotope detection in nuclear fusion environments. The developed lasers demonstrate significant improvements in terms of performance, including better thermal management, higher output power, higher efficiency, and precise spectral control. These advancements could open up new possibilities for real-time, in-situ measurements of water isotopes in fusion reactors, enabling more accurate monitoring of plasma parameters and ensuring safe and steady operation.

Moreover, the findings of this work have implications not only for the field of laser spectroscopy but also for other areas that require compact and high-power laser systems, such as optical communication, industrial processing, and medical diagnosis. The compact and portable system design also paves the way for practical applications outside of the laboratory setting.

6.2 Future prospects

Future research directions may involve further optimization and refinement of the developed laser sources, as well as the implementation of ultrasensitive isotope detection using self-developed lasers combined with multipass spectroscopy techniques. Several optimization directions are worth exploring, as discussed follows:

(1). Further power improvement of cryogenic Er:YAP laser

The use of an optically anisotropic window in the cryogenic Er:YAP laser introduced significant depolarization loss into the laser cavity, thus resulting in a low laser efficiency. To address this issue, future optimization efforts should focus on using an optically isotropic substrate to minimize intracavity loss. Additionally, the Er:YAP crystal exhibited degraded absorption at low temperatures, suggesting that a longer crystal is preferable for achieving a higher optical-to-optical efficiency and hence higher laser power. Notably, no thermal rollover of laser power was observed during the experiment, indicating that the laser output power can be further increased by simply increasing the pump power in future studies.

(2). Laser performance optimization of Fe:ZnSe oscillator

Power saturation was also not observed in the 4-μm Fe:ZnSe laser. The maximum output power was mainly limited by the available 3-μm pump power. Therefore, increasing the power of the laser is the first priority. Theoretical modeling of the Fe:ZnSe laser suggests that effective power improvement at a limited pump power can be achieved by appropriately increasing the output coupling transmission or by slightly increasing the Fe:ZnSe crystal length. Additionally, the theoretical study predicts that the thermal lensing effect is the main factor hindering power improvement of the Fe:ZnSe laser. The corresponding countermeasure is to insert a compensating lens into the resonator to extend the power scaling capability.

(3). Power improvement and tuning range extension of hybrid Fe:ZnSe amplifier

Optimizing the extraction efficiency of an amplifier system is crucial for increasing the amplified laser power. Theoretical calculations based on a rate equation model for Fe:ZnSe amplifier regime demonstrate that using a multipass amplifier structure can effectively increase the extraction efficiency and hence the output power, which can be readily achieved by employing a space-reduced cryostat and placing several high reflectors for beam guidance. Furthermore, a cascade amplifier chain can be constructed to continuously amplify the laser power. For the extension of the tuning range, a DFB-QCL array [6-1] or an EC-QCL based on a bound-to-continuum designed chip can be used as the input signal to demonstrate a high-power, single-frequency laser that is tunable throughout the entire gain spectrum of Fe:ZnSe.

(4). Integration of multipass absorption spectroscopy with self-built laser systems

After eliminating the atmospheric CO_2 interference using a pure gas circulator, future studies will focus on water isotope detection using our self-developed 3–5 μm laser systems. First, all the absorption peaks of water isotopes within this wavelength range will be accurately calibrated by precisely scanning the wavelength of the laser systems. Subsequently, we will combine our high-performance mid-infrared lasers with either a Herriott-type gas cell [6-2] or a cavity ring-down spectroscopy technique [6-3] to implement multipass absorption spectroscopy. This integration aims to gradually achieve high-sensitivity detection of lower-concentration samples. Figure 6-1 illustrates a schematic diagram of the final detection system.

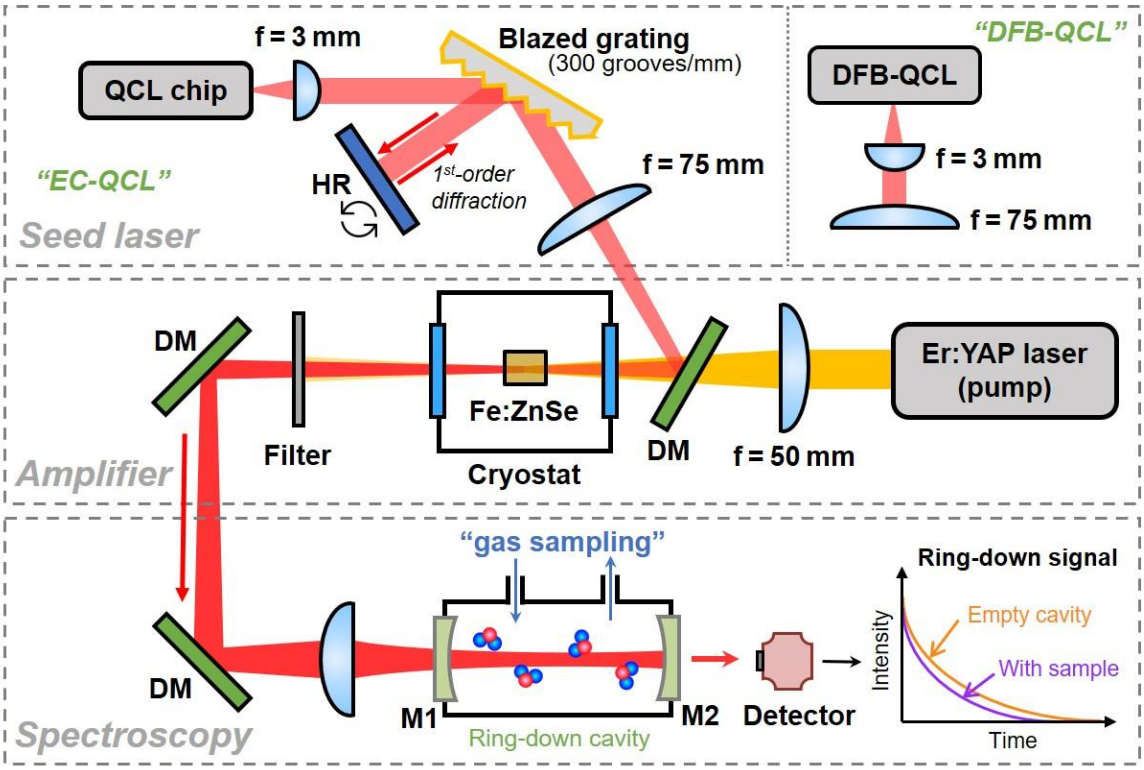

Fig. 6-1. Final diagram of the isotope detection system using our self-developed high-performance laser sources.

The work presented in this dissertation has accomplished the design of the front-end laser systems, i.e., the seed laser and amplifier sections, and has made significant progress in the preliminary exploration of spectroscopic studies. Subsequent results on water isotope detection will be reported in future publications.

References (Chapter VI)

[6-1]. B. G. Lee, M. A. Belkin, R. Audet, J. MacArthur, L. Diehl, C. Pflügl, F. Capasso, D. C. Oakley, D. Chapman, A. Napoleone, D. Bour, S. Corzine, G. Höfler, and J. Faist, "Widely tunable single-mode quantum cascade laser source for mid-infrared spectroscopy," Applied Physics Letters, **91**(23), 231101 (2007).

[6-2]. P. Werle, F. Slemr, K. Maurer, R. Kormann, R. Mücke, B. Jänker, "Near-and mid-infrared laser-optical sensors for gas analysis," Optics and Lasers in Engineering, **37**(2-3), 101–114 (2002).

[6-3]. K. Iwamoto, H. Tomita, R. Terabayashi, V. Sonnenschein, and K. Saito "Development of 2.2 μm cavity ring-down spectrometer for tritiated water analysis," Japanese Journal of Applied Physics, **62**(3), 036001 (2023).

Acknowledgement

This dissertation marks the culmination of a long and unforgettable journey, one that would not have been possible without the unwavering support of numerous individuals, for which I am profoundly grateful. First and foremost, my deepest and sincerest gratitude goes to my supervisors, Prof. Ryo Yasuhara and Prof. Hiyori Uehara. Their consistent and invaluable guidance, encouragement, advice, and discipline throughout my PhD journey have been instrumental in shaping the outcome of my research. I am truly grateful for their unwavering commitment to my academic growth.

I would also like to extend my appreciation to Prof. Shigeki Tokita of Kyoto University and Prof. Fedor Potemkin of Moscow State University, without whose help I could not have successfully completed my PhD work. Their expertise and support have been invaluable.

I would like to thank all the members of the NIFS laser group: Dr. Weichao Yao for his continuously selfless and productive advice, Dr. Quan Shi for refining my presentations, Dr. Mingzhong Zhao for help collecting and interpreting spectroscopic data, and Dr. Linpeng Yu for inspiring me with innovative ideas and insights.

I would like to express my gratitude to my colleagues: Dr. Hiroki Kawase for helping me acclimate to our lab, Dr. Haotian Yang, who fluently speaks Japanese, for his countless help with my daily life, Dr. Hikaru Kumai for being my tutor and offering living support, and Dr. Yuki Tamaru for fruitful discussions about my work.

I would be remiss if I did not thank Nakamura-sensei for teaching me the most important skill to survive in Japan— the Japanese language! Special thanks to the individuals in the Graduate Student Affairs Section and the Secretary offices for all the behind-the-scenes work involved in supporting my life in Japan.

I would also like to thank all friends, colleagues, and mentors who have provided valuable insights, feedback, and support during this journey. I apologize that I cannot mention each of you individually, but please know that your contributions have been truly appreciated.

Furthermore, I am eternally grateful to my family for their unwavering support,

unconditional love, belief in my abilities, and financial assistance. Their encouragement has been the driving force behind my pursuit of higher education.

A special acknowledgment goes to my incredible girlfriend, Ms. Yajie Shen. Her constant love, encouragement, and remote company kept me motivated and focused on completing my PhD study. I am deeply indebted to her and recognize that I could not have achieved this without her.

Finally, I would like to acknowledge the SOKENDAI Special Researcher Program for providing the fellowship and research grant, without which this PhD research would not have been possible.

Once again, I extend my heartfelt appreciation to everyone who has contributed to the successful completion of my doctoral dissertation. May the future be forever bright for all of us.

Enhao Li

Publications

First-authored papers:

[1]. **Enhao Li**, Hiyori Uehara, Weichao Yao, Shigeki Tokita, Fedor Potemkin, and Ryo Yasuhara, "High-efficiency, continuous-wave Fe:ZnSe mid-IR laser end pumped by an Er:YAP laser," Optics Express, 29(26), 44118–44128 (2021).

[2]. **Enhao Li**, Weichao Yao, Hiyori Uehara, and Ryo Yasuhara, "Cryogenically cooled 2.8 μm Er:YAP laser with watt-level output power," Applied Physics Express, 15(9), 092003 (2022).

[3]. **Enhao Li**, Hiyori Uehara, Shigeki Tokita, Weichao Yao, and Ryo Yasuhara, "A hybrid quantum cascade laser/Fe:ZnSe amplifier system for power scaling of CW lasers at 4.0–4.6 μm," Optics and Laser Technology, 157, 108783 (2023).

[4]. **Enhao Li**, Hiyori Uehara, Shigeki Tokita, Mingzhong Zhao, and Ryo Yasuhara, "High-power, single-frequency mid-infrared laser based on a hybrid Fe:ZnSe amplifier," *submitted to Optics and Laser Technology* (2023).

[5]. **Enhao Li**, Hiyori Uehara, Shigeki Tokita, Linpeng Yu, and Ryo Yasuhara, "Room temperature, high-repetition-rate gain-switched Fe:ZnSe laser end pumped by a Q-switched Er:YAP laser," *in preparation*.

Co-authored papers:

[1]. Weichao Yao, **Enhao Li**, Hiyori Uehara, and Ryo Yasuhara, "Efficient diode-pumped Er:YAP master-oscillator power-amplifier system for laser power improvement at 2920 nm," Optics Express, 29(16), 24606–24613 (2021).

[2]. Haotian Yang, Hengjun Chen, **Enhao Li**, Hiyori Uehara, and Ryo Yasuhara, "Electro-optically Q-switched operation of a high-peak-power Tb:$LiYF_4$ green laser," Optics Express, 29(20), 31706–31713 (2021).

[3]. Weichao Yao, Jian Liu, **Enhao Li**, Zhen Zhang, Xiaodong Xu, Jun Xu, Liangbi Su, Hiyori Uehara, and Ryo Yasuhara, "Tb,Y:SrF_2 crystal for efficient laser operation in the visible spectral region," Optics Letters, 47(4), 774–777 (2022).

[4]. Weichao Yao, Hiyori Uehara, **Enhao Li**, and Ryo Yasuhara, "Power-scalable two-wavelength pumped Er:YAP laser at 2.9 μm," Optics and Laser Technology 152, 108073 (2022).

[5]. Shuangyuan Feng, Hiroki Natsume, Shin Kajita, **Enhao Li**, Ryo Yasuhara, Masayuki Tokitani, Hirohiko Tanaka, and Noriyasu Ohno, "Fabrication of tungsten-based optical diffuser using fiberform nanostructure via efficient plasma route," *accepted by Optics Express* (2023).

Conference Presentations

International conferences:

[1]. (Oral Presentation) “Study of the CW laser properties of Fe:ZnSe single crystals at ~4 μm,” Optics & Photonics International Congress 2022 (OPIC2022), Yokohama, April 2022.

[2]. (Oral Presentation) “Highly-efficient CW Fe:ZnSe Laser Amplifier at ~4 μm,” The 15th Pacific Rim Conference on Lasers and Electro-Optics (CLEO-PR2022), Sapporo, August 2022.

[3]. (Poster Presentation) “Power Scaling of Widely Tunable, Narrow-linewidth (<0.3 nm) Mid-infrared Lasers Based on a Hybrid QCL/Fe:ZnSe Amplifier,” Laser Congress 2022, Barcelona, December 2022.

[4]. (Oral Presentation) “QCL-seeded Fe:ZnSe Amplifier System for High-power, Narrow-linewidth Mid-infrared Laser Generation,” Optics & Photonics International Congress 2023 (OPIC2023), Yokohama, April 2023.

Domestic conferences:

[1]. (Oral Presentation) “A watt-level mid-IR Fe:ZnSe laser pumped by a 3 μm Er:YAP laser,” JSAP 第 6 回フォトニクスワークショップ, online, November 2021.

[2]. (Oral Presentation) “A high-optical-efficiency, CW mid-IR Fe:ZnSe laser pumped by an Er:YAP laser,” 2021 年度レーザー学会中部支部若手研究発表会, online, December 2021.

[3]. (Oral Presentation) “Highly-efficient CW 4 μm Fe:ZnSe laser pumped by an Er:YAP laser,” レーザー学会学術講演会第 42 回年次大会, online, December 2022.

[4]. (Oral Presentation) “Study of the CW laser amplification properties of the Fe:ZnSe crystal at mid-IR band,” 第 69 回応用物理学会春季学術講演会, Sagamihara, March 2022.

[5]. (Oral Presentation) “High-power, single-longitudinal-mode Fe:ZnSe laser amplifier injection-seeded by a DFB-QCL at 4.3 μm,” 第 83 回応用物理学会秋季学術講演会, Sendai, September 2022.

[6]. (Oral Presentation) “Cryogenically cooled Er:YAP laser operating at ~3 μm,” レーザー学会学術講演会第 43 回年次大会, Nagoya, January 2023.

[7]. (Oral Presentation) “High-power, narrow-linewidth and widely tunable mid-IR laser based on a hybrid QCL/Fe:ZnSe laser amplifier,” 第 70 回 応用物理学会 春季学術講演会, Tokyo, March 2023.

Awards:

[1]. 2021 年度レーザー学会中部支部若手研究発表会 優秀発表賞

[2]. 第 53 回（2022 年秋季）応用物理学会講演奨励賞

[3]. The Best Students Oral Paper Award – The 12th Advanced Lasers and Photon Sources Conference